A Study of Particle Entrainment in Two Common Particle-Fluid Flows in Nature: Bedload Transport in Rivers and Debris Flows in Upland Regions

A DISSERTATION
SUBMITTED TO THE FACULTY OF THE GRADUATE SCHOOL
OF THE UNIVERSITY OF MINNESOTA
BY

AMIRREZA GHASEMI

IN PARTIAL FULFILLMENT OF THE REQUIREMENTS
FOR THE DEGREE OF
DOCTOR OF PHILOSOPHY

KIMBERLY HILL

MAY, 2020

Acknowledgements

First and foremost, my deepest gratitude to my advisor, Prof. Kimberly Hill, for her guidance and assistance throughout my entire PhD studies as well as many opportunities she provided throughout my studies that helped me to grow both in my career and in my life.

I would like to thank my dissertation committee members, Prof. Vaughn Voller, Prof. Chris Paola, Prof. Xue Feng, and Prof. Andy Wickert for their help and support.

I would like to thank my Iranian friends, my friends at Saint Anthony Falls Laboratory and at the University of Minnesota for all their help, support and encouragement during my PhD studies.

Finally, I would also like to thank my family who have always offered their unconditional love and support to me which has been one of the greatest driving forces behind my work.

Dedication

In dedication to my beloved parents and brothers.

Abstract

This work performed for the research describes in this dissertation concerns particle entrainment in two common particle-fluid flows in nature: 1) bedload transport in rivers, and 2) debris flows in steep upland regions. The bedload transport work addressed here concerns height-dependent entrainment from a bed of a channelized flow. Towards this, we perform distinct element method (DEM) simulations to study the roles of particle size and fluid flow on the transport rate, bed surface variations, and depth-dependent particle entrainment. We do so in the context of a theoretical probabilistic formulation derived to better capture spatial variation in sediment exchange between bed material load and alluvial deposits (Parker et al. (2000)). Our findings allow us to provide a link between the longitudinal bedload transport rate with vertical bed surface statistics and provide closure for a theoretical model designed to model transport and bed-surface exchange in the presence of bed variabilities. The debris flow erosion work here focuses on the effect of grain size distribution of a debris flows on the rate of entrainment of bed material. Towards this, we perform several experiments in a laboratory flume where we measure the relative roles of inclination angle, bed composition, and average flow composition on average and instantaneous erosion dynamics. Most significantly, we find that the infiltration of fine particles into a coarse bed can markedly increase the rate of erosion. Further, the infiltration rate is maximized for intermediate concentrations of small particles in the flow. We show this is due to the interplay of two simultaneous mechanisms: (1) segregation dynamics known as *kinetic sieving* in the shear flow when there is sufficient agitation of the coarse particles to allow the small particles to sink into the bed and (2) correlated interparticle forces which create sufficient agitation only with an adequately high concentration of coarse particles. In this presentation we demonstrate how a better understanding of these two processes can contribute to a better understanding of the "sediment cycle" in earth-surface dynamics.

Contents

List of Tables

List of Figures

Chapter 1

Introduction to the tale of two erosion processes

Fluid flows carry particles over a wide range of scales in natural settings, from the transport of rain droplets in air and tiny organisms in oceans to spray flows that distribute a liquid over an area. In some cases, for example, for small particles of low densities, the particles are carried passively by fluid. In other words, their motion is essentially identical to the fluid around them. However, in most cases, the particles have their own complex motion, distinct from surrounding fluid, due to their inertia which prevent particles to purely follow the motion of fluid. In the latter case, both qualitative and mathematically quantitative descriptions of their motion requires consideration of each type of material – minimally fluid and solid – to describe the dynamics of the system. To describe the macroscopic behavior of the system, in many of these cases, dynamics at particle scale needs to be determined.

Among many fluid-particle transport in nature, there are two forms of transport, that despite their considerable impacts on public safety, environmental sustainability, infrastructures, and landscape evolution, a physics-based understanding of their dynamics is not reached that can describe many phenomena occured within these systems. The

first of these two, is the sediment transport in rivers which affect the environment and landscape and occurs in the forms of *bedload transport*, *suspended load transport*, and *washload transport*. *Bedload* refers to the particles in the rivers that move closely to the bed surface (often in contact with the bed) in the forms of rolling, sliding, or saltation. Depends on the flow magnitude in rivers, the size of bedload particles varies but often is dominated by coarser particls such as gravels and cobbles. *Suspended load* are those particles that are mostly not in contact with the bed and carried with surrounding fluid or big jumps. *Bedload* and *suspended load* particles forms the bed material loads. Finally, the *wash-load* particles are those very fine particles that are washed by flow and almost never in contact with the bed and their motion can be described by the motion of the fluid.

The second type of fluid-particle flows are those gravity-driven flows of boulders, gravels, and mud down hillslopes often called "*Debris Flows*". These massive and rapid flows of poorly sorted particles originate, usually, from the steep upland regions. The particles in debris flows vary in size, from microns (e.g. clay and silt) to meters (e.g. boulders) (Takahashi (2009)). In addition, debris flows can have a significant amount of organic material. For example, those originated in forested steep can have up to 60% organic debris (Hungr et al. (2001)) (see Fig. 1.1 for a schematic comparison of these two transport processes).

At the first glance, these two sediment transport processes may look similar as a mixture of particles with fluid is transported within a channel. However, there are certain differences between these two transport processes which distinguish them from each other. A few of these differences are as follows:

- **Material**: Debris flows have a high concentration of particles in motion which can exceed 50 percent while the concentration of particles in bedload transport is usually less than 10 percent. In addition, the particles involved in bedload transport are usually narrow in size (e.g. gravel or cobble particles) while debris

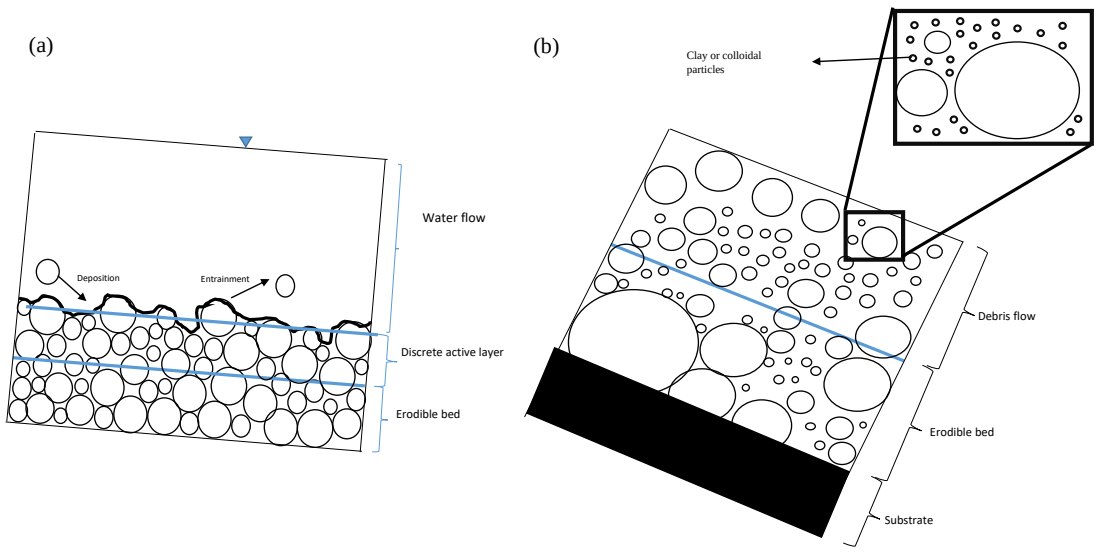

Figure 1.1: Schematic illustration of (a) bedload transport, (b) debris flows. Different inclination angle is used to emphasize on the slopes these flow occur. Particles are not scaled.

flows have a wide range of particles from clays to boulders.

- **Dominant driving force on particles for transport**: Debris flows occur on steep slopes where the main driving force is the gravity while the natural rivers where the bedload transport occurs have usually a very mild slope (0.01-0.1%). For this reason, the main driving force on particles in bedload transport is the fluid force.

- **The span of particle movement**: Most of the particles transport occurs near the bed in bedload transport while in debris flows, particles are in motion in the whole overlying flow, from the bed to the surface of the flow.

- **Type of dominant particle movement**: Transport of particles in bedload is highly episodic, especially at low transport stages which are the common conditions in natural rivers. This episodic behavior means the particles have a chance of entrainment and once they are entrained, they can move for some distance

downstream before being deposited. This behavior of bedload motions has motivated some researchers to consider the stochastic framework in studying of these processes because the mean parameter cannot adequately describe the transport. On the other hand, the motion of particles in debris flows are usually continuous, which means once they are entrained, they keep their motion until they face some kind of flow resistance such as the change in slope. Due to this characteristic of debris flows, the stochastic framework is less considered in describing the motion of particles in flow and instead, researchers use depth-average equations to describe the dynamics of these flows (Iverson (2012)).

- **Rheology of flow over erodible bed materials**: The interstitial fluid in bedload transport is water while in debris flow is mud due to the high concentration of clay and silt particles. The interstitial fluid in bedload transport where the concentration of particles is low behaves like a Newtonian fluid while in debris flows where high concentration of particles is common, the interstitial fluid behaves like non-newtonian fluid. While different models (e.g. Bingham model) are used to describe the rheology of debris flows, it is believed the interstitial fluid behaves like a shear-thinning fluid where the viscosity of fluid decreases under shear strain.

This study aims to contribute in providing a physics-based understanding of the flow dynamics of these two processes. One underlying parameter to understand the dynamics of these flows, is to understand how the particles erode and becomes part of these flows. In this regard, the focus of this study is to understand the statistics of the entrainemnt rate in these flow and the parameters that control this rate.

With this brief introduction of the bedload transport and debris flows, we present our methodology to study these processes and our results regarding the statistics and flow dynamics of these processes in the next chapters. In particular, this dissertation is organized as follows:

- Chapter 2 provide a historic review of the frameworks used by researchers over

the last few decades to describe the mass balance of bedload particles with the strength and weakness of each framework.

- Chapter 3 describes the methodology used by author to study the bedload transport. In particular, this chapter presents our Distinct Element Method (DEM) to simulate the bedload transport.

- Chapter 4 provides the results obtained in this study regarding the statistics of the bed surface and particle entrainment and how these statistics change for different size particles and hydraulic conditions.

- Chapter 5 provides a discussion of results presented in chapter 4.

- Chapter 6 provides a historic review of the attempts made by researchers to understand the particles erosion by debris flows through experimental and in-field studies.

- Chapter 7 describes the experimental procedure and the methodology used in this study to investigate the important parameters that control the entrainment rate of debris flows.

- Chapter 8 presents the results obtained through the experimental studies regarding the entrainment rate of debris flows. This chapter ends with a discussion of these results.

- Chapter 9 summarizes the main conclusions of this study and suggest the potential improvements of this study with future investigations.

Chapter 2

Literature review of mass balance of sediment in bedload transport

Predicting the evolution of alluvial channels is a significant problem for environmental restoration and also for adaptation under ever-changing climate conditions. To predict spatial and temporal evolution of alluvial channels, modelers combine (1) equations expressing the conservation of mass and momentum of the fluid flow (e.g., Saint-Venant equations, or similarly well-known representations); (2) equations expressing the conservation of mass along the sediment bed surface (e.g., the Exner equation), and (3) equations expressing a dependence of particle transport on average fluid stress on an alluvial bed (e.g,. by Meyer-Peter and Muller (1948); Ashida and Michiue (1972); Wilcock and Crowe (2003)). This work is concerned with the manner in which we relate spatial gradients in sediment transport with temporal height changes in a sediment bed, primarily associated with (2) above. For this we turn what is often called "the Exner Equation," essentially conservation of sediment mass.

The Exner equation is named after the Austrian physicist, Felix Exner, who proposed this equation for the first time, through his work on sand dunes. In its simplest form, assuming uniform particle density and constant solid fraction throughout of the bed,

the Exner equation can be expressed as:

$$(1-\lambda_p)\frac{\partial \eta(x,t)}{\partial t} = -\frac{\partial q(x,t)}{\partial x} \tag{2.1a}$$

$$(1-\lambda_p)\frac{\partial \eta(x,t)}{\partial t} = D(x,t) - E(x,t) \tag{2.1b}$$

Here, q is the volumetric transport rate of sediment per unit width and λ_p is the bed porosity. We use x as the direction of average transport, so $\partial q/\partial x$ is the spatial gradient of sediment transport downstream. If negative, then it contributes to a growth in local bed height, η, over time t (Fig. 2.1(a)). As indicated, the Exner Equation is sometimes expressed in what is typically called the *entrainment form* using the difference between local rates per unit area of deposition D and entrainment E.

While either form provides an extraordinarily efficient way to capture average elevation changes in a sediment bed, neither has the functionality to reflect any variations associated with grain size distributions, nearly universal in natural rivers. Therefore, this equation cannot capture a certain phenomena observed in river channels such as the vertical sorting and bed surface composition (Parker (1991a)). To explain these phenomena, modellers need to write this equation at particle scale (i.e. averaged over 1 to 2 particle sizes), which prevents an efficient way of modelling these phenomena.

To resolve this problem, Hirano (1971) suggested that the particles' size distribution should be divided into several classes and the mass balance be written for each class separately. The idea of dividing the particle's size distribution into several classes is first used by Einstein et al. (1950) to describe the transport rate of sediments. He suggested that the transport rate of each class of particles in a mixture can be calculated as the transport rate of that class in a uniform mixture multiplied by the fraction of that class in the mixture. This assumption, however, does not take into account the effects of sorting and shielding of fine particles by bigger particles.

To account for possible sorting of particles in a non-uniform mixture while formulating the sediment mass conservation, Hirano (1971) introduced into the model framework a thin layer just below the bedload transport layer, known as "active" layer (also known as "mixing" or "exchange" layer in the literature). Hirano's active layer based model includes explicit consideration of a finite-thickness (1 - 3 particle sizes in the absence of bed forms to prevent any formation of vertical pattern) interface layer between particles in transport and bed deposit. Thus, the bed deposit is divided in two parts: the interface or active layer and the substrate. In tracking the concentration of one particle type i (e.g., color only, density, or size), we can write the active-layer version of the (entrainment form) Exner equation as:

$$(1-\lambda_p)\left[f_{L,i}\frac{\partial \eta}{\partial t}+(f_{a,i}-f_{L,i})\frac{\partial L_a}{\partial t}+L_a\frac{\partial f_{a,i}}{\partial t}\right]=D_i-E_i \tag{2.2}$$

L_a is the active layer thickness (Fig. 2.1(b)); $f_{L,i}$ is the volume fraction of particles of type i in the active layer at the interface of the active-layer with substrate, and $f_{a,i}$ is the volume fraction of particles of type i in the active layer. D_i and E_i represent volumetric sediment deposition rate and sediment entrainment rate, respectively, per unit area. Porosity λ_p is approximated as uniform from the bottom of the transport layer and active layer and throughout the substrate. The volume fraction of particles of type i in the active layer is approximated as uniform.

This model framework tracks entrainment and deposition of a particular grain type i in substrate-transport exchange translated somewhat through the finite-thickness active layer. For example, during a depositional period, the grain size characteristics of the particles in transport do not necessarily equal the characteristic of the top of the bed. Rather, the characteristics of the sediment transferred to the substrate during deposition are generally a combination of that in the active and transport layers and are assigned in a manner that can differ from one model to the next (Ferguson (2003)).

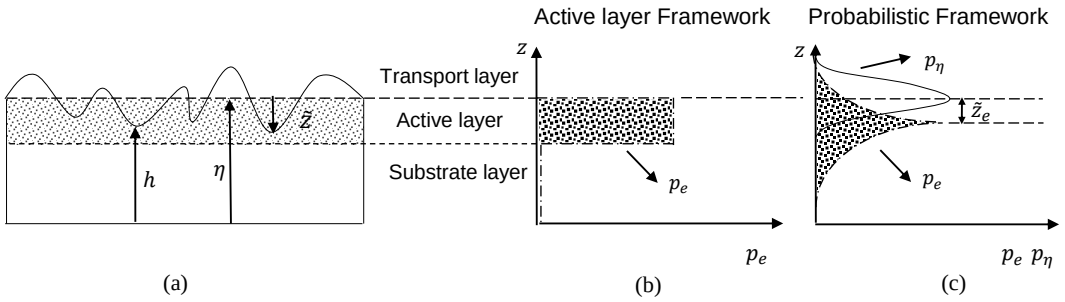

Figure 2.1: Schematic representation of the bed and the difference between discrete and continuous models: (a) a representative sketch of a bed, (b) Discrete model with *active layer* formulations, and (c) continuous model proposed by Parker et al. (2000).

Since the introduction of this discrete layer framework of sediment mass balance, it has provided a framework for the community to explain some of the phenomena observed in nature such as downstream fining in river (e.g. Parker (1991a,b)), the long-term evolution of a gravel-sand transition (e.g. Ferguson (2003)), sedimentation in lakes and reservoirs (Cui et al. (2006b,a)) and the prediction of the spatial distribution of sediment sizes in an alluvial deposit, i.e. the grain size stratigraphy (Ribberink (1987)).

While this framework captures some aspects of grain size segregation and associated stratification that occur during depositional processes at the associated timescales, it does not have the capability to account for exchanges that can happen due to grain size effects with what can be somewhat shorter timescales. An example of this occurs when smaller particles in a mixture find "pockets" in a bed at a statistically higher rate than do larger neighboring particles and push the larger particles into transport through a "squeeze-expulsion" mechanism (Savage and Lun (1988)). The time scale of this process depends more on the particle dynamics time scales than it does on depositional scales and thus cannot be fully captured through the active layer model.

Under equilibrium conditions, restrictions of the active-bed layer formalism become even more apparent. The exchange of sediment among layers can only be associated with changes in the mean bed elevation. During steady conditions ($\partial q/\partial x = 0$, and $D = E$)

this framework predicts no exchange at all between substrate, active, and transport layers (Viparelli et al. (2010a,b)). Also, the discrete representation of the deposit limits entrainment and deposition to the topmost part of the bed. In summary, active layer-based models cannot account for vertical sediment fluxes associated with bedform migration, cannot reproduce the infiltration of fine particles in a coarse substrate, fail to reproduce the fine details of the alluvial stratigraphy and cannot capture tracer and contaminant dispersal (Blom et al. (2008); Parker (2004); Pelosi et al. (2014)).

To resolve the problems associated with the active layer framework, Armanini (1995) took a significant step forward and developed a new sediment continuity formulations without discretizing the bed deposit into several layers. Armanini's depth-continuous model considers the instantaneous sediment mass balance at the bed surface for each class of sediments:

$$\tilde{\beta}_j \frac{\partial h}{\partial t} = -\frac{\partial \tilde{q}_j}{\partial x} \tag{2.3}$$

where $\tilde{\beta}_j$ represents the instantaneous percentage of class j at the bed surface that includes any possible porosity of the bed. $\tilde{q}_j$ represents the instantanous transport rate of class j. That is, "˜" refers to the instantaneous quantities. h is the instantaneous bed elevation (see Fig. 2.1). Equation 2.3 neglects the storage of sediments in the water coloumn; however, Armanini (1995) included the term associated with storage of sediments in the water column in his formulation but for this study, we assume the storage of sediments in the water column is negligible.

Armanini (1995) divided each term in equation 2.3 into an average and fluctuating quantity. Then, he took an ensemble average of the parameters (similar to what is done for turbulent flows to derive Reynolds Average Navier Stokes (RANS) equations) and introduced a new term, that he called it a diffusive term, to explains the vertical flux

of particles ($\overline{\beta_j' \frac{\partial \eta'}{\partial t}}$).

$$\beta_j \frac{\partial \eta}{\partial t} + \overline{\beta_j' \frac{\partial \eta'}{\partial t}} = -\frac{\partial q_j}{\partial x} \tag{2.4}$$

Here, $\eta' = h - \eta$ (see Fig. 2.1). He treated the diffusive term using the Boussinesq diffusive model:

$$\overline{\beta_j' \frac{\partial \eta'}{\partial t}} = \epsilon_z \frac{\partial \beta_j}{\partial z} \tag{2.5}$$

where ϵ_z is a diffusion coefficient.

Although this model can explain some of the vertical fluxes occurred within the bed in the small time-scale, this model would predict the uniform distribution of all particle sizes in the vertical direction in the long time-scale, which is not in agreement to what has been observed in nature and experimental studies (Blom et al. (2008)). While the specific model proposed by Armanini (1995) had limitations, the idea of a depth-continuous model of sediment continuity that he proposed was later used by Parker et al. (2000) in another form.

Parker et al. (2000) proposed a new continuous framework which they referred to as "the probabilistic Exner equation". This new framework captures bed height variations and erosion / deposition height variations in a probabilistic sense. In comparison with the "active layer approach", which models a likelihood of entrainment with depth as a step function, this probabilistic approach allows the likelihood to vary continuously with distance in the bed (Fig. 2.1). At the same time, this framework has the capability to represent and track explicitly the fractions of particles of different sizes as well as other characteristics. While this framework is both efficient and flexible, there are unresolved

closure problems we address herein.

We can express the conservation of sediment volume at elevation z in the deposit for uniform materials in the following form:

$$(1-\lambda_p)p_\eta(x,z,t)\frac{\partial\eta(x,t)}{\partial t} = p_d(x,z,t)\times D - p_e(x,z,t)\times E \tag{2.6}$$

p_η is a height-dependent probability density, essentially, the probability that the instantaneous (or local) bed elevation is at height z at time t. p_d and p_e are the probability densities that account for bed-normal, depth dependent deposition and entrainment rates. This probabilistic form of the Exner equation allows for bedload-substrate particle exchange below (or above) the average bed surface, common in cases of bed surface variability associated with roughness, bedforms, etc. (as in Fig. 2.1). In other words, the bed-normal depth dependences of p_d and p_e represent expected variability in deposition and entrainment associated with short term changes of local bed level associated with sediment transport processes as particles are alternately plucked from and deposited into the bed (Figure 2.1). The form allows for segregation in mixtures with significant spatial variability (bed roughness and bedforms). And the form allows for bedload-bed exchange under steady state. This framework offers all this without need to explicitly represent short-term variability. However, for its application to alluvial problems, the framework needs closure, in other words, functional forms for p_d, p_e, and p_η.

Wong et al. (2007) took the first significant steps toward testing the probabilistic framework and deriving expressions for p_d, p_e, and p_η. They performed laboratory flume experiments using gravel particles of a narrow, lognormal size distribution with $d_{50} = 7.1\ mm$ and $d_g = 7.2\ mm$ where d_{50} is the median particle size and d_g is the geometric mean particle size. They performed experiments under steady state, lower-regime plane-bed conditions. To find p_η, they used a sonar-transducer system to measure

local time-dependent bed elevations. In doing so, they found that p_η follows a Gaussian distribution whose standard deviation s_η depends on bed shear stress τ_o:

$$p_\eta(h|\eta, s_\eta^2) = p_\eta(\tilde{z}|0, s_\eta^2) = \frac{1}{\sqrt{2\pi}s_\eta(\tau)} exp\left[-\frac{1}{2}\left(\frac{\tilde{z}}{s_\eta(\tau)}\right)^2\right] \tag{2.7}$$

Here, following Wong et al. (2007), $\tilde{z} = \eta - h$ (see Fig. 2.1(a)). Unfortunately p_d ($= p_e$ in steady state conditions) were inaccessible directly due to the opacity of the particles and associated difficulty of identifying initial particle movement and the associated height just prior to that movement. Instead, based in part on depth-dependent entrainment of tracer particles, Wong et al. (2007) proposed an elevation-specific density for entrainment from their data:

$$p_d(\tilde{z}) = \frac{1}{2s_\eta(\tau)} exp\left(-\frac{|\tilde{z} - \tilde{z}_e - \tilde{z}_n|}{s_\eta(\tau)}\right) \tag{2.8a}$$

$$p_e(\tilde{z}) = \frac{1}{2s_\eta(\tau)} exp\left(-\frac{|\tilde{z} - \tilde{z}_e + \tilde{z}_n|}{s_\eta(\tau)}\right) \tag{2.8b}$$

$\tilde{z}_e$ is an offset Wong et al. (2007) suggested characterizes steady state conditions (i.e., mobile-bed equilibrium). They proposed that maximum entrainment was likely to occur just below the average bed surface ($\tilde{z}_e \geq 0$). $\tilde{z}_n$ an additional offset function that characterizes non-equilibrium conditions. Their experimental data suggest $\tilde{z}_e = 0.25d_{50}$. Since their experiments involved equilibrium conditions, no value for $\tilde{z}_n$ was available.

These experimental data provided the confidence that this framework would be effective in capturing depth-dependent phenomenology in bedload transport conditions. However, physical experiments to gather the additional data needed to close the equations are extremely limited. Measurements of bed height such as those performed by

Wong et al. (2007) are limited to the absolute local surface of particles and cannot distinguish between moving particles and particles in the bed. Modern techniques such as index-matched tracking of subsurface particles show promise but at present have not been performed to address these issues.

In this work, we aim to close the probabilistic Exner equations using computational simulations based on the distinct element method (DEM). In DEM simulations, we can track the motion of each particle at every time step and thus can provide robust particle location and velocity at each time step toward the derivation of local bed height and elevation-specific erosion and deposition densities. Additionally, since different effects can be "turned on" and "turned off" in DEM simulations, we can systematically explore the importance of specific system details, including grain size distribution, grain shape, average stress on the bed, and turbulent fluctuations. Therefore, in this study, we aim to, first, conduct computational experiments with similar conditions to the physical experiments performed by Wong et al. (2007) in terms of grain size distribution and fluid properties and bed shear stress. Our goal by conducting this first set of experiments is to, first, validate the form found by Wong et al. (2007) for the bed surface variations and second, to find a form for the elevation-specific entrainment of particles. Then, this study aims to extend the first set of experiment to a wider range to include different size particles and turbulent fluctuations. Through these experiments, we aim to the provide functional forms for p_e and p_η to close the probabilistic framework and to find the role of particles size and turbulent fluctuations on the forms of these parameters.

In the next chapter, we present our simulations set-up including the particle size distribution and baseline fluid model.

Chapter 3

Computational Experiments

Toward determining how the statistics of bed height and entrainment height vary with bed shear stress and particle size, we performed extensive computational distinct element method (DEM) experiments. DEM was first introduced by Cundall and Strack (1979) to model systems of particles. Since the introduction this method, it has been adopted by many researchers in a wide range of application (Zhu et al. (2008)).

In this technique, the motion of each particle in the system is determined with Newton's equation of motion by considering the contact and non-contact forces. Depending on the application, different forces are considered. For our simulation, we consider three sets of forces: (1) Those due to contacts with other particles, (2) those associated with fluid-particle interactions, and (3) body forces (specifically, the weight of each particle). As such, we can use the following governing equations to describe the translational and rotational motion of each particle:

$$m_i \frac{dv_i}{dt} = \Sigma_j F_{ij}^c + \Sigma_k F_{ik}^{nc} + F_i^f + F_i^g \tag{3.1a}$$

$$I_i \frac{d\omega_i}{dt} = \Sigma_j M_{ij} \tag{3.1b}$$

Here i is the subscript for particle i. m_i, v_i, I_i, ω_i are the mass, velocity, moment of inertia and rotational velocity of particle i respectively. F_{ij}^c, F_{ik}^{nc}, M_{ij} are respectively, the contact force, non-contact force such as van der Waals and electrostatic forces, and torque on particle i by particle j or k. F_i^f and F_i^g are the fluid and gravitational force on particle i respectively. Equation 3.1 is a general form for the equation of motion of a particle among other particles in a fluid.

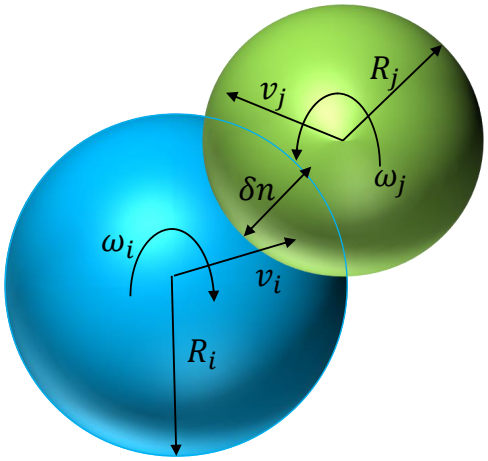

Figure 3.1: Schematic illustration of two particles in contact with each other with arbitrary translational and rotational speed.

Several researchers have implemented this technique in studies of bedload transport to provide more information at particle scale between fluid and particles which cannot be captured with current experimental facilities. Early models developed for this purpose used relatively simple fluid models to simulate the interactions between fluid and particles. For example, Jiang and Haff (1993) used a single "slab" or "layer" to model the fluid flow. In their model, the momentum equation was solved at each time step for fluid layer by considering only forces due to shear stress and drag forces on particles. Later, Jiang (1995) took a similar approach but developed a multi-slab model to account for spatially variable momentum exchange between particles and fluid during intense bedload transport. McEwan et al. (1999) used the multi-slab model developed

by Jiang (1995) to study the bedload transports at lower transport stages close to the critical thresholds.

With these relatively simple models, new information were provided which enhanced the understanding of the underlying mechanism of bedload transport. For example, Jiang (1995) found during the intense bedload transport, the shear stress is linearly proportional to shear rate in the lower sediment layers which leads to an exponential velocity profile for fluid within these layers. McEwan et al. (1999) found a need to distinguish between what they called a dynamic roughness, which is a roughness caused by moving grains, and a static roughness, that is the roughness caused by stationary grains on the surface, in how they influenced flow and transport rate. Based on this, they found dynamic roughness contributes more to flow resistance for moderate to high transport rates while in low transport stages, static roughness plays a significant role.

With further development in computer technology and simulation techniques, researchers implemented more complex fluid models. Schmeeckle and Nelson (2003) explicitly included mechanisms for representing turbulent fluctuations and shielding of downstream grains by upstream grains. They performed simulations where in which they represented their fluid velocities with experimental measurements of fluid over a mobile bed under a low transport stage. They calculated a modified local fluid velocity each particle "experienced" (through a drag force) according to:

$$U_{xr} = \left(\overline{u}_x erf\left(\frac{I_d}{5h_p} \right) + u'_x \right) \left(1 - \frac{v_{xw}}{u_x} \right) \tag{3.2}$$

Here U_{xr} is the reduced downstream velocity including the mean ,$\overline{u}_x$, and fluctuating u'_x components, and v_{xw} is the component of the velocity of the wake particle in the downstream direction. h_p is the height of the protrusion of the wake particle above that of the top of the bed particles and I_d is the downstream distance between two particles. When they incorporated this locally defined velocity in the equation of motion in their

DEM simulations, they found their simulations follow the transport relation of Luque and Van Beek (1976).

Drake and Calantoni (2001) considered the bedload transport at intense transport stages, often called sheet flows, in coastal regions where the flow is typically bidirectional and oscillating rather than the unidirectional flow of rivers. To model the transport, they used multi-layers of fluid which exchange momentum via eddy viscosity. Each layer of the fluid exerts drag, buoyancy, added mass and pressure gradient force on the particles within them. Their model was fully coupled which means the particles influence the motion of fluid layers by exerting the equal and opposite force on them. Like the most of DEM simulations for bedload transport, they neglect the lift and Magnus forces.

More recently researchers have used more complex models for fluid phase to provide a more realistic simulations of bedload transport. Most of these studies have considered a discrete description for solid phase and a continuous description for fluid phase (Lagrange/Euler). For example, Ji et al. (2013) studied the influence of turbulent coherent structures on particles entrainment by using the direct numerical simulation (DNS) of turbulent flow combined with discrete element method to model the particle motion. Maurin et al. (2015) used the same framework, Lagrangian description for the solid phase and Eulerian description for the fluid phase, to propose a model for studying steady bedload transport. They used DEM to model the solid phase and spatially averaged two-phase Navier-Stokes equations to model the fluid phase. Schmeeckle (2014) numerically investigated the transport of sand particles by combining a turbulence-resolving large eddy simulations (LES) with DEM. In this simulation Schmeeckle (2014) results showed a similar relationship to that of Meyer-Peter and Muller (1948) relationships modified by Wong and Parker (2006), specifically: $q^* = 3.97(\tau^* - 0.0495)^{1.5}$. Here, q^* is the normalized transport rate as we define later in Eq 4.2, and τ^* is the normalized bed shear stress.

More the focus of Schmeeckle (2014) paper of DEM simulations with a fully coupled LES fluid model was on the bed roughness which is a measure of frictional resistance

that the flowing water experiences. His study indicates the bed roughness increases as the bed transport rate increases. He also found the peak of transport rate occurs near the bed surface where a large number of particles are in motion with relatively small velocity. This result illustrates the transport rate is governed more by the number of particles in motion rather than the velocity of particles which is in agreement with other studies (Roseberry et al. (2012); Ancey (2010)).

All these works show the strength of the DEM technique in studying of the bedload transport. Therefore, we use this technique to simulate the bedload transport in this study. We introduce our DEM details in the next section.

3.1 Our DEM details

Our DEM simulations are built on an in-house DEM model developed first by Hill and Tan (2017). This model uses a one-way coupling between the particles and fluid and considers the most important forces relevant to the bedload transport, in most ways similar to the framework introduced by Schmeeckle and Nelson (2003). We chose this framework for its relative simplicity in the baseline representation of fluid, particles, and fluid-particle interactions. This then allowed us to study how varying this framework affected the outcome of the transport results in a systematic way.

For completeness we describe the framework we use in detail here and point out deviations from the model of Schmeeckle and Nelson (2003) when they arise.

3.1.1 The equation of motion for our DEM simulations

Similar to Schmeeckle and Nelson (2003), at each time step we calculate the force $\vec{F}_{p,k}$ on each particle k according to:

$$\vec{F}_{p,k} = \vec{F}_{c,k} + \vec{F}_{g,k} + \vec{F}_{b,k} + \vec{F}_{m,k} + \vec{F}_{d,k} \tag{3.3}$$

$\vec{F}_{c,k}$ refers to the net contact forces which equals to the sum of all forces exerted by the other particles that are touching particle k, and requires further discussion as we do shortly in Section 3.1.2.

$\vec{F}_{g,k}$ refers to the gravity force on particle k:

$$\vec{F}_{g,k} = \rho_{p,k} \forall_{p,k} \vec{g} \tag{3.4}$$

where $\rho_{p,k}$ is the mass density of the particle k, $\forall_{p,k}$ is the particle volume and $\vec{g}$ represents the gravitational acceleration.

$\vec{F}_{b,k}$ refers to the buoyancy force on particle k:

$$\vec{F}_{b,k} = \rho_f \forall_{p,k} \vec{g} \tag{3.5}$$

where ρ_f is the fluid density.

$\vec{F}_{m,k}$ refers to the added mass force on particle k:

$$\vec{F}_{m,k} = \rho_f \forall_{p,k} c_m \frac{d\vec{u}_{p,k}}{dt} \tag{3.6}$$

where c_m is the added mass coefficient and $\vec{u}_{p,k}$ is the particle velocity. To calculate the added mass force, we use $c_m = 0.5$ as suggested by Batchelor (1976) and Drake and Calantoni (2001), though we note Jiang and Haff (1993) following Landau and Lifshitz (1987) assumed $c_m = 0.2$.

$\vec{F}_{d,k}$ refers to the drag force on particle k:

$$\vec{F}_{d,k} = \frac{1}{2}\rho_f c_d A_k |\vec{u}_{\mathrm{rel,p}}| \vec{u}_{\mathrm{rel,p}} \tag{3.7}$$

where $A_k = \pi d_{p,k}^2/4$ is the central cross-sectional area of particle k, $\vec{u}_{\mathrm{rel,k}}$ is a relative particle velocity, similar to that of the particle relative compared to that of the fluid as we detail in section 3.1.3, and c_d is the drag coefficient that is a function of a particle Reynolds number (Re_s) as suggested by Drake and Calantoni (2001):

$$c_d = 24 {Re_s}^{-1} + 4 {Re_s}^{-0.5} + 0.4 \tag{3.8a}$$

$$Re_s = |\vec{u}_{\mathrm{rel}}| d_p/\nu \tag{3.8b}$$

where ν is the kinematic viscosity of fluid and given in table 3.1.

Table 3.1: Summary of fluid and particle properties. The properties of particles are chosen similar to those reported for granite particles.

Property	**Magnitude**
fluid density ρ_f	1000 kg/m^3
fluid kinematic viscosity ν_f	$10^{-6} m^2/s$
particle density ρ_p	2650 kg/m^3
particle elastic modulus E_p	29 GPa
particle Poisson's ration ν_p	0.2

3.1.2 Interparticle contact force model

The manner in which we represent interparticle interactions is the way in which our baseline framework differs the most from that of Schmeeckle and Nelson (2003). While they used the forces on hard spheres to represent interparticle forces, we used a framework that explicitly represents particle properties as we summarize here. We model the interparticle contact forces, F_c, using the *Hertz-Mindlin* contact theory with a damping component specified by Tsuji et al. (1992) and Coulomb sliding friction. To calculate $\vec{F_c}$ on each particle, we sum over all interparticle contacts; Each interparticle contact force is calculated in terms of normal and tangential components:

$$F_n = -k_n {\delta_n}^{3/2} - \eta_n {\delta_n}^{\frac{1}{4}} \dot{\delta}_n \tag{3.9a}$$

$$F_t = \min[-k_t {\delta_n}^{\frac{1}{2}} \delta_t - \eta_t {\delta_n}^{\frac{1}{4}} \dot{\delta}_t, -\mu F_n \delta_t / |\delta_t|] \tag{3.9b}$$

As is standard in such a mechanistic model (e.g., see Tsuji et al. (1992)), F_n and F_t are considered in the normal and tangential directions relative to the interparticle contact plane, whereas δ_n and δ_t are model deformations in these normal and tangential directions, represented computationally as overlapping regions. Here and throughout the dissertation, $\dot{q}$ represents temporal derivatives in any variable q. k_n and k_t are stiffness factors, and η_n and η_t represent damping factors, all of which can be calculated based on particles properties such as particle size, mass, Young's moduli, and etc. Tables 3.2 define the contact parameters (i.e. η_n and η_t) in terms of the particle properties.

α in Table 3.2 is 0.07 for a coefficient of restitution ~ 0.9 according to Tsuji et al. (1992). Table 3.2 defines the contact parameters based on particles effective characteristics which these effective parameters are defined in 3.3 for two particles.

Table 3.2: Expressions for contact parameters of our DEM model.

Contact Parameter	**Expression**
k_n	$\frac{4}{3}\sqrt{R_{eff}}E_{eff}$
k_t	$8\sqrt{R_{eff}}G_{eff}$
η_n	$\alpha\sqrt{m_{eff}k_n}$
η_t	$\alpha\sqrt{m_{eff}k_t}$

Table 3.3: Expressions for effective parameters used in defining the contact parameters.

Effective Parameter	**Expression**
R_{eff}	$\left(\frac{1}{R_1}+\frac{1}{R_2}\right)^{-1}$
E_{eff}	$\left(\frac{1-\nu_1^2}{E_1}+\frac{1-\nu_2^2}{E_2}\right)^{-1}$
G_{eff}	$\left(\frac{2(1+\nu_1)(2-\nu_1)}{E_1}+\frac{2(1+\nu_2)(2-\nu_2}{E_2}\right)^{-1}$
m_{eff}	$\left(\frac{1}{m_1}+\frac{1}{m_2}\right)^{-1}$

3.1.3 Fluid models

The foundational fluid model used in this study is based on the model used by Hill and Tan (2017) ,in this, we also differ from Schmeeckle and Nelson (2003) who used experimentally measured velocities for their simulation results. In this model, the representation of bed shear stress τ_o relies on the well-known expression for what is known as the "*log-law of the wall*," a mathematical expression of the average stream-wise fluid velocity profile $\overline{u}_{f,x}(z)$ observed under steady turbulent conditions (see Fig. 3.2:

$$\overline{u}_{f,x}(z) = \frac{u_\tau}{\kappa} ln\left(\frac{z}{z_0}\right) \tag{3.10a}$$

$$z_0 = k_s/30 = 3.5d_{50}/30 \tag{3.10b}$$

In this equation, $u_\tau \equiv \sqrt{\tau_o/\rho_f}$ is the shear velocity, $\kappa = 0.41$ is the von Karman constant, and z_0 is the position at which the fluid velocity is zero ($\overline{u}_{f,x}(z_0) = 0$). As relatively common, we define z_0 in terms of a roughness coefficient, k_s, that scales with a representative particle diameter (e.g., Pope (2001), Schlichting and Gersten (2016), Van Rijn (1982)). We dynamically locate the position at which $\overline{u}_{f,x}(z) = 0$ so that the distance between the bed surface and the zero-fluid-velocity plane is $z_1 = 2d_{50}$, as we discuss in Section 3.2.

The fluid model used by Hill and Tan (2017) neglected the turbulent fluctuations and assumed the fluid velocity in the $y-$ and $z-$ directions are zero. In this study, we use the same fluid model proposed by Hill and Tan (2017) for many of the simulations, although, we introduce the turbulent fluctuations into our simulations later to understand the role of these fluctuations on the bed surface statistics. We explain our fluid model that consider the turbulent fluctuations in the simulations in section 4.3, but for now we focus on explaining the relatively simple fluid model used in this study without any consideration of turbulent fluctuations.

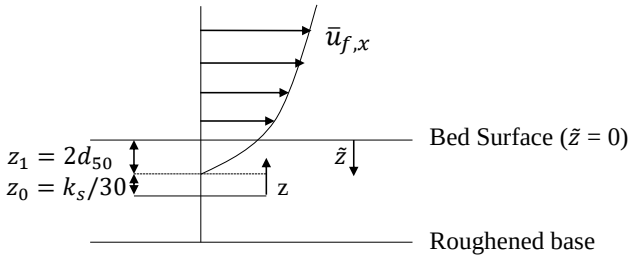

Figure 3.2: Sketch of flow velocity profile of the simulated bedload transport.

Since, we neglect the velocity fluctuations for this fluid model, we assume the fluid velocity in the $y-$ and $z-$ directions are zero and we model the relative velocity in these two directions between the particles and the fluid, which are used to calculate the added

mass and drag forces, as the negative velocity of the particles. $u_{\mathrm{rel},y} = -u_{p,y}; u_{\mathrm{rel},z} = -u_{p,z}$. While we limit ourselves to one-way coupling for the work described here, we include some shielding effect from upstream particles that theoretically influences the drag force experienced by each particle in the downstream. We use the experimentally-derived relationship proposed by Schmeeckle and Nelson (2003):

$$u_{\mathrm{rel},x} = [u_{f,x}(z_c) - u_{p,x}] \times \mathrm{erf}\left(\frac{l_d - h_p}{5h_p}\right) \tag{3.11}$$

In this equation, $u_{f,x}(z_c)$ is the fluid velocity from Eq. 3.10a (Fig. 3.2) at a particular particle center z_c, $u_{p,x}$ is the downstream particle velocity, l_d is the downstream distance between the center of the particle of concern and its first upstream neighbor, and h_p is the height difference between the topmost part of the two particles.

3.2 Computational Experiment Procedure

To initialize each computational experiment, we first provide a channel bed with a certain length and width and sufficiently high so that the particles never encounter the top boundary. We design our channel beds to have a periodic boundary condition in downstream ($-x$) and cross-stream($-y$) directions which means if a particle exits the channel in these directions, it will enter the channel from the other side. By performing various simulations to determine our results were not size limited (see Section 4.1), we designed our channel for the results reported in this study to be about $50 \times d_{50}$ long and $12 \times d_{50}$ wide.

After preparing the channel bed, we introduce the particles into our simulations. We put 3000 particles (for most of the simulations reported in this study) in a crystal arrangement and assign a random size to each particle. However, we limit the random sizes to follow a narrow log-normal distribution. After arranging the particles, we release

them to drop on the channel bed due to the gravity force. While, we drop the particles, the forces are limited to gravity and contact forces. Figure 3.3 shows the particles before releasing and after settling on the bed.

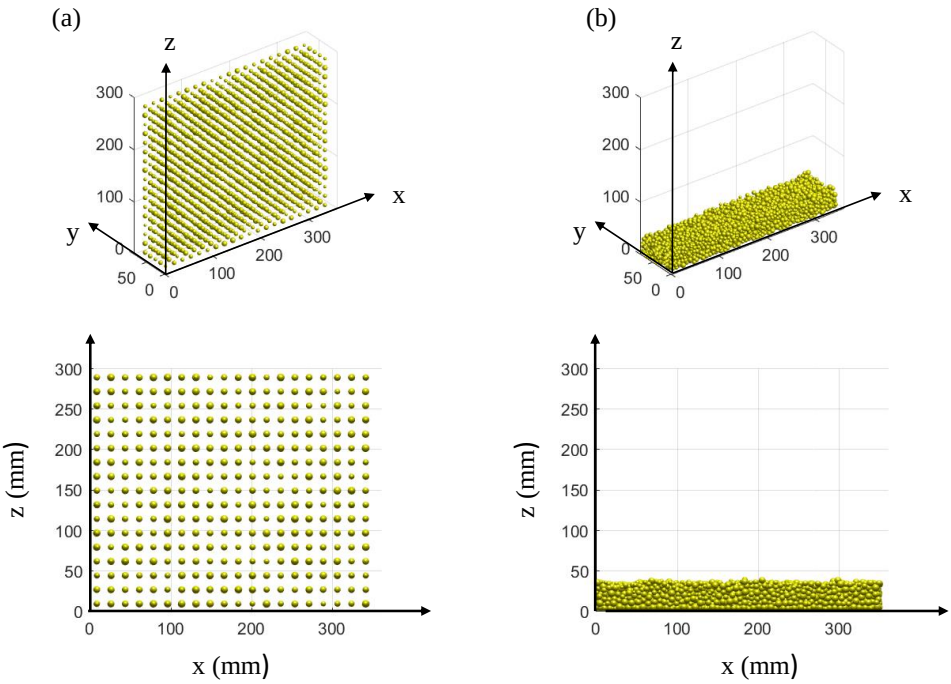

Figure 3.3: Schematic representation of simulated particle in 3D (top row) and 2D (bottom row) for (a) before dropping, and (b) after particles are settled down.

After giving sufficient time to the particles to settle down, we affix the particles touching the base of the channel to this bottom surface to create a rough base and reduce sliding between the particles and the channel base that would otherwise occur. For similar simulations in terms of the particle size, d_{50}, we use the same initialized bed to minimize additional uncertainties that might be introduced by local variations in bed roughnesses. Once the particles in this roughened bottom bed are fixed in place, we "turn on" the fluid forces.

Part of simulating the fluid forces involves positioning the velocity profile ($u_{f,x}(z)$, the *log-law* in Eq. 3.10a), requiring us to determine the location of the bed surface

($z = z_0 + z_1$ in Fig. 3.2). Towards this, we first divide the particle data from the simulated flume (i.e., the computational domain) into five rectangular columns, each the full width of the flume ($12 \times d_{50}$) and $10 \times d_{50}$ long. Then, we determine the top of the highest particle in each column, calculate the average of all five, and set this to be the location of $z = z_0 + z_1$ for the fluid velocity profile. Once we have initiated the fluid velocity, at every time step we calculate all interparticle and fluid forces on each particle, as noted in Eq. 3.3.

After the initiation of fluid flow, the particles on the surface start to move, primarily by rolling and also by hopping. As the particles move intermittently, the top surface can change, and we dynamically adjust the vertical position of the velocity profile accordingly using the top surface of each particle whose velocity is smaller than that of the fluid velocity corresponding to the location of its center. After the system reaches a steady state , we continue the simulations for an additional 20 seconds and report on transport rate, bed height statistics, and entrainment statistics over this time period.

3.3 Time Steps and Numerical Integration

To track the location and movement of each particle through our simulations, we calculate the translational and rotational acceleration of each particle based on the sum of all forces and moments on it,at each time step. We integrate these accelerations using the fourth-order Runge-Kutta method (Chapra et al. (2010)) at each time step to update each particle's translational and rotational positions and velocities throughout the simulation. The fourth-order Runge-Kutta provides a more precise approximation of the particle's motion from one time-step to another. This method, in general, is written as follows:

$$y_{i+1} = y_i + \frac{1}{6}\left(k_1 + 2k_2 + 2k_3 + k_4\right)h \tag{3.12a}$$

$$k_1 = f\left(x_i, y_i\right) \tag{3.12b}$$

$$k_2 = f\left(x_i + \frac{1}{2}h, y_i + \frac{1}{2}k_1 h\right) \tag{3.12c}$$

$$k_3 = f\left(x_i + \frac{1}{2}h, y_i + \frac{1}{2}k_2 h\right) \tag{3.12d}$$

$$k_4 = f\left(x_i + h, y_i + k_3 h\right) \tag{3.12e}$$

where h is the time step. For the simulations of this study, y can be the position a particle, its translational or rotational velocity. For example, if y is assumed to be the position of the particle, then the k parameters are the velocity of the particle at each increment of time-steps and defined in Eq. 3.12.

For this study, each computational time step is approximately $5\mu s$. To save computational time and space, we do not output the particle locations and velocities at each time step but instead we output these information every 10,000 time steps i.e., every $50ms$ which we found is sufficient to provide the details of the transport.

With this introduction of our DEM model, we present our results regarding the bed surface and particle entrainment statistics obtained from DEM simulations in the next chapter. Next chapter is divided in 3 sections: the first section present the results for one particle size distribution with d_{50} and with shear stress conditions similar to to that of Wong et al. (2007) to understand if the simple fluid model presented in this chapter provides similar statistical results as those of Wong et al. (2007). Then, we extend our simulations to include more particle sizes to understand the role of the particle sizes on the statistical paramters of the bed, however, still all the simulations are performed on uni-modal particle sizes and not mixtures. Finally, to understand the role of the turbulent fluctuations on the bed surface statistics, we introduce the

turbulent fluctuations into our DEM model through random walk processes.

Chapter 4

Results of bedload transport

In this chapter, we present our results on bed surface statistics and entrainment height statistics for simulated bedload transport. We organize the results along three distinct topics. The first section focuses on the results from set of parameters that follow those of the bedload experiments of Wong et al. (2007). In the second section, we report the results from three sets of simulations with three specific grain sizes designed to check whether the results are dependent on particle size. In the last section we report how the additions of velocity fluctuations influence the results.

4.1 One Narrow Size Distribution

We performed nine computational DEM experiments with similar conditions to the physical experiments performed by Wong et al. (2007) in terms of grain and fluid properties (Table 3.1) and bed shear stress (Table 4.1). We used these baseline experiments to design our simulations to determine how shear stress on an alluvial deposit influences the statistics of bed height and entrainment height. At the same time using the proximity of these carefully designed controlled experiments provides a reliable control against which we can validate our simulations.

We designed our grain size distribution to follow a narrow log-normal distribution

with median particle size, d_{50} = 7.1 mm, geometric mean particle size, d_g = 7.2 mm, and geometric standard deviation, $\sigma_g = 1.2$, simialr to the physical experiments of Wong et al. (2007). We designed our shear stress conditions to be similar to that of Wong et al. (2007); specifically we varied our bottom shear stress τ_o so that the Shields number ($\tau^* = \tau_o/((\rho_s - \rho_f)gd_{50})$) ranged from $\tau^* = 0.0757$ to 0.1193 (Table 4.1). We set gravity g =9.81 m/s^2.

For most of the simulations we performed for this first set of results (Table 4.1), we used 3000 particles, resulting in a bed with the height of approximately 5 d_{50}. We found this to be a sufficient number of particles (and bed height) so that the results were not affected by this relatively small height (e.g., as compared with runs of 10,000 particles and 15,000 particles in runs 3a and 3b in Table 4.1, respectively).

Table 4.1: Computational flow and bed parameters for d_{50} particles.

Run	**Bed thickness**	τ^*	k_s	z_1	q^*	$\eta(mm)$
1	$\sim 5d_{50}$	0.1193	$3.5d_{50}$	$2d_{50}$	0.050	36.38
2	$\sim 5d_{50}$	0.1052	$3.5d_{50}$	$2d_{50}$	0.029	36.86
3	$\sim 5d_{50}$	0.1044	$3.5d_{50}$	$2d_{50}$	0.033	36.83
3a	$\sim 16d_{50}$	0.1044	$3.5d_{50}$	$2d_{50}$	0.033	113.13
3b	$\sim 25d_{50}$	0.1044	$3.5d_{50}$	$2d_{50}$	0.033	168.17
4	$\sim 5d_{50}$	0.0915	$3.5d_{50}$	$2d_{50}$	0.022	36.38
5	$\sim 5d_{50}$	0.0908	$3.5d_{50}$	$2d_{50}$	0.020	36.14
6	$\sim 5d_{50}$	0.0844	$3.5d_{50}$	$2d_{50}$	0.016	36.17
7	$\sim 5d_{50}$	0.0757	$3.5d_{50}$	$2d_{50}$	0.012	36.18

4.1.1 Transport rate

We calculate a spatially-averaged near-instantaneous unit transport rate q_{t_i} at each output timestep t_i according to:

$$q_{t_i} = \frac{\sum_{p=1}^{N} \forall_p u_{p,x}(t_i)}{\text{bed area}} \tag{4.1}$$

In this equation, $u_{p,x}(t_i)$ is the velocity of particles p at output time step t_i in the downstream direction (if t is the simulation time in seconds after the water is "turned on", $t_i = t*20$); $\forall_p$ is the volume of that particle, N is the number of particles ($N = 3000$ for most of the results reported here), and the bed area for most of the data reported in this section is 350 mm $\times$ 85 mm, or $\approx$ 50 d_{50} $\times$ 12 d_{50}. As is common, we non-dimensionalize our transport rate according to:

$$q^* = \frac{q}{\sqrt{(s-1)g d_{50}} d_{50}} \tag{4.2}$$

often referred to as the Einstein number. Typical for systems in bedload transport, there is a high temporal variability in the transport rate (Fig. 4.1(a)). So, for comparison with experiments, we define the average dimensionless transport rate from $t = t_s = 2.5$ s to time $T = t - t_s$ as q^*_T:

$$q^*_T = \frac{\sum_{t_i=t_s\times 20}^{t_i=(T+t_s)\times 20} q^*_{t_i}}{T \times 20} \tag{4.3}$$

In this form, T and t_s are both expressed in units of seconds, and the factor of 20 that appears throughout is associated with our output rate (and thus available data) of

20 per second. Based on data such as those plotted in Fig. 4.1(a, inset), we used $T = 20$ as a sufficiently long time to average the fluctuations for clear results. Henceforth, we use $q^* \equiv q^*_{20}$ to represent a statistically steady average unit transport rate for each system. Yet, we calculated the uncertainty involves in measuring q^* over the course of our simulations and plot on Fig. 4.2 for each bed shear stress. As clear in this figure, the uncertainty that is involved in the average values of transport rates measured in this study is one order of magnitude smaller than the average values.

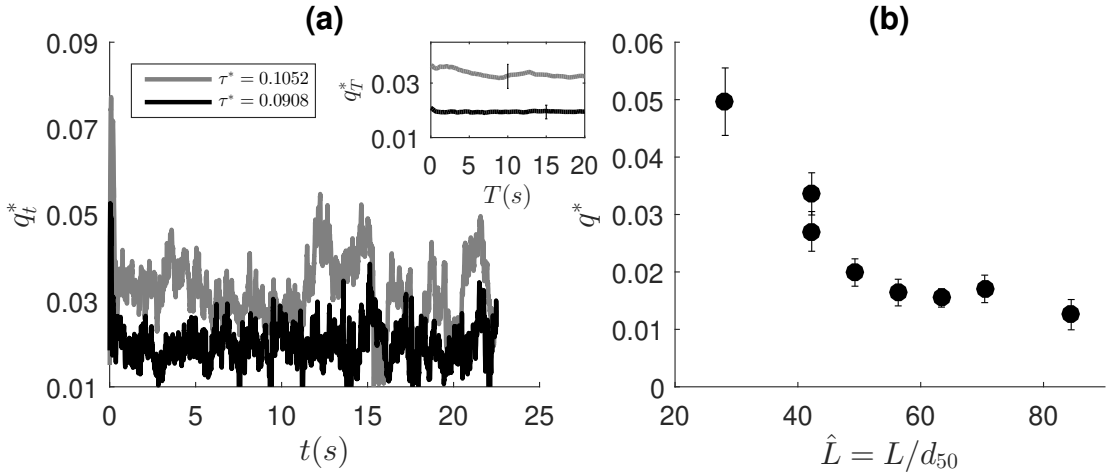

Figure 4.1: The conditions required to perform statistical analyses of bed surface: (a) shows the time needed to reach steady state conditions. The inset shows the average transport rate starting just after reaching steady state to time T after reaching steady state. The error-bar in the inset shows the standard deviation of transport variations for 20 seconds after reaching the steady state conditions. (b) shows the minimum channel length required to eliminate the effect of channel size on the transport rate. q^* represents the average transport rate for 20 seconds after reaching the steady state for $\tau^* = 0.0908$. The error bars represents the uncertainty involved in the calculations of q^* which we calculate as the standard deviation of transport variations for 20 seconds after steady-state conditions.

To compare our transport data with those previously published for similar systems, we note that for a number of well-known bedload transport relations (e.g., Meyer-Peter and Muller (1948); Luque and Van Beek (1976)) including the experiments after which

our simulations were designed, q^* scales roughly as $\tau^{*1.5}$:

$$q^* = a_q \times (\tau^* - \tau_c^*)^{1.5} \tag{4.4}$$

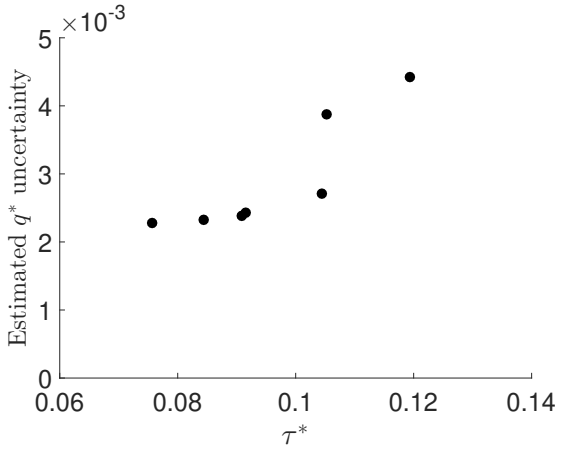

Figure 4.2: Standard deviation of transport rate time series for 20 seconds after reaching steady-state conditions, $t_s = 2.5s$.

Here, τ_c^* is an empirically determined reference stress below which the transport rate is negligible. To compare our results to these published relationships, we calculate the linearized least squares fit of Eq. 4.4 to our data. Fig. 4.3(a) demonstrates that our data are well-fit by this equation when $a_q \approx 2.59$ and $\tau_c^* \approx 0.051$. Our results are particularly close to those from the physical experiments by Wong et al. (2007) after which we patterned our simulations (Fig.4.3(b) and caption). We note that the simulations performed by Schmeeckle and Nelson (2003), after which we designed part of the details of our simulations, are similar to the Luque and Van Beek (1976) relationship plotted in Fig. 4.3(b). On the other hand, the results from simulations of Schmeeckle (2014) are closer to those of Meyer-Peter and Muller (1948) plotted in Fig. 4.3(b).

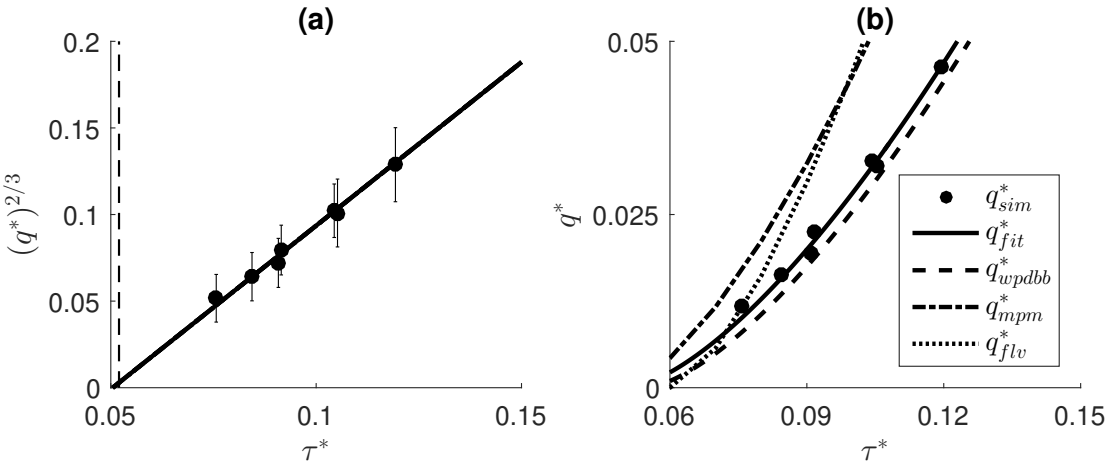

Figure 4.3: a) Our data for $q^{*2/3}$ plotted vs. τ^* (solid circles) and a linearized least squares fit of Eq. 4.4 (line) to those data $[a_q,\tau_c^*]$=[2.59, 0.051]. Vertical dashed line: the reference Shields stress calculated using the Brownlie equation: $0.22Re_p^{-0.6} + 0.06 \times 10^{(-7.7Re_p^{-0.6})}$. b) q^* plotted vs. τ^* for our data (q^*_{sim}) (solid circles) and the fit from (a) (solid line) compared with other previously proposed relationships. q^*_{wpdbb} is the fit proposed by Wong et al. (2007), $[a_q,\tau_c^*]$=[2.66, 0.0549]; q^*_{mpm} is from the well-known transport model proposed by Meyer-Peter and Muller (1948), $[a_q,\tau_c^*]$=[3.97, 0.0495], modified by Wong and Parker (2006); q^*_{flv} is the transport model proposed by Luque and Van Beek (1976), $[a_q,\tau_c^*]$=[5.7, 0.06].

4.1.2 Bed surface statistics

To calculate the bed surface and entrainment statistics, we need to quantitatively distinguish between "bed particles" and "entrained particles". Many particles may be only slightly /jiggling] or *rocking* in a way that one would not normally identify them as entrained, so it is not sufficient to use a distinction of zero or non-zero velocity to determine which we would consider part of the bed, and which we would consider part of the flow. For our work, we consider theoretical forms of average particle velocity in bedload transport, from Bagnold (1956) and Bridge and Dominic (1984) (and references within):

$$u_{p,a} = a_u \times (u_\tau - u_{\tau c}) \tag{4.5}$$

Here, $u_\tau \equiv \sqrt{\tau_0/\rho}$ is typically called the shear velocity, and $u_{\tau c} \equiv \sqrt{\tau_c/\rho}$ is a reference shear velocity. As Bridge and Dominic (1984) discussed, a_u is a coefficient that researchers typically treat as constant and, depending on the study, have found typical values ranging 8.5 (e.g., Bagnold (1956)) to 14 (e.g., Abbott and Francis (1977)). Bridge and Dominic (1984) proposes this variation is due to the fact that the average value of a_u should vary with hydraulic conditions.

In this dissertation we use Eq. 4.5 to provide us with a way to quantitatively distinguish between bed particles and entrained particles that varies with stress. To find out an appropriate value of a_u for the purpose of this study, we try different threshold velocities defined as:

$$u_{\mathrm{th,n}} \equiv n \times (u_\tau - u_{\tau c}) \tag{4.6}$$

where n represents a coefficient similar to a_u in Eq. 4.5. We choose a value for a_u somewhat arbitrarily based on computational results as we present shortly. We consider a particle is stationary and therefore part of the bed at a particular time if its downstream velocity is less than $u_{\mathrm{th,n}}$

Toward calculating the bed surface variability, we divide the channel into 150 subsections (each a column of cross-sectional area $\approx 14\ mm \times 14\ mm \approx 2\ d_{50} \times 2\ d_{50}$). For the jth column, at each time step t_i we record the top of the upper-most stationary particle (whose downstream velocity was less than u_{th}): $z_{top,i,j}$. We defined the averaged bed surface height η as the arithmetic mean of those (600,000) values and calculated what might be considered an effective bed roughness as the standard deviation of the bed surface variations.

For a visualization of how the standard deviation varies with shear stress, we define

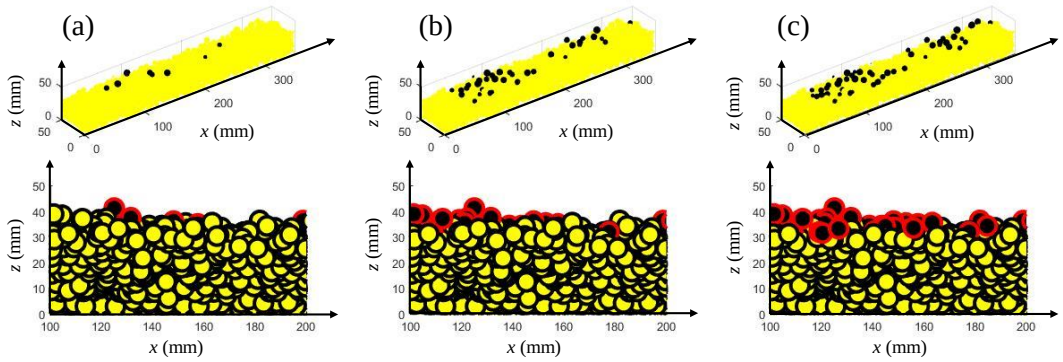

Figure 4.4: Schematic representation of simulated particles in 3D (top row) and 2D (bottom row) to illustrate the effect of changing a_u on the threshold velocity described in the text. The dependence of moving particles number on the threshold velocity: a) $u_{\rm bd} < u_{\rm th,5}$, b) $u_{\rm bd} < u_{\rm th,2}$, c) $u_{\rm bd} < u_{\rm th,1}$. Here $u_{\rm bd}$ is the velocity of bed particles. Arrows show the flow direction.

a variance of each bed height as $\tilde{z}(x_j, y_k, ti) \equiv \eta - z_{top}(x_j, y_k, ti)$. Then we divide these data into 10 bins of equal width ($\Delta\tilde{z}$) ranging from the lowest to highest values of $\tilde{z}$ throughout each experiment. We normalize these binned data and then plot them in Fig. 4.5 for three representative simulations of different shear stresses for four different threshold velocities. From these plots, we can see that, while not perfect in all cases, a Gaussian distribution fits the data well, as suggested by analogous experimental data of Wong et al. (2007).

Similar to the results of Wong et al. (2007), the bed roughness of our simulation data increases with increasing bed shear stress (τ_0), for all different threshold velocities. We plot the standard deviation of the bed heights (s_η) normalized by d_{50} ($\hat{s}_\eta = s_\eta/d_{50}$) versus Shields stress (τ^*) in Fig. 4.6, for all different threshold velocities. As clear in Fig. 4.6, the bed surface roughness, $\hat{s}_\eta$, increases with the bed shear stress; however, the rate of increase is less noticeable for smaller threshold velocities $u_{th,1}$ and $u_{th,2}$.

We note at this point we found no noticeable differences in the bed surface variations when we double and triple the bed height (as in Run 3 compared with Run 3a and 3b), so we focus on analyzing the results only for the 3000 particle simulations for the rest

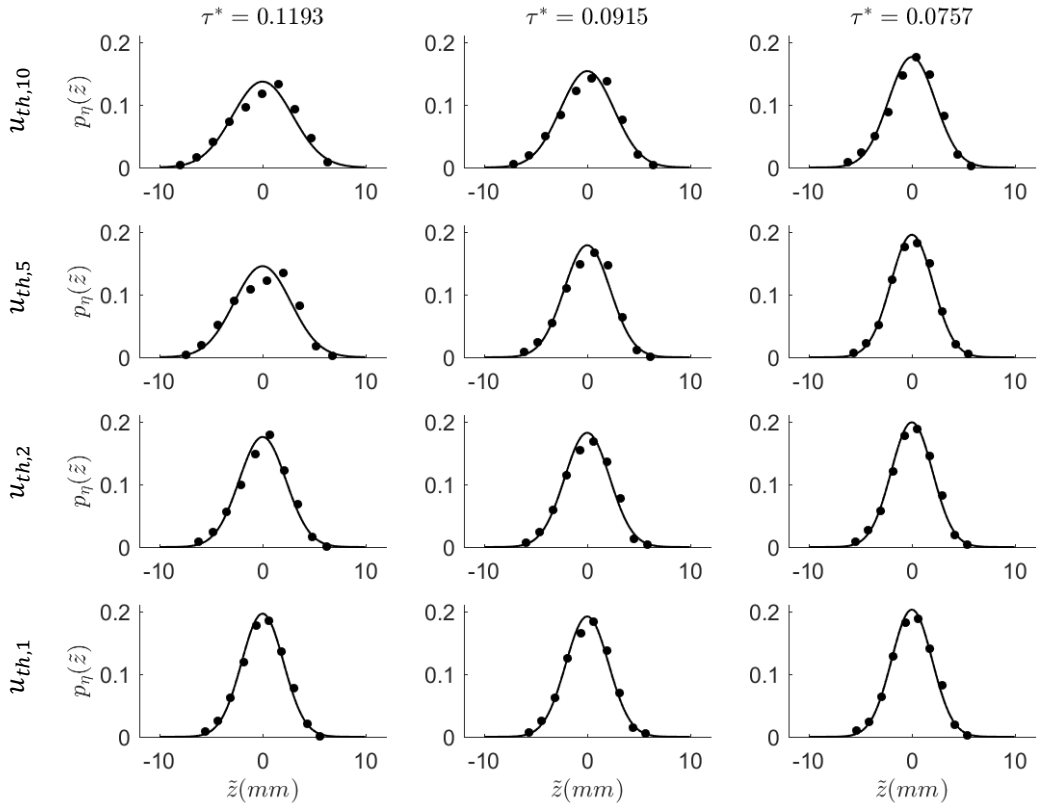

Figure 4.5: Three representatives of probability density distribution of bed height variations for three different threshold velocity. Filled circles represent the simulation data while the solid line represents the Gaussian fitting curve, $p_\eta(\tilde{z}|0, s_\eta^2)$. Table 2 shows the standard deviation of all the computational experiments designed for this study.

of this dissertation.

4.1.3 Particle entrainment statistics

For a quantitative measure of the entrainment height statistics for our data, we first need to define what we identify as an entrainment event, that is, a "conversion" of a bed particle to an entrained particle. Since a particle is not typically considered entrained if it moves only a short distance, especially if the movement is limited to shaking or rocking, we base a quantitative definition on a minimum distance that a

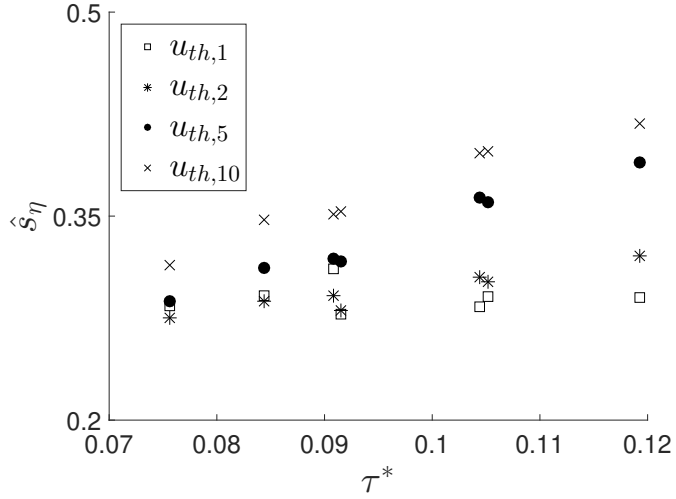

Figure 4.6: The standard deviation of the bed height variations against the Shields stress for different threshold velocities, $u_{th,n}$ where n = 1, 2, 5, 10.

particle must travel in a certain amount of time before we consider it to be entrained. What constitutes a minimal distance to be considered entrained in a general sense is debatable and warrants discussion beyond the scope of this study. For our purpose, we consider a particle entrained if it travels at an average speed greater than u_{th} for 10 time-step or 0.05 seconds. In other words, its minimum displacement once entrained is:

$$\delta r_{min} = u_{\mathrm{th}} \delta t \tag{4.7}$$

where $\delta t = 0.05s$. For each entrainment event defined in this way, we use the vertical position of these particles relative to the mean bed height, $\tilde{z}$, prior to their entrainment for entrainment height statistics. We bin these data and normalize them as we did for the bed height data and plot the distributions for three representative shear stresses of different threshold velocities in Fig. 4.7. For an analytical expression of the probability of entrainment heights, we consider two, the exponential form previously suggested (Eq. 2.8b) and a general Gaussian fit:

$$p_{e,\exp}(\tilde{z}|\tilde{z}_e, s_\eta^2) = \frac{1}{2s_\eta(\tau)} exp\left[-\frac{|\tilde{z}-\tilde{z}_e|}{s_\eta(\tau)}\right] \tag{4.8a}$$

$$p_{e,\mathrm{gau}}(\tilde{z}|\tilde{z}_e, s_e^2) = \frac{1}{\sqrt{2\pi}s_e(\tau)} exp\left[-\frac{1}{2}\left(\frac{\tilde{z}-\tilde{z}_e}{s_e(\tau)}\right)^2\right] \tag{4.8b}$$

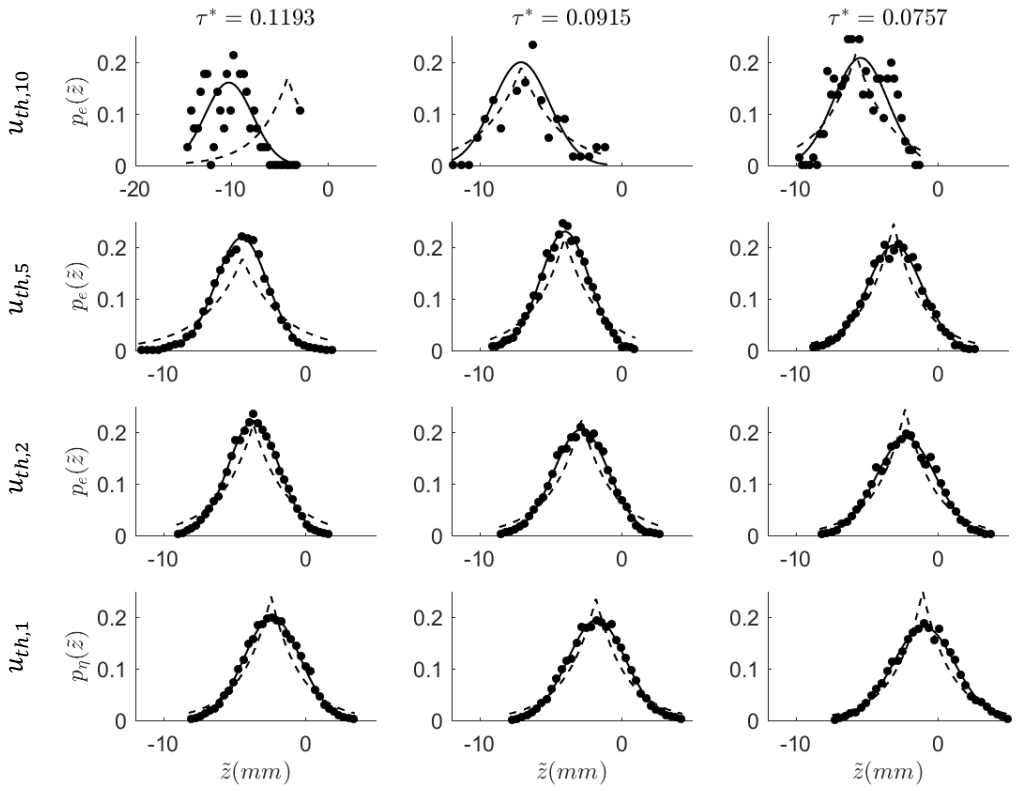

Figure 4.7: Three representative of entrainment height distributions. Filled circles represent the simulation data; the solid line represents a Gaussian fitting curve, $p_e(\tilde{z}|\tilde{z}_e, s_e^2)$ (Eq. 4.8b), and the dashed line represents an exponential fitting curve, $p_e(\tilde{z}|\tilde{z}_e, s_\eta^2)$, suggested by Wong et al. (2007), (Eq. 4.8a). Table 2 shows the fitting parameters of these distributions.

In Eqs. 4.8, s_η is the standard deviation of the bed height likely to increase with

increasing bed shear stress as suggested by Wong et al. (2007); $\tilde{z}_e$ is an offset characterizing the position at which the maximum entrainment occurs, and s_e is the (bed shear stress dependent) standard deviation of the entrainment heights about the mean entrainment height.

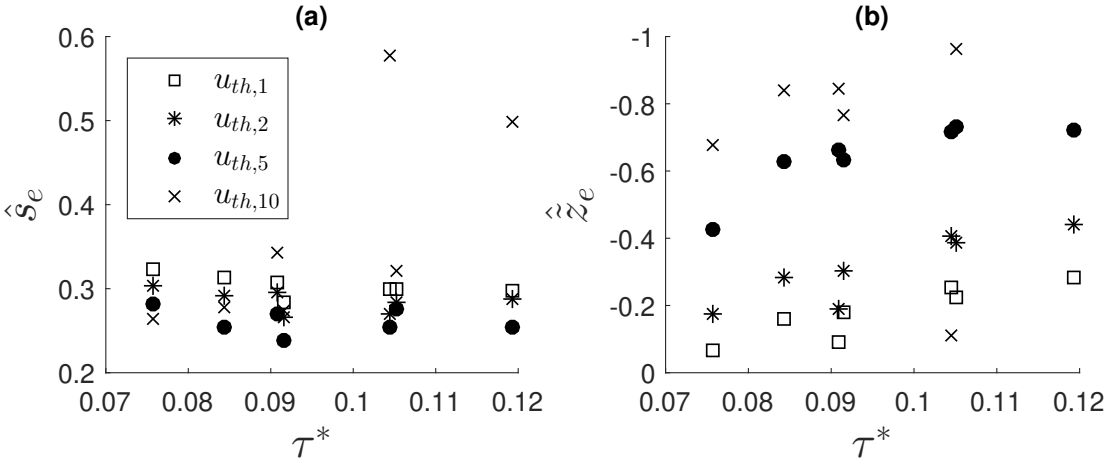

Figure 4.8: Statistics of particles entrainment height distribution against the Shields stress for different threshold velocities: a) shows the standard deviation of the entrainment height distributions, $\hat{s}_e$, b) shows the peak entrainment height , $\hat{\tilde{z}}_e$.

For all simulations, we found p_e well-fit by Guassian distributions; not so well-fit by the exponential form (Eqs. 2.8b and 4.8a). Further, unlike that suggested by the exponential form, our fitted value of s_e appears to be independent of bed stress within the range we investigate. Fig. 4.8a shows s_e data stay constant with changing the bed shear stress except for a few data points for threshold velocity $u_{th,10}$. On the other hand, we found the maximum entrainment occurs above the mean bed height and its distance from the mean bed height,$\tilde{z}_e$, to increase with bed shear stress (Fig. 4.8b), which is in contrast to what proposed by Wong et al. (2007).

After investigating the effect of choosing different threshold parameters n for the threshold velocity $u_{th,n}$ (Eq. 4.6) on the bed surface statistics, we found all the threshold velocities, excluding $u_{th,10}$ are capable of producing consistent results (Fig. 4.5, 4.6, 4.7).

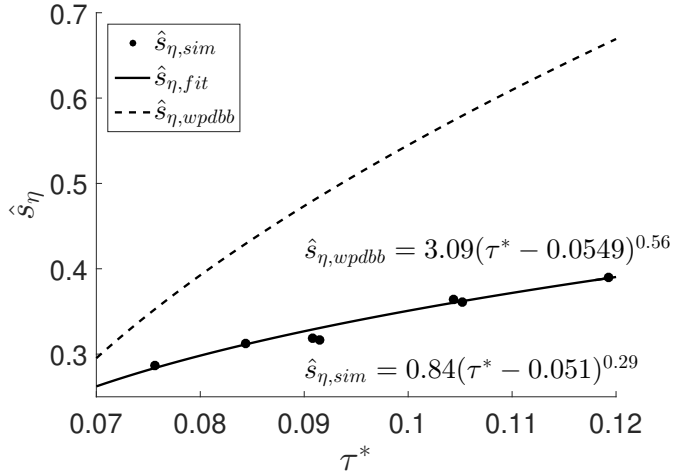

Figure 4.9: Power law fitting model for standard deviation of bed height variation against shields stress. Filled circles represents the calculated standard deviation from the simulations. Solid line represents our fitting model with $a_\eta = 0.84$ and $b_\eta = 0.29$ while the dashed line represents the fitting model suggested by Wong et al. (2007) with $a_\eta = 3.09$ and $b_\eta = 0.56$

We chose n=5 as the threshold velocity coefficient for the rest of this study (Eq. 4.9) because of the apparent independence of the results to the choice of this value near n=5 and also because this is closer to the range reported by Bridge and Dominic (1984) (Eq. 4.5). So, for the rest of this study, we use this to identify a particle as moving or part of the bed. In other words, a particle would be considered effectively stationary and therefore part of the bed at a particular time if its downstream velocity is less than a threshold value equal to:

$$u_{\mathrm{th},5} \equiv 5 \times (u_\tau - u_{\tau c}) \tag{4.9}$$

Using this threshold velocity, we fit a power law relationship between the standard deviation of the bed surface variations, $\hat{s}_\eta$, and the shields stress, $\tau^* - \tau_c^*$:

$$\hat{s}_{\eta,\mathrm{fit}} = a_\eta(\tau^* - \tau_c^*)^{b_\eta} \tag{4.10}$$

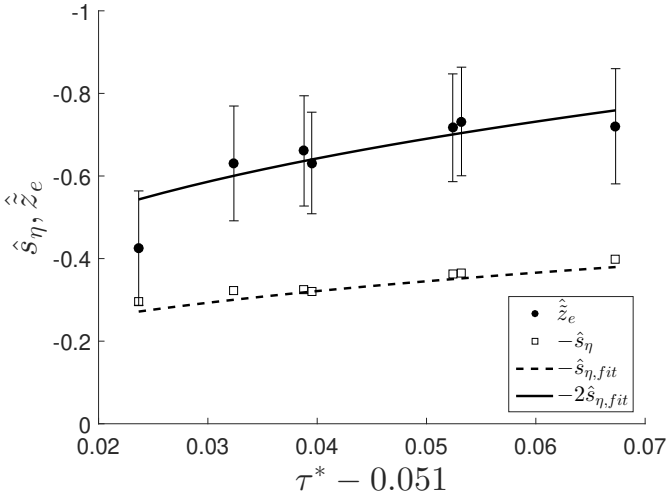

Figure 4.10: Normalized peak entrainment height, $\hat{\tilde{z}}_e$, and the normalized bed surface standard deviation, $\hat{s}_\eta$, as a function of excess Shields stress. Error bars show the standard deviation of entrainment height distribution, s_e in Eq. 4.8b and table 4.2. $\hat{s}_{\eta,fit}$ is our power law fitting model for the bed surface standard deviations, Eq. 4.10 and Fig. 4.6.

where τ_c^* is the reference Shields stress derived from the transport data (Eq. 4.4). This form is not unlike that suggested by the experimental data of Wong et al. (2007). On the other hand, our fit coefficients $a_\eta \approx 0.8$ and $b_\eta \approx 0.3$ are somewhat different than the experimental results of Wong et al. (2007) (see Fig. 4.9), as we discuss in more details in Chapter 5.

Furthermore, we plot the normalized peak entrainment height of particles, $\hat{\tilde{z}}_e = \tilde{z}_e/d_{50}$ using the threshold velocity defined in Eq. 4.9 with the corresponding $\hat{s}_\eta$ values versus the the shields stress, $\tau^* - \tau_c^*$, in Fig. 4.10.

Figure 4.10 shows the peak entrainment height scales with the bed surface roughness and occurs approximately $2 \times \hat{s}_\eta$ above the mean bed height. We discuss the implications of this result in Chapter 5. Table 4.2 summarizes the results of the bed surface statistics calculated using the threshold velocity defined in Eq. 4.9.

Table 4.2: Summary of statistical analyses of bed surface for 7 computational experiments of this study.

Run	τ^*	$\hat{s}_\eta$	$\hat{\tilde{z}}_e$ for $p_{e,gau}$	$\hat{s}_e$	$\hat{\tilde{z}}_e$ for $p_{e,exp}$
1	0.1193	0.393	-0.71	0.255	-0.79
2	0.1052	0.353	-0.77	0.276	-0.71
3	0.1044	0.374	-0.73	0.254	-0.74
4	0.0915	0.340	-0.70	0.238	-0.70
5	0.0908	0.330	-0.69	0.270	-0.67
6	0.0844	0.311	-0.62	0.254	-0.65
7	0.0757	0.296	-0.46	0.281	-0.60

4.2 Three Narrow Size Distributions

This section involves the extension of the research described in the previous section to our investigation of the sensitivity of our results to the absolute size of the particles keeping everything else constant. In this regard, we use the same DEM model in the previous section, in particular the same flow model (Fig. 3.2), to simulate the bedload transport of three different particle sizes with the median size of d_{50} = 4.12 mm, 7.1 mm, and 12 mm and with ρ_s= 2650 kg/m^3. More information about each particle size (e.g. geometric mean particle size and geometric standard deviation) are given in Table 4.3. To minimize the crystallization in the bed, we allow the particle size distribution to vary by approximately 10%, as described in Table 4.3. We note that we scale everything about our model with particle size. That is, the coefficients in the contact force model scale with particle size; the parameters in the log-law fluid model scale with particle size, and the size of the model flume scales with particle size."

For each particle size, we simulated the bedload transport for 12 different bed shear

Table 4.3: Particle size statistics.

d_{50} (mm)	d_g (mm)	σ_g	Size range (mm)
4.12	4.10	1.21	[2.08 - 6.20]
7.1	7.2	1.2	[4.82 - 9.60]
12	11.92	1.12	[9.50 - 14.5]

stresses as detailed in table 4.4. The channel size for each particle size distribution is about $50 \times d_{50}$ long and $12 \times d_{50}$ wide as we found in the previous section is the minimum size to produce results independent of channel size.

Table 4.4: Computational flow and bed parameters for different size particles.

Run	$d_{50}(mm)$	τ^*	k_s	z_1	q^*	$\eta(mm)$
1	(4.12,7.1,12)	0.1330	$3.5d_{50}$	$2d_{50}$	(0.054,0.053,0.068)	(21.71,36.64,60.10)
2	(4.12,7.1,12)	0.1250	$3.5d_{50}$	$2d_{50}$	(0.053,0.043,0.057)	(21.74,36.64,59.57)
3	(4.12,7.1,12)	0.1193	$3.5d_{50}$	$2d_{50}$	(0.047,0.041,0.048)	(21.67,36.68,59.31)
4	(4.12,7.1,12)	0.1052	$3.5d_{50}$	$2d_{50}$	(0.044,0.032,0.037)	(21.70,36.43,58.99)
5	(4.12,7.1,12)	0.1044	$3.5d_{50}$	$2d_{50}$	(0.039,0.033,0.037)	(21.67,36.62,58.95)
6	(4.12,7.1,12)	0.0960	$3.5d_{50}$	$2d_{50}$	(0.032,0.029,0.030)	(21.53,36.66,58.70)
7	(4.12,7.1,12)	0.0915	$3.5d_{50}$	$2d_{50}$	(0.033,0.022,0.037)	(21.66,36.47,58.48)
8	(4.12,7.1,12)	0.0908	$3.5d_{50}$	$2d_{50}$	(0.027,0.023,0.025)	(21.59,36.43,58.60)
9	(4.12,7.1,12)	0.0880	$3.5d_{50}$	$2d_{50}$	(0.026,0.020,0.021)	(21.54,36.56,58.52)
10	(4.12,7.1,12)	0.0844	$3.5d_{50}$	$2d_{50}$	(0.021,0.015,0.017)	(21.52,36.51,58.52)
11	(4.12,7.1,12)	0.0757	$3.5d_{50}$	$2d_{50}$	(0.016,0.010,0.011)	(21.49,36.41,58.33)
12	(4.12,7.1,12)	0.0710	$3.5d_{50}$	$2d_{50}$	(0.013,0.010,0.007)	(21.48,36.52,58.41)

For the rest of this section, similar to the previous section, we first present our results regarding the transport rate of particles. Then, we present the results associated with the bed surface and particle entrainment height distributions.

4.2.1 Transport rate

We calculated the transport rate for each set of the simulations using Eq. 4.1 and non-dimesnsionalize it using Eq. 4.2 $\left(q^* = \frac{q}{\sqrt{(s-1)gd_{50}}d_{50}}\right)$. Fig. 4.11 shows the time series of transport rate of two representatives ($\tau^* = 0.125$ and $\tau^* = 0.0915$) for each particle size.

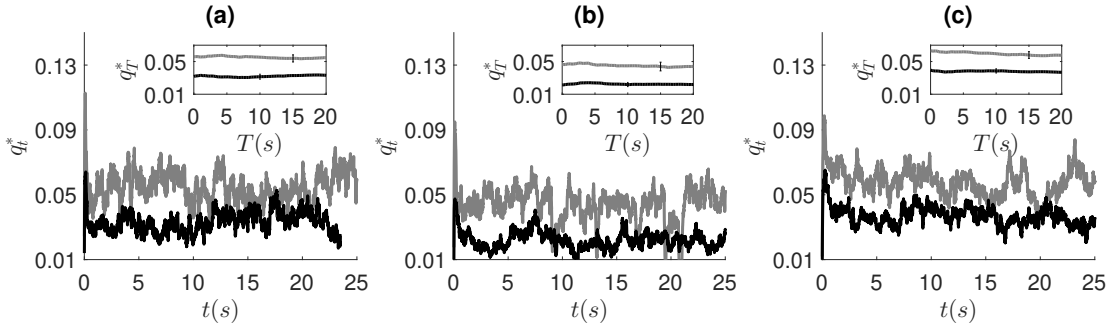

Figure 4.11: Time series of transport rate for two representatives (the gray line is for $\tau^* = 0.125$ and the black line is for $\tau^* = 0.0915$) for each particle size. (a) shows the time series for $d_{50} = 4.12mm$ particles size, (b) shows the time series for $d_{50} = 7.1mm$ particles size, and (c) shows the time series for $d_{50} = 12mm$ particles size. For each figure, the inset shows the average transport rate starting just after reaching the steady state conditions to time T after reaching the steady state. The error-bar shows the standard deviation of transport variations for 20 seconds after reaching the steady state conditions.

To find the transport rate model parameters (a_q and τ_c^* in Eq. 4.4) of each particle size, we follow the same procedure for all three particles we outlined in section 4.1. That is, we calculate the linearized least square fit of $q^{*2/3}$ vs τ^* (See Fig. 4.12 and Table. 4.5).

The small values of error in our fitting (RMSE values in Tab. 4.5) is promising to accept that our data fit well with linearized least square. In addition, we found a systematic changes in the coefficients of fitting (a_q and τ_c^*) among different size particles (See Fig. 4.12b and c). In particular, both a_q and τ_c^* increases as the size of the particles increases. These variations harken back to the variety of bedload transport relationships previously proposed for much wider ranges of conditions, as we mentioned briefly in

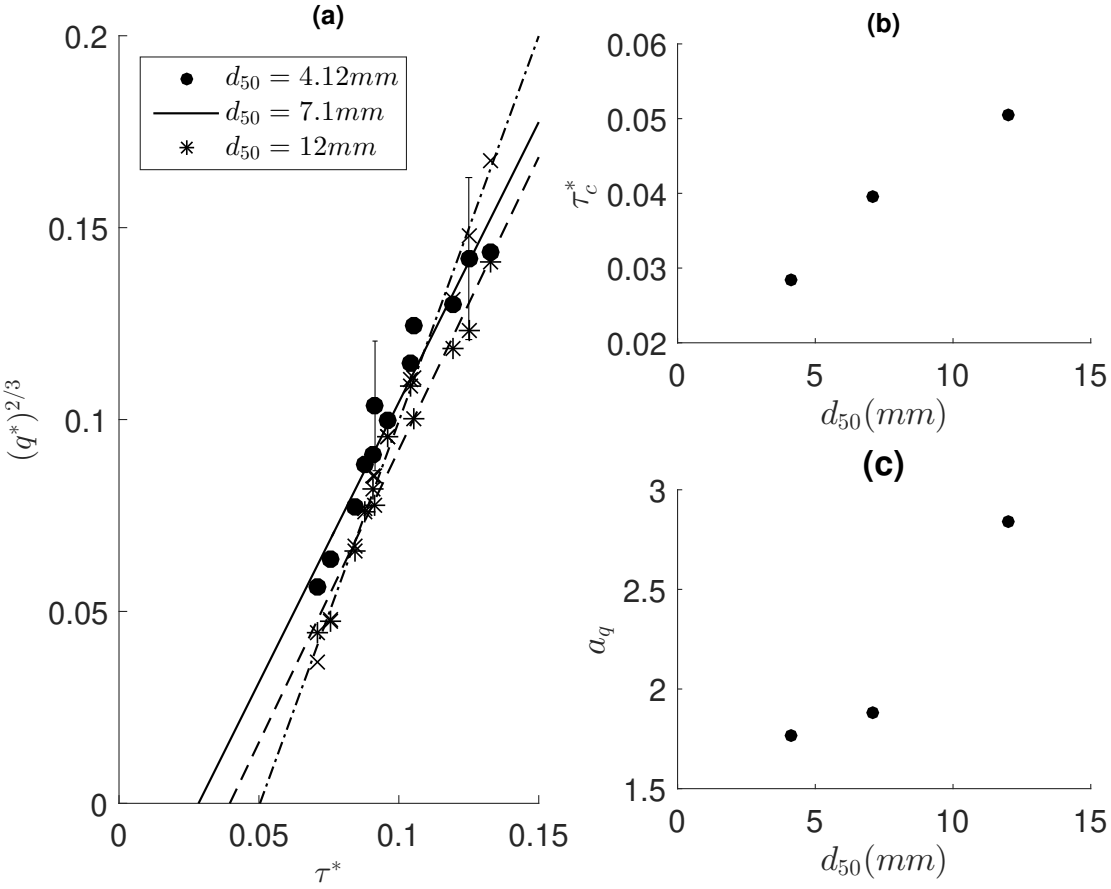

Figure 4.12: Linear least square fitting to transport data against the dimensionless bed shear stress, τ^*, to find the parameters of our transport model, $q^* = a_q \times (\tau^* - \tau_c^*)^{1.5}$, for each particle size.

the context of simulation results of Schmeeckle and colleagues (Schmeeckle and Nelson (2003); Schmeeckle (2014)). We discuss this in a bit more detail in Chapter 5.

In any case, for the results regarding the bed surface statistics that we report in this section, we use the values of fitting parameters in Table. 4.5.

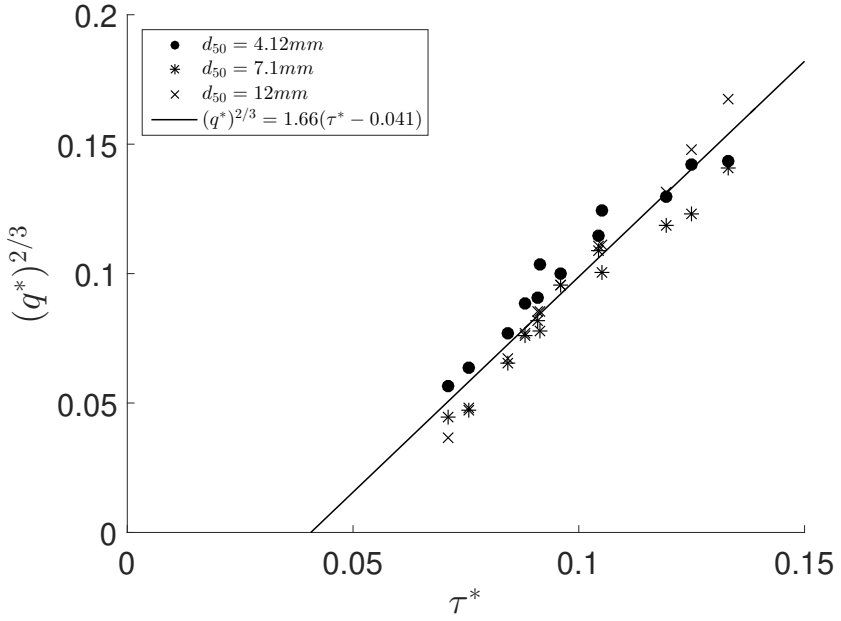

Figure 4.13: Linear least square fitting to transport data against the dimensionless bed shear stress, τ^*, to find the parameters of the transport model, $q^* = a_q \times (\tau^* - \tau_c^*)^{1.5}$, that fits to the transport rate of all three different size particles, $[a_q, \tau_c^*] = [1.66, 0.041]$.

Table 4.5: Computational flow and bed parameters. Last column gives the root mean square error (RMSE) of the linear fittings shown in Fig. 4.12.

d_{50} (mm)	a_q	τ_c^*	RMSE
4.12	1.77	0.0284	0.0063
7.1	1.88	0.0396	0.0054
12	2.84	0.0504	0.0034

4.2.2 Bed surface statistics

Here we investigate the effect of grain size on the bed surface variability results. To do so, we calculate the bed surface distribution of different size particles using the same procedure explained in section 4.1.2. In particular, to calculate the bed surface statistics, we use Eq. 4.9 to distinguish between the moving and the bed particles. Then, we divide the channel into 150 subsections (each a column of cross-sectional area $\approx 2\ d_{50} \times 2\ d_{50}$)

and use the same procedure in 4.1.2 to calculate the bed surface distributions. We plot this distribution for three representative simulations for each particle size in Fig. 4.14.

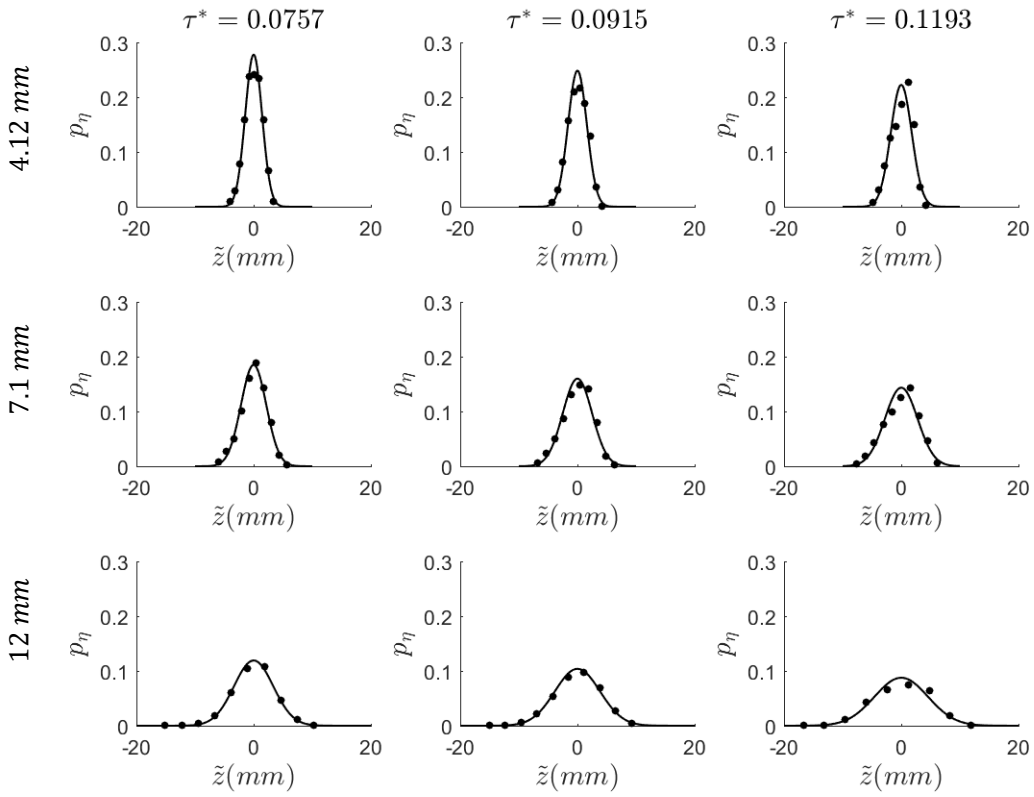

Figure 4.14: Three representatives of probability density distribution of bed height variations for each particle size. Filled circles represent the simulation data while the solid line represents the Gaussian fitting curve, $p_\eta(\tilde{z}|0, s_\eta^2)$. Table 4.6 shows the standard deviation of all the computational experiments designed for this section.

Figure 4.14 presents the probability distribution of the bed surface height for several cases. From this figure we can see that, as for the d_{50} =7.1 mm particles, for all the different particle systems the width increases with model shear stress. We can also see that the width increases for any particular shear stress as we increase the typical particle size in the mixture (top to bottom in Fig. 4.14). To investigate the quantitative dependence of particle size on the standard deviation of bed surface variations, we

normalize the standard deviation by the median particle size, $\hat{s}_\eta = s_\eta/d_{50}$, and plot these normalized values against the Shields stress, τ^*. We plot all systems together in Fig. 4.15 and then do so in Fig. 4.16 with a separately fitted exponential function for each system of particles. In Fig. 4.17, we plot the normalized s_η values of each particle size against the excess shields stress. We fit a power law relationship between the $\hat{s}_\eta = s_\eta/d_{50}$ and $\tau^* - \tau_c^*$ (Eq. 3.10b) and found the fitting coefficient of this unique power law relation ($a_\eta = 0.83$ and $b_\eta = 0.28$) are similar to that for the $d_{50} = 7.1$ mm particles alone. We discuss this more in next chapter.

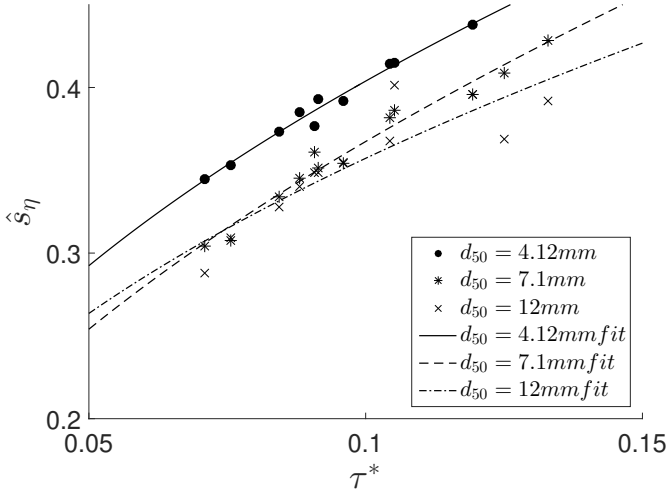

Figure 4.15: The standard deviation of the bed height variations against the Shields stress for particles of different size.

In the next section, we present the results regarding the entrainment statistics of different size particles to understand if these statistics, similar to the bed surface statistics, are only a function of hydraulic conditions when normalized by the median particle size.

4.2.3 Particle entrainment statistics

To determine the statistics of particle entrainment height for each particle size, we follow the definition of entrainment event used in section 4.1.3 (Eq. 4.7) to detect if a particle

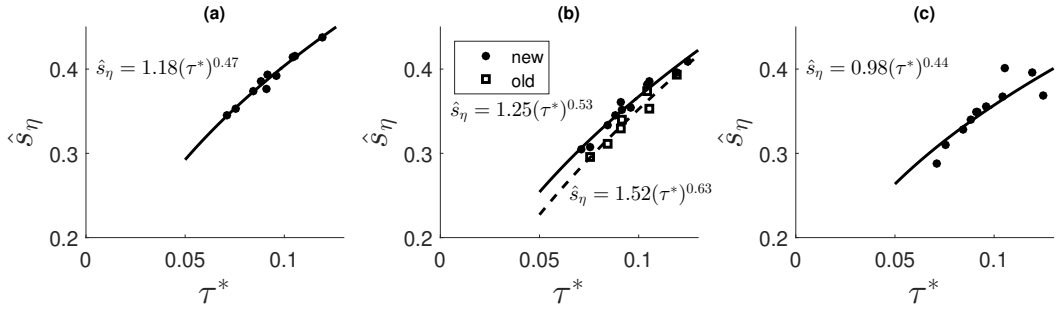

Figure 4.16: Power law fitting model for standard deviation of bed height variation, $\hat{s}_\eta$, against shields stress (τ^*): (a) for small size particles, $d_{50} = 4.12mm$, with fitting parameters $a_\eta = 1.18$ and $b_\eta = 0.47$, (b) for medium size particles, $d_{50} = 7.1mm$, with fitting parameters $a_\eta = 1.25$ and $b_\eta = 0.53$, (c) for big size particles, $d_{50} = 12mm$, with fitting parameters $a_\eta = 0.98$ and $b_\eta = 0.44$. Filled circles represents the calculated standard deviation from the simulations and solid line represents our fitting model.

is entrained. Then, following the same procedure described in 4.1.3, we calculate the entrainment height distribution of each particle size for different bed shear stresses.

Figure 4.18 shows the entrainment height distributions for three representative shear stresses for each particle size. Similar to what we found in the section 4.1, Fig. 4.18 shows the entrainment height distribution (p_e) well fit by Gaussian distribution for all the particle sizes and the peak of the entrainment occurs above the average bed height. Again, as is true of the standard deviation of the bed variations (Fig. 4.14), we found that the statistics of the entrainment height distribution depends on both the particle size distribution and hydraulic conditions (Fig. 4.18).

We calculate and plot the normalized peak entrainment height, $\hat{\tilde{z}}_e = \tilde{z}_e/d_{50}$, in Fig. 4.19 for each particle size.

Fig. 4.19 shows the peak entrainment height, $\hat{\tilde{z}}_e$, scales similarly with the bed surface roughness, $\hat{s}_\eta$, for $d_{50} = 4.12mm$ and $d_{50} = 7.1mm$ particles; However, the peak entrainment height of larger particles, $d_{50} = 12mm$, shows deviation from this relationship. Instead, we note that the peak entrainment height of $d_{50} = 12mm$ particles scales with the bed surface roughness, however, it scales as $\hat{\tilde{z}}_e = 1.5 \times \hat{s}_\eta$ instead of $\hat{\tilde{z}}_e = 2 \times \hat{s}_\eta$ (See Fig. 4.20).

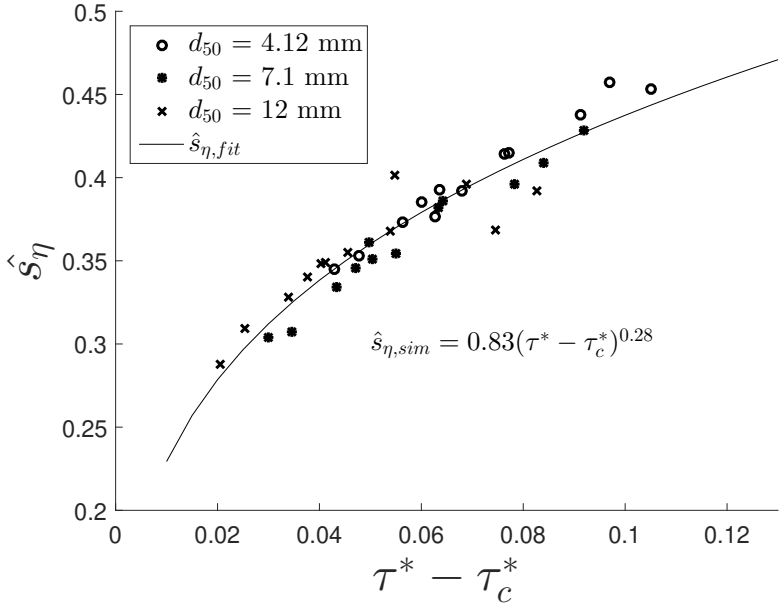

Figure 4.17: Power law fitting model for standard deviation of bed height variation against excess shields stress $(\tau^* - \tau_c^*)$ where τ_c^* is given in table 4.5 for each size. Solid line represents our fitting model with $a_\eta = 0.83$ and $b_\eta = 0.28$.

We note, similar to the previous section, the standard deviation of the entrainment height distributions, for all the different size particles, are bed stress independent (i.e. see Fig. 4.18) and for this reason we did not present these here; however, we include their values for each particle size and bed shear stress in Tab. 4.6. This table summarizes the results of this section regarding the bed surface and entrainment height distributions.

All the results presented to this point are for cases where we neglect the turbulent fluctuations. However, to understand the role of turbulent fluctuations on the bed surface statistics, we present the results for cases where we have turbulent fluctuations in the next section.

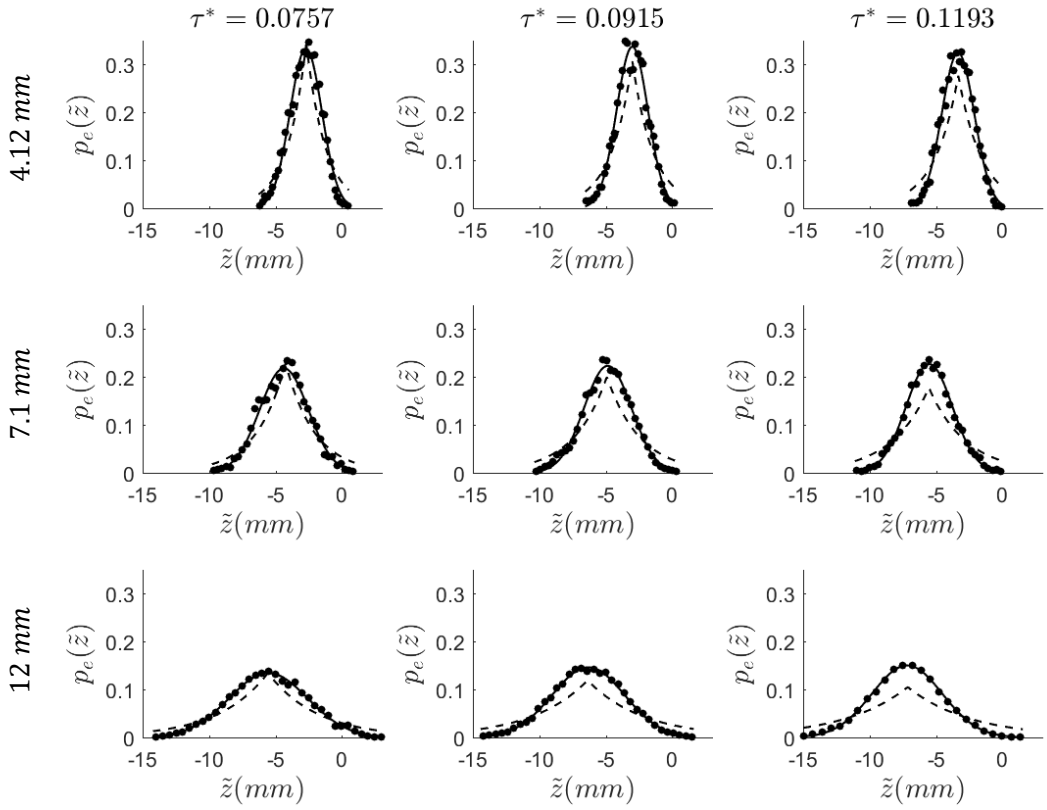

Figure 4.18: Three representative of entrainment height distributions for each particle size. Filled circles represent the simulation data; the solid line represents a Gaussian fitting curve, $p_e(\tilde{z}|\tilde{z}_e, s_e^2)$ (Eq. 4.8b), and the dashed line represents an exponential fitting curve, $p_e(\tilde{z}|\tilde{z}_e, s_\eta^2)$, suggested by Wong et al. (2007), (Eq. 4.8a). Table 2 shows the fitting parameters of these distributions.

4.3 Turbulence

In this section we investigate the sensitivity of our results to (1) the presence of turbulent-like velocity fluctuations and (2) some of the statistics of the velocity fluctuations themselves. Towards this goal, we use 4 different fluid models in this study. These fluid models are relatively simple compare to current advanced fluid models, for example that use large eddy simulations for the fluid and two-way coupling between fluid and

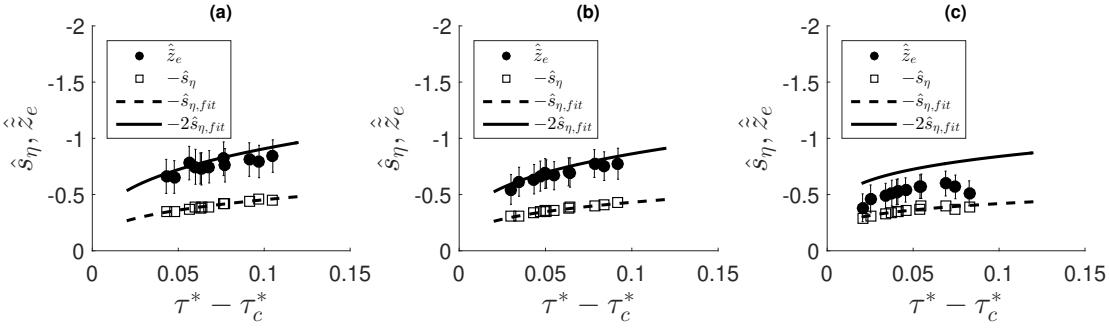

Figure 4.19: Normalized peak entrainment height, $\hat{\tilde{z}}_e$, and the normalized bed surface standard deviation, $\hat{s}_\eta$, as a function of the excess Shields stress for a) $d_{50} = 4.12mm$, b) $d_{50} = 7.1mm$, c) $d_{50} = 12mm$. Error bars show the standard deviation of the entrainment height distribution, $\hat{s}_e$. $\hat{s}_{\eta,fit}$ is the power law fitting specifically for each particle size, Fig. 4.16. Fitted values are included in Table 4.6.

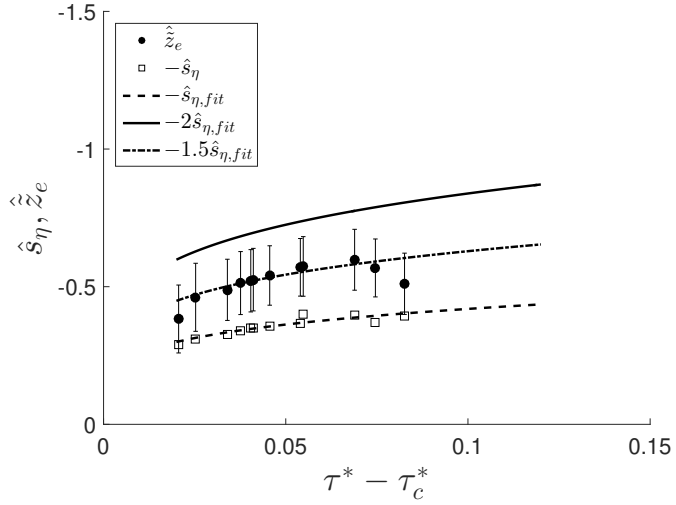

Figure 4.20: Normalized peak entrainment height, $\hat{\tilde{z}}_e$, and the normalized bed surface standard deviation, $\hat{s}_\eta$, as a function of the excess Shields stress for $d_{50} = 12mm$. Error bars show the standard deviation of the entrainment height distribution, $\hat{s}_e$. $\hat{s}_{\eta,fit}$ is the power law fitting (Eq. 4.8b and Table 4.6.

particles. In fact, our goal in using these fluid models, rather than reproduce, as well as possible, every detail in the field, is to isolate systematically some of these details to discover their influence on the outcomes.

In addition to our first steady fluid velocity model, in this section we present three

Table 4.6: Summary of statistical analyses of bed surface for 3 different particle sizes and 12 different hydraulic conditions .

Run	$d_{50}(mm)$	τ^*	$\hat{s}_\eta$	$\hat{\tilde{z}}_e$	$\hat{s}_e$
1	(4.12,7.1,12)	0.1330	(0.45,0.43,0.39)	(-0.84,-0.77,-0.51)	(0.29,0.28,0.22)
2	(4.12,7.1,12)	0.1250	(0.46,0.41,0.37)	(-0.79,-0.75,-0.57)	(0.29,0.26,0.21)
3	(4.12,7.1,12)	0.1193	(0.44,0.40,0.40)	(-0.81,-0.78,-0.60)	(0.30,0.25,0.22)
4	(4.12,7.1,12)	0.1052	(0.42,0.39,0.40)	(-0.76,-0.70,-0.57)	(0.30,0.26,0.22)
5	(4.12,7.1,12)	0.1044	(0.41,0.38,0.37)	(-0.82,-0.70,-0.57)	(0.30,0.25,0.21)
6	(4.12,7.1,12)	0.0960	(0.39,0.35,0.36)	(-0.75,-0.68,-0.54)	(0.29,0.25,0.22)
7	(4.12,7.1,12)	0.0915	(0.39,0.35,0.35)	(-0.73,-0.68,-0.53)	(0.29,0.25,0.23)
8	(4.12,7.1,12)	0.0908	(0.38,0.36,0.35)	(-0.73,-0.69,-0.52)	(0.28,0.27,0.23)
9	(4.12,7.1,12)	0.0880	(0.39,0.35,0.34)	(-0.75,-0.66,-0.51)	(0.31,0.27,0.23)
10	(4.12,7.1,12)	0.0844	(0.37,0.33,0.33)	(-0.80,-0.64,-0.49)	(0.30,0.26,0.22)
11	(4.12,7.1,12)	0.0757	(0.35,0.31,0.31)	(-0.66,-0.61,-0.46)	(0.29,0.26,0.25)
12	(4.12,7.1,12)	0.0710	(0.35,0.30,0.29)	(-0.66,-0.55,-0.38)	(0.30,0.27,0.25)

models that incorporate representative velocity fluctuations into our simple DEM model to do so. Then we present the results to help us understand the relative role of turbulent fluctuations and average flow velocity in our bed surface statistics.

4.3.1 Fluid Models

In this section, we describe the four fluid models we use in this study to investigate the relative role of the average flow velocity and turbulent fluctuations on the bed surface statistics and sediment transport rate.

We start by introducing basic notation we will use in the framework of what is commonly called Reynolds decomposition:

$$u_f = \overline{u}_f + u'_f \tag{4.11}$$

where u_f is a local and instantaneous fluid velocity, $\overline{u}_f$ is an average fluid velocity and u'_f is the difference between the two, what we refer to (as is common) as a "velocity fluctuatio". Through theoretical formulations and experimental validations, researchers have developed expressions for each of the term on the right hand side of equation 4.11, which we use for our fluid models. We introduced the logarithmic form for the velocity profile in Chapter 3 (Eq. 3.10aa). We maintain this form for $\overline{u}_f$ for all four models. For the form of the fluctuations, we first consider how the standard deviation of the mean fluctuation magnitude varies with height above the bed surface. Several forms have been proposed (Nakagawa et al. (1975); Nezu and Nakagawa (1993); Ghesemi et al. (2019); Nikora (2005)).

For the velocity fluctuations, researchers have proposed different expressions for turbulent intensities over gravel-bed rivers. Nakagawa et al. (1975) proposed a power law relation for turbulent intensities in the streamwise direction using the log-law of the wall for the energy equilibrium region in the following form:

$$\frac{\sqrt{\overline{u'^2_f}}}{u_\tau} = B(z/H)^{-1/6}(1 - z/H)^{1/3} \tag{4.12}$$

where u'_f is the velocity fluctuations in the streamwise direction, u_τ is the shear velocity, z is the distance from the zero-plane velocity, and H is the flow depth. Later, Nezu and Nakagawa (1993) proposed an exponential function to scale the turbulent intensities in downstream, vertical and cross-stream directions. Using the turbulent energy equation ($G = \epsilon + T_D + P_D + V_D$, where G is turbulent energy generation, ϵ is the total energy dissipation, T_D is the turbulent energy diffusion, P_D is the pressure energy diffusion, and V_D is the viscous diffusion) and $k - \epsilon$ turbulence model and neglecting

the viscous term, they proposed semi-theoretical exponential relations for the turbulence intensities:

$$\frac{\sqrt{\overline{u_f'^2}}}{u_\tau} = D_u exp(-z/H) \tag{4.13a}$$

$$\frac{\sqrt{\overline{v_f'^2}}}{u_\tau} = D_v exp(-z/H) \tag{4.13b}$$

$$\frac{\sqrt{\overline{w_f'^2}}}{u_\tau} = D_w exp(-z/H) \tag{4.13c}$$

where v' and w' are the velocity fluctuations in the vertical and cross-stream directions, respectively. D_u, D_v, and D_w are constants and found empirically to be 2.3, 1.63, and 1.27 (Nezu and Nakagawa (1993)).

Another scaling method for the turbulent intensities rooted in the spectral scaling. Perry et al. (1986, 1987) proposed the following relation for the streamwise direction of turbulent energy by integrating the spectral energy density of turbulent flow over all wave-numbers and neglecting the viscous region in the following form:

$$\frac{\overline{u_f'^2}}{u_\tau^2} = B - A(\log z/H) - C(z_+)^{-1/2} \tag{4.14}$$

where A and C are universal constants, and B is a large-scale characteristic constant. The first term on the right hand side of equation 4.14 is for the first region of spectrum which is associated with the largest eddies within the turbulent flows or where the energy production exists. The second term is associated with the intermediate eddies where energy production and cascade energy transfer co-exists. The third term is associated with relatively small eddies that correspond to the "*Kolomogorov*" region and $z_+ =$

zu_τ/ν. Several researchers (i.e. Nikora (2005); Ghasemi (2016); Ghesemi et al. (2019)) have used this form because of its more inclusive representation of the different forms of the fluctuations in the different regions of the flow.

For simplicity for our study, we use the expressions proposed by Nezu and Nakagawa (1993) (Eq. 4.13) to model turbulent fluctuations through a random processes. In particular, for this fluid model, we introduce the velocity fluctuations in the downstream and vertical directions by the following equations:

$$u'(t) = r_u\sqrt{\overline{u_f'^2}} \tag{4.15a}$$

$$w'(t) = r_w\sqrt{\overline{w_f'^2}} \tag{4.15b}$$

where r_u and r_w are random numbers that we choose in a manner from one of three ways, as described below, under the subheadings "Fluid model 2, Fluid model 3, and Fluid model 4".

For the results we report here, we include only fluctuations in the vertical and streamwise direction. We neglect the fluctuations in the spanwise direction as Ghasemi (2016) found the effects of these fluctuations considerably smaller than those in the normal and downstream directions (i.e. $(\overline{u_f'v_f'})$ and $(\overline{v_f'w_f'})$ are about an order of magnitude smaller than $(\overline{u_f'w_f'})$).

Fluid model 1: no fluctuations

The first fluid models used in this study has already been described in detail in Chapter 3 and used for the results in the earlier sections of this chapter. As we mentioned in Chapter 3, turbulent flows over gravel beds, the downstream velocity profile is closely described by a logarithmic relationship. For the rest of the simulations, we still use this relationship for $\overline{u}_f$.

Fluid model 2: fluctuations with uniform distribution

To investigate the role of turbulent fluctuations on the bed surface statistics and transport rate, we first consider the form of the average fluctuation magnitude as it varies with height above the bed. We introduce these velocity fluctuations into our fluid models through random processes that follow the expressions proposed for these fluctuations.

For the second fluid model we added fluctuations in the simplest manner possible. We chose r_u and r_w (Eqs. **??**) for each time step from a uniform distribution between -0.5 and 0.5.

Fluid model 3: fluctuations with normal distribution

This fluid model is similar to fluid model 2 except that the random numbers r_u and r_w are chosen from a standard Gaussian distribution. We note here that this may be a more appropriate baseline model for the fluctuations based on the Central-Limit Theorem (Pope (2001)). Specifically, the Central-Limit Theorem states that when independent random variables are added, their properly normalized sum tends toward a normal distribution even if the original variables themselves are not normally distributed. For the case of turbulent flows, it means if we repeat an experiment N times and record the velocity at a particular location and time and take an ensemble average, the ensemble average (which itself is a random number) should follow a Gaussian distribution as N tends to infinity.

Since all the computational experiments reported in this study are simulated in FORTRAN, we cannot generate Gaussian distributions from the default built-in functions. Instead, we generate the Gaussian distributions by, first, generating a several random numbers that follow uniform distributions. Then, we transform these random numbers to comprise two sets of standard Gaussian distributions and select the random variables r_u and r_w from these new generated distributions.

Fluid model 4: correlated fluctuations with normal distribution

Fluid model 4 uses a Gaussian distribution from which to choose r_u and r_w (like model 3), and it forces them to be correlated in the same manner shown to be important for sediment transport under certain circumstances (McLean et al. (1994)).

Fluid models 2 and 3 consider the turbulent fluctuations, however, these models introduce the fluctuations without providing any correlations between them. We provide correlations between the random numbers, r_u and r_w by selecting them from a standard bi-variate Gaussian distribution:

$$f(r_u, r_w) = \frac{1}{\sqrt{2\pi}} exp\left(-\frac{r_u^2}{2}\right) \frac{1}{\sqrt{2\pi}\sqrt{1-\gamma_{uw}^2}} exp\left[\frac{(r_w - \gamma_{uw} r_u)^2}{2(1-\gamma_{uw}^2)}\right] \tag{4.16}$$

Here $f(r_u, r_w)$ represents the probability density function of the bi-variate Gaussian distribution with mean and covariance matrix as:

$$\mu = \begin{vmatrix} \mu_u = 0 \\ \mu_w = 0 \end{vmatrix} \tag{4.17a}$$

$$\Sigma = \begin{vmatrix} \sigma_u^2 = 1 & \gamma_{uw}\sigma_u\sigma_w \\ \gamma_{uw}\sigma_u\sigma_w & \sigma_w^2 = 1 \end{vmatrix} \tag{4.17b}$$

Here, μ_u, μ_w, σ_u, and σ_w are the mean and standard deviation of r_u and r_w random variables. γ_{uw} represents the cross-correlation between r_u and r_w. For the results we present here, we use the following equation (Yeganeh et al. (2000); Yeganeh-Bakhtiary et al. (2009)):

$$\gamma_{uw} = \frac{\overline{u'_f w'_f}}{\sqrt{\overline{u'^2}}\sqrt{\overline{w'^2}}} \tag{4.18}$$

Here, ($\overline{u'_f w'_f}$) often called the Reynolds shear stress and is related to other dynamic variables according to (Nezu and Nakagawa (1993)):

$$\tau(z) = -\rho_f \overline{u'_f w'_f} + \nu \frac{\partial u_f}{\partial z} \tag{4.19a}$$

$$\tau(z) = \rho_f u_\tau^2 (1 - z/H) \tag{4.19b}$$

Here, $\tau(z)$ is the total shear stress at height z above the bed. ρ_f is the fluid density, ν is the fluid kinematic viscosity, and $\frac{\partial u_f}{\partial z}$ represents the instantaneous shear rate.

Re-arranging the Eq. **??**, we can determine the Reynolds shear stress by the following equation:

$$-\overline{u'_f w'_f} = \nu \frac{\partial u_f}{\partial z} - u_\tau^2 (1 - z/H) \tag{4.20}$$

A combination of equations 4.13, 4.18, and 4.20 leads to the following relationship for the cross-correlation, γ_{uw}.

$$\gamma_{uw} = \frac{\frac{\nu}{u_\tau^2} \frac{\partial u_f}{\partial z} - (1 - z/H)}{(2.3)(1.27) exp(-2z/H)} \tag{4.21}$$

To generate bi-variate Gaussian distribution in FORTRAN, we follow the steps we took to develop the random numbers for Model 3 by first generating two Gaussian distributions. Then, to provide a correlation between these two series of Gaussian

distributions, we need to calculate the eigenvalues and eigenvectors of the covariance matrix of $f(r_u, r_w)$, which vary by z, and used the following equation to transform a pair of uncorrelated random numbers (r_u, r_w) to correlated random numbers (r'_u, r'_w):

$$r' = \lambda^{1/2} \Phi r \tag{4.22}$$

where r' is the transformed random number, λ is the diagonal matrix made up of the eigenvalues of covariance matrix, Φ is the matrix of eigenvectors and r is the original random number. Schematic representation of our step by step method in generating turbulence fluctuations is shown in figure 4.21.

4.3.2 Computational Experiments

To investigate the role of turbulent fluctuations on the bed surface statistics, entrainment height and transport characteristics, we perform several computational experiments using the fluid models introduced in the previous section. We perform the simulations on only one particle size distribution with median particle size, $d_{50} = 7.1mm$, that we use in section 4.1 to compare directly with results from Wong et al. (2007). Similar to the previous section, we simulated the bedload transport for 12 different bed shear stresses, ranging from $\tau^* = 0.071$ to $\tau^* = 0.133$, for each fluid model (Tab. 4.7).

Table 4.7: Computational flow parameters for investigating the role of turbulent fluctuations on the bed surface statistics.

Set Name	$FluidModel$	τ^*	k_s	z_1	$H(cm)$
F1-Z2d	1	0.071 - 0.1330	$3.5d_{50}$	$2.00d_{50}$	N/A
F2-Z2d	2	0.071 - 0.1330	$3.5d_{50}$	$2.00d_{50}$	10
F3-Z2d	3	0.071 - 0.1330	$3.5d_{50}$	$2.00d_{50}$	10
F4-Z2d	4	0.071 - 0.1330	$3.5d_{50}$	$2.00d_{50}$	10

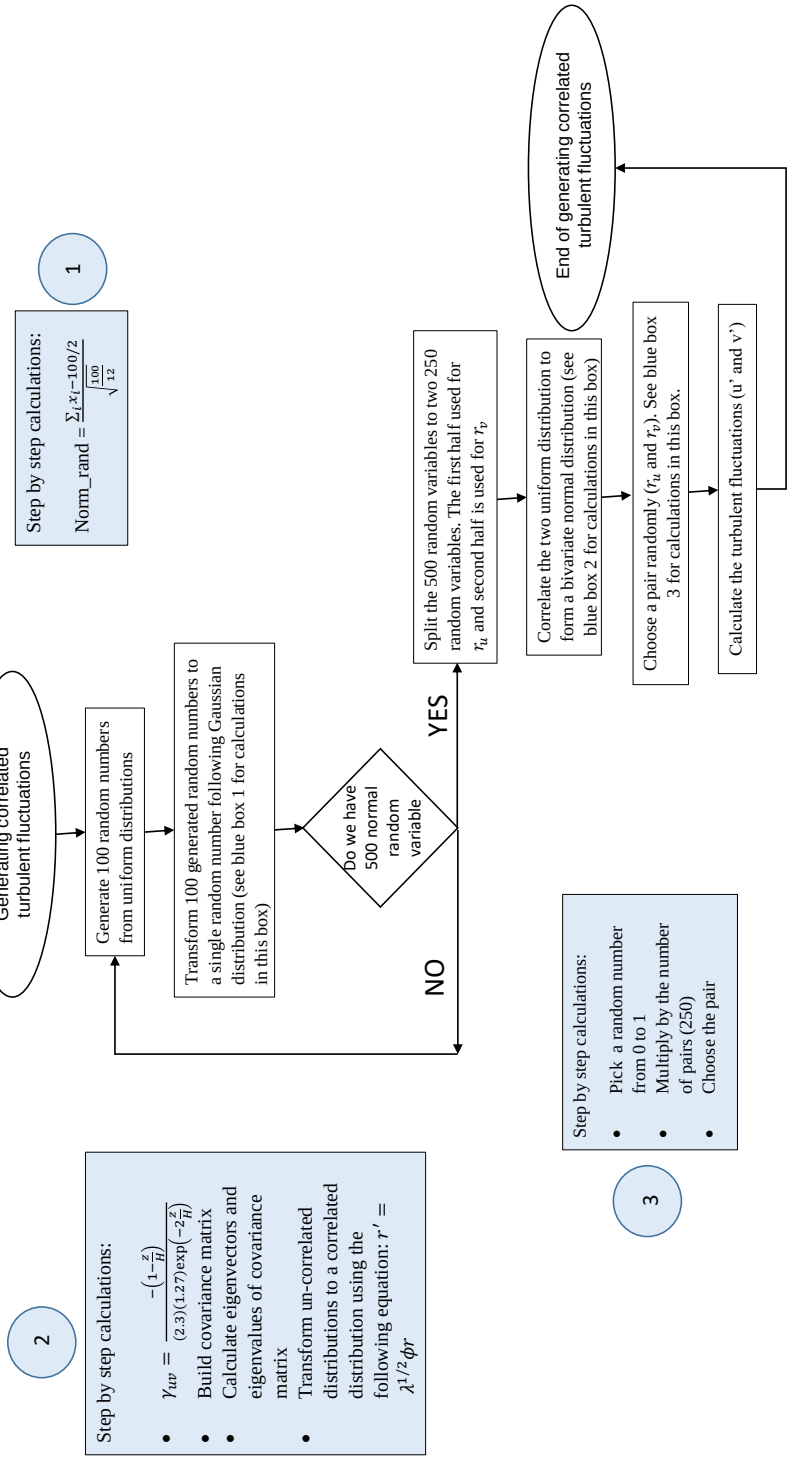

Figure 4.21: A flow chart to show step by step our methodology in generating correlated turbulent fluctuations.

Similar to the previous sections, in the next section, we first present the results regarding the transport rate of particles. Then, we present the bed surface and entrainment height statistics of each set of the simulations for the rest of this section.

4.3.3 Transport rate

Following the same procedure from previous sections, we calculate the transport rate for each simulations using Eq. 4.1 and normalize it using Eq. 4.2. The channel size for all the simulations reported in this section, as in section 4.1, is equal to 350 mm long and 85 mm wide.

Fig. 4.22 shows the transport rate time series of two representative simulations ($\tau^* = 0.0915, 0.125$) from each fluid model.

As clear in Fig. 4.22, the transport rate increases in the presence of turbulent fluctuations (especially for fluid model 3 and 4). This finding is in agreement to many studies that have shown the role of near bed turbulence on an increase in sediment transport rate (Grass (1983); Nelson et al. (1995); Sumer et al. (2003)).

To find the parameters of our transport rate model, similar to the previous sections, we assume the normalized transport rate, q^*, scales roughly with the bed shear stress as: $q^* \sim \tau^{*1.5}$ and fit a linearized least square model between $q^{*2/3}$ and τ^*.

Fig. 4.23 shows $q^{*2/3}$ against τ^* with a linearized least square fit to each fluid model. The error bars in this figure show the variations in the average value for transport rate for 20 seconds of simulations under steady-state conditions for two representatives of fluid model 1 and 4. These error bars are the same as those shown in the insets of Fig. 4.22. Table 4.8 shows the coefficient of fitting for each fluid model. We note that, the reference shear stress decreases when we introduce the turbulent fluctuations, , while the slope is similar for all.

In the next section, we present the results regarding the bed surface variations and the influence of turbulent fluctuations on these variations.

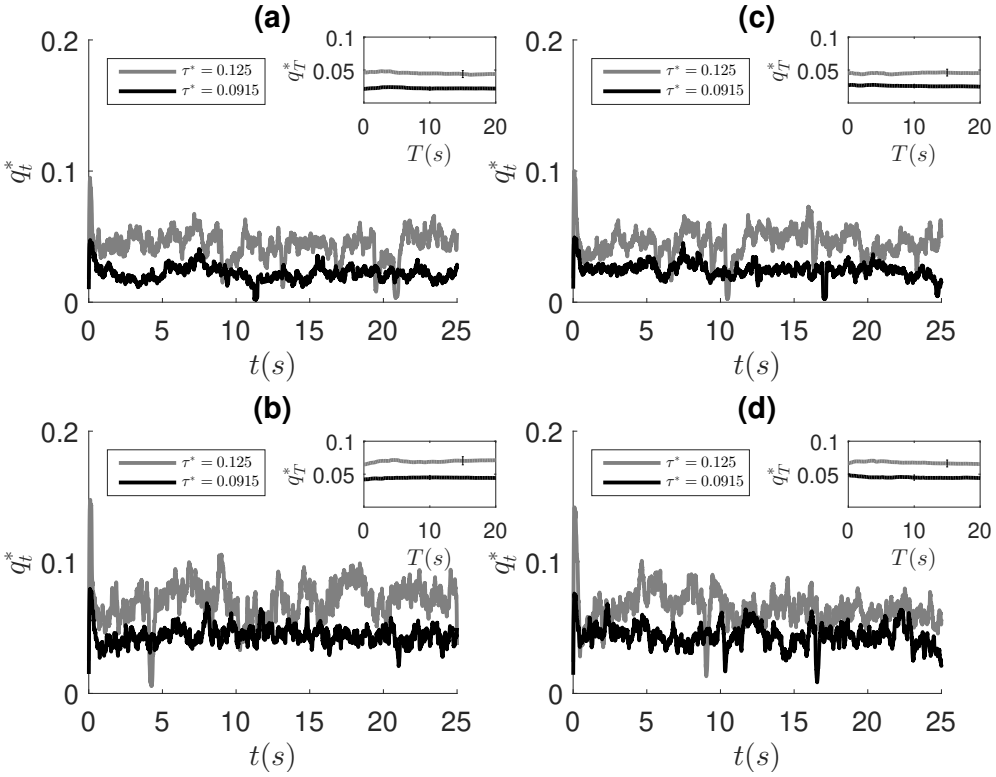

Figure 4.22: Time series of transport rate for two representative simulations for a) F1-Z2d model, b) F2-Z2d model, c) F3-Z2d model, and d) F4-Z2d model. The bed shear stress for black line is $\tau^* = 0.0915$ and for gray line is $\tau^* = 0.125$. The inset in each plot shows the average transport rate starting just after reaching the steady state to time T after reaching steady state. The error-bar in the inset shows the standard deviation of transport variations for 20 seconds after reaching the steady state conditions.

4.3.4 Bed surface statistics

In this section, we present the bed surface distribution for different fluid models. To calculate these distributions, we follow the procedure explained in the previous sections. We plot a representative of bed surface distribution for each fluid model in Fig. 4.24.

Fig. 4.24 shows the bed surface variations still follow the Gaussian distribution in the presence of turbulent fluctuations. In addition, it shows the variations, (s_η), of these distributions depends slightly on the presence of the turbulent fluctuations (i.e. compare plot (a) with plot (d) where plot (d) has a slightly wider distribution). We

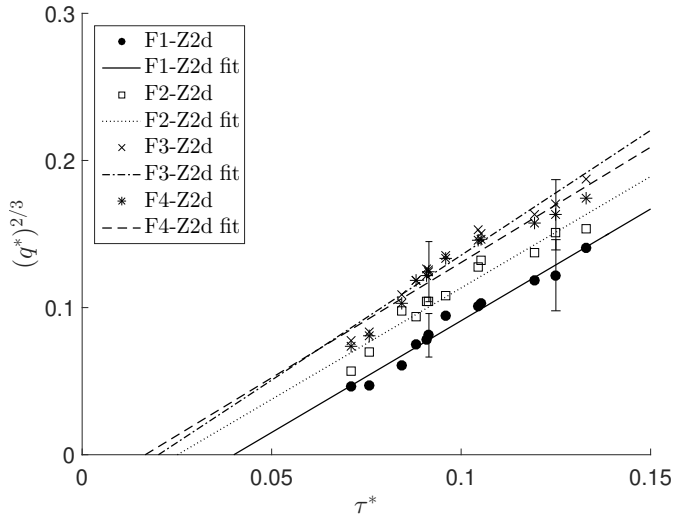

Figure 4.23: Linear least square fitting to transport data, $q^{*2/3}$ against the dimensionless bed shear stress, τ^*, to find the parameters of the transport model, $q^* = a_q \times (\tau^* - \tau_c^*)^{1.5}$, (Eq/ 4.4. The error bars show the variations in the average transport rate over 20 seconds of the simulations.

Table 4.8: Transport parameters for different fluid model.

Set name	Fluid model	z_1	a_q	τ_c^*
F1-Z2d	1	$2d_{50}$	1.87	0.040
F2-Z2d	2	$2d_{50}$	1.86	0.025
F3-Z2d	3	$2d_{50}$	2.21	0.020
F4-Z2d	4	$2d_{50}$	1.96	0.017

not here that this variation seems significantly less than that due to the change in bed shear stress we investigated. (i.e. compare Fig. 4.24 with Fig. 4.5). We discuss this more in Chapter 5.

We plot the standard deviation of the bed surface variations at each bed shear stress for each fluid model and plot the normalized values ($\hat{s}_\eta = s_\eta/d_{50}$) versus Shields stress on Fig. 4.25.

Fig. 4.25 shows the manner in which the magnitude of the bed surface variations at the same bed shear stress depends on the presence of turbulent fluctuations. Similar

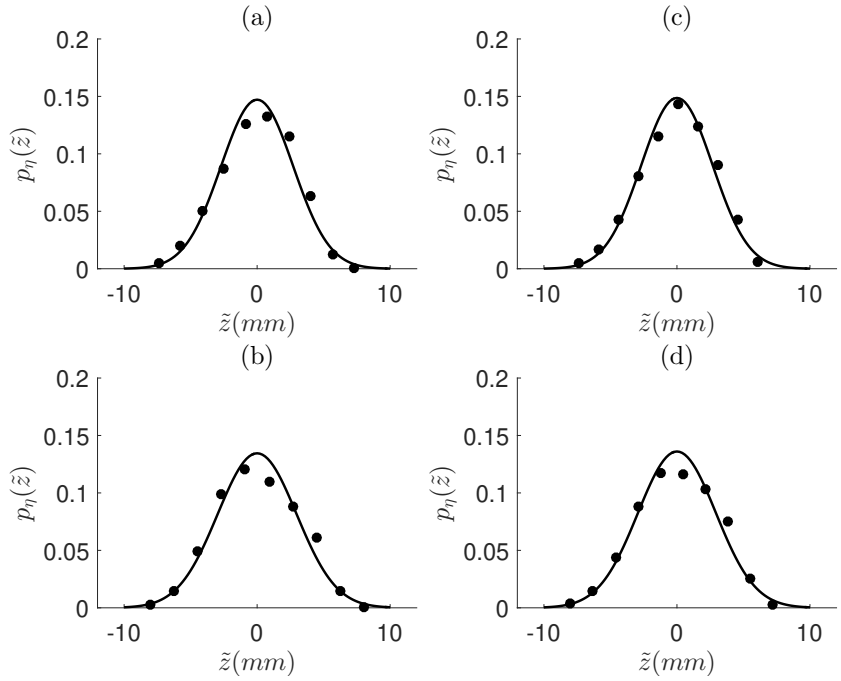

Figure 4.24: A representative ($\tau^* = 0.1044$) of probability density distribution of bed height variations for each fluid model: (a) F1-Z2d, (b) F2-Z2d, (c) F3-Z2d, and (d) F4-Z2d. Filled circles represent the simulation data while the solid line represents the Gaussian fitting curve, $p_\eta(\tilde{z}|0, s_\eta^2)$.

to the section 4.2, we fit a power law relation between $\hat{s}_\eta$ and τ^* and plot in Fig. 4.26. Despite the differences between the $\hat{s}_\eta$ values in Fig. 4.25, the fittings in Fig. 4.26 does not reveal any systematic changes between different fluid model at first glance. we discuss this more in Chapter 5,

In previous section, we found the normalized standard deviation of the bed surface variations ($\hat{s}_\eta$) for different size particles follows a similar trend when plotted against the excess Shields stress, $\tau^* - \tau_c^*$. To find out if this is true in the presence of turbulent fluctuations, we fit a power law relation between the $\hat{s}_\eta$ values and $\tau^* - \tau_c^*$ and plot in Fig. 4.27. Surprisingly, Fig. 4.27 shows a similar power law relation found in previous sections for the cases without the presence of turbulence. This is an interesting finding as it indicates the only important factor in determining the bed surface variations is the

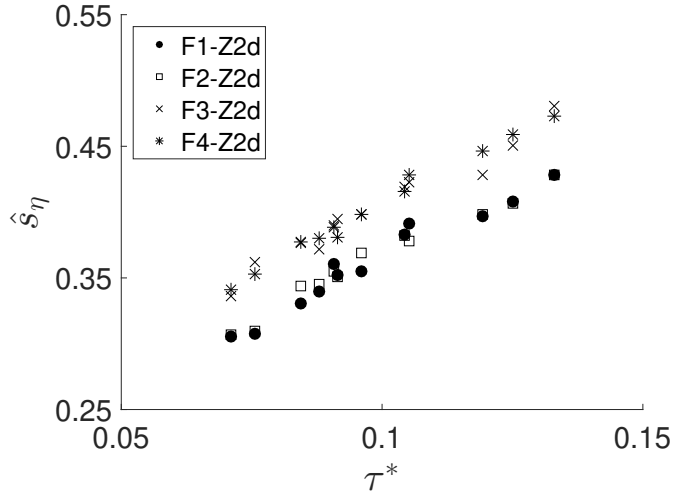

Figure 4.25: Standard deviation of bed surface variations for different fluid models as a function of the Shields stress.

excess Shields stress.

4.3.5 Particle entrainment statistics

The results of previous sections showed that the entrainment height distribution follows a Gaussian distribution and its first moment of statistics scales with the standard deviation of the bed surface height. To understand if these are true in the presence of turbulent-like fluctuations, we follow the procedure described in previous sections to calculate the entrainment height distributions for the each fluid model presented in this section. In particular, we use the definition of entrainment event (Eq. 4.9) to detect the entrained particles. Then, we record their vertical location, just prior to their entrainment. Using this information, we calculate the entrainment height distribution followed the procedure described in details before. Fig. 4.28 shows this distribution for a representative ($\tau^* = 0.1044$) of each fluid model.

As clear in Fig. 4.28, the entrainment height distributions, still, follow a Gaussian distribution in the presence of turbulent fluctuations. However, the standard deviation of the entrainment height distributions, s_e, increases in the presence of turbulent

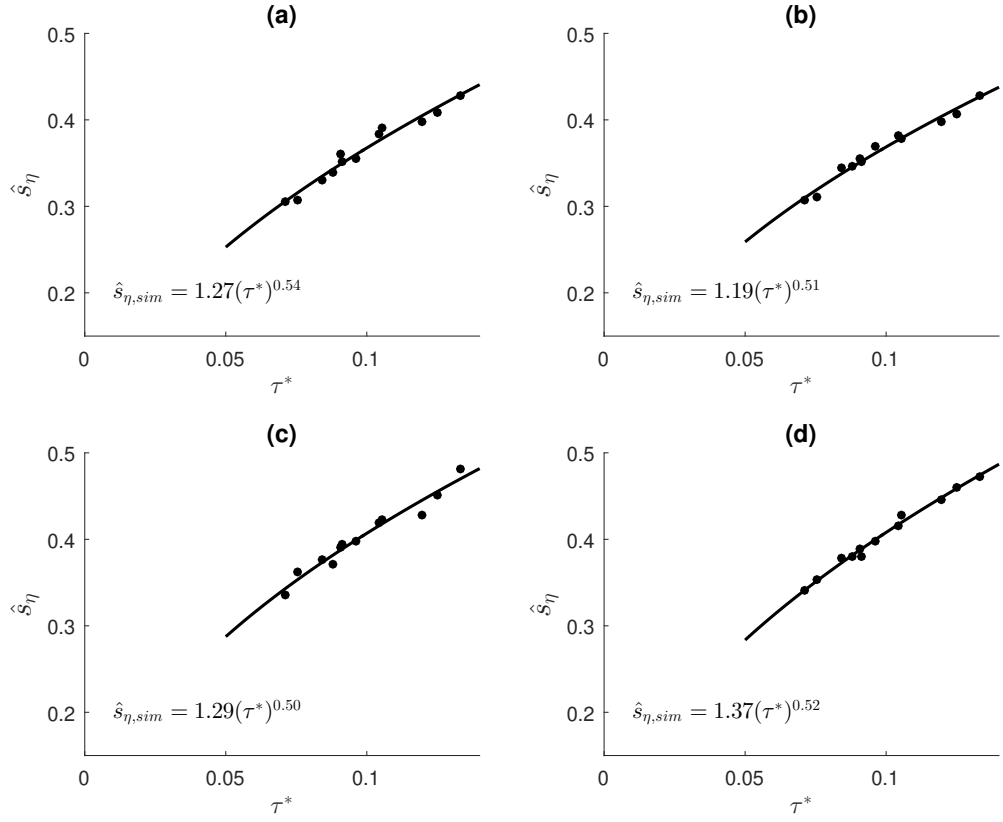

Figure 4.26: Power law fitting model for standard deviation of bed height variations, $\hat{s}_\eta$, against Shields stress (τ^*): (a) for model fluid 1 with fitting parameters $a_\eta = 1.27$ and $b_\eta = 0.54$, (b) for model fluid 2 with fitting parameters $a_\eta = 1.19$ and $b_\eta = 0.51$, (c) for model fluid 3 with fitting parameters $a_\eta = 1.29$ and $b_\eta = 0.5$, (d) for model fluid 4 with fitting parameters $a_\eta = 1.37$ and $b_\eta = 0.52$, .

fluctuations. We plot the standard deviation of the entrainment height distribution for each fluid model as a function of the Shields stress in Fig. 4.29. This figure shows the standard deviation of entrainment height distribution is bigger in the presence of turbulence; yet, similar to the previous results, they are independent of bed shear stress regardless of the presence or absence of turbulence.

To investigate the effect of turbulent fluctuations on the peak entrainment height and to understand if this height still scales with the standard deviation of the bed surface height in the presence of turbulent fluctuations, we calculate the first moment

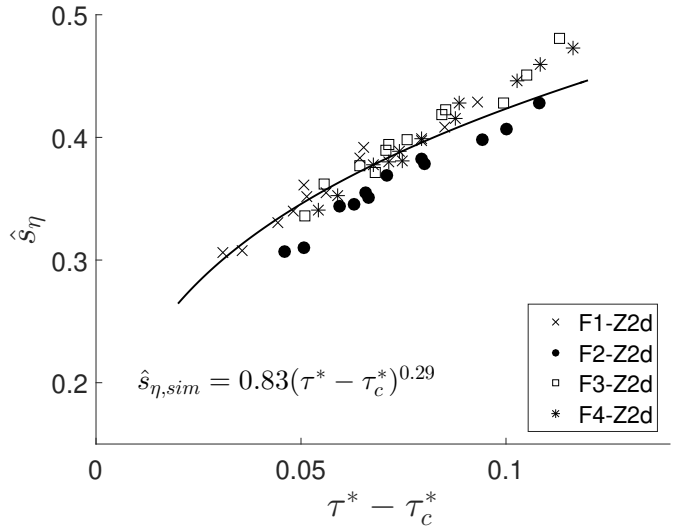

Figure 4.27: Power law fitting model for standard deviation of bed height variation against excess Shields stress ($\tau^* - \tau_c^*$) where τ_c^* is given in table 4.8 for each fluid model. Solid line represents our fitting model with $a_\eta = 0.83$ and $b_\eta = 0.29$.

of the entrainment height distribution (which represent the peak entrainment height location) and plot in Fig. 4.30 for each fluid model.

Similar to the results of the entrainment height statistics in the previous sections, Fig. 4.30 shows the peak entrainment height depends on the bed shear stress and increases as the bed shear stress increases. More suprisingly is that the normalized peak entrainment height, $\hat{\tilde{z}}_e$ still scales with the normalized bed surface roughness, $\hat{s}_\eta$, in the presence of turbulent fluctuations as: $\hat{\tilde{z}}_e \sim 2 \times \hat{s}_\eta$.

The consistency of our results between the bed surface roughness and peak entrainment height, regardless of the presence of turbulent fluctuations is surprising and promising that there may be a link between the vertical statistics of the bed and longitudinal transport rate of particles. We will discuss the possibility of the existence of this link in the next chapter.

We end this chapter by summarizing the results of this section in table 4.9.

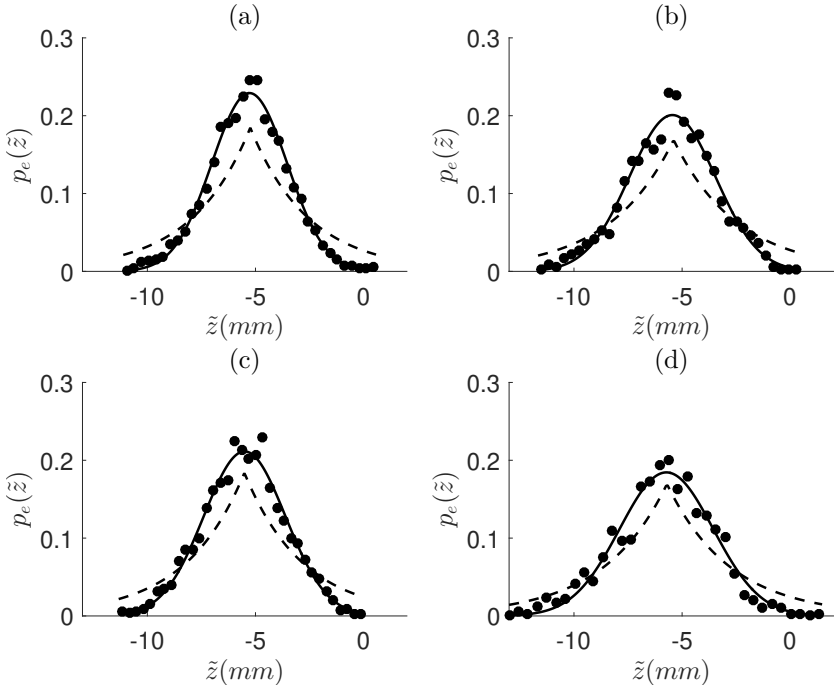

Figure 4.28: A representative of entrainment height distributions for a) F1-Z2d simulations, b) F2-Z2d simulations, c) F3-Z2d simulations, and d) F2-Z2d simulations. Filled circles represent the simulation data; the solid line represents a Gaussian fitting curve, $p_e(\tilde{z}|\tilde{z}_e, s_e^2)$ (Eq. 4.8b), and the dashed line represents an exponential fitting curve, $p_e(\tilde{z}|\tilde{z}_e, s_\eta^2)$, suggested by Wong et al. (2007), (Eq. 4.8a).

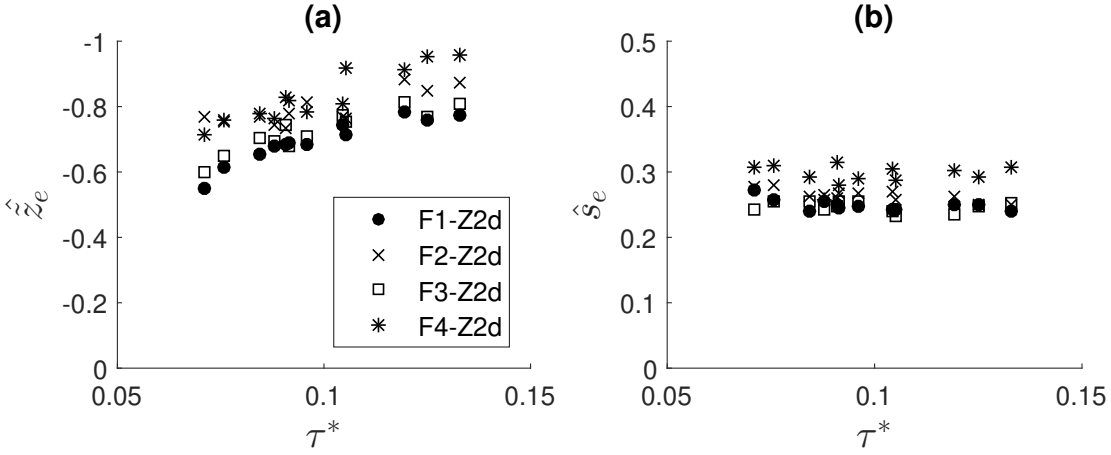

Figure 4.29: Standard deviation of the entrainment height distributions as a function of Shields stress for different fluid models.

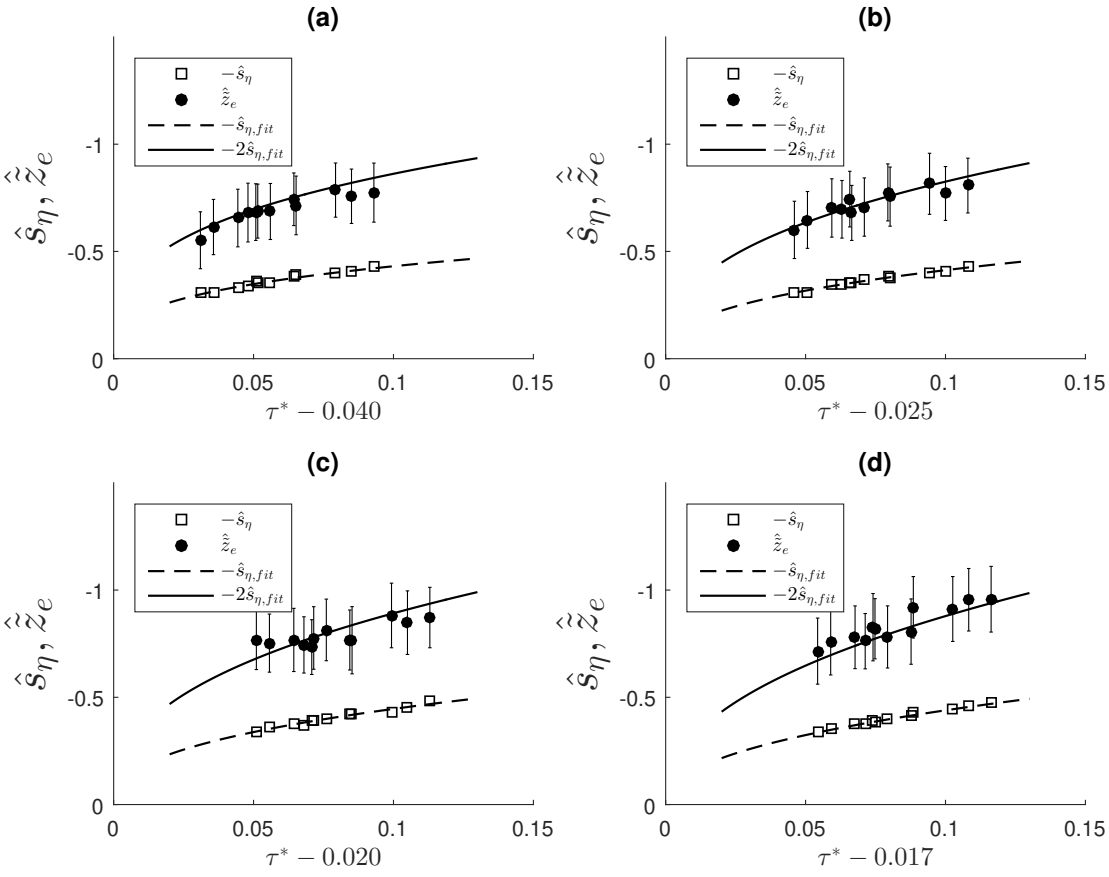

Figure 4.30: Normalized peak entrainment height, $\hat{\tilde{z}}_e$, and normalized bed surface standard deviation, $\hat{s}_\eta$ as a function of excess Shields stress for a) F1-Z2d model, b) F2-Z2d model, c) F3-Z2d model, and d) F4-Z2d model. Error bars show the standard deviation of the entrainment height distribution.

Table 4.9: Summary of statistical analyses of bed surface for 12 different hydraulic conditions with different fluid models .

Run	**Fluid Model**	τ^*	$\hat{s}_\eta$	$\hat{\tilde{z}}_e$
1	(1,2,3,4)	0.1330	(0.43,0.43,0.48,0.47)	(-0.77,-0.81,-0.87,-0.96)
2	(1,2,3,4)	0.1250	(0.41,0.41,0.45,0.46)	(-0.75,-0.77,-0.85,-0.96)
3	(1,2,3,4)	0.1193	(0.40,0.40,0.43,0.45)	(-0.78,-0.82,-0.88,-0.91)
4	(1,2,3,4)	0.1052	(0.39,0.38,0.42,0.43)	(-0.70,-0.76,-0.77,-0.92)
5	(1,2,3,4)	0.1044	(0.38,0.38,0.42,0.42)	(-0.70,-0.78,-0.77,-0.81)
6	(1,2,3,4)	0.0960	(0.35,0.37,0.40,0.40)	(-0.68,-0.71,-0.81,-0.78)
7	(1,2,3,4)	0.0915	(0.35,0.35,0.39,0.38)	(-0.68,-0.68,-0.78,-0.82)
8	(1,2,3,4)	0.0908	(0.36,0.36,0.39,0.39)	(-0.69,-0.74,-0.73,-0.83)
9	(1,2,3,4)	0.0880	(0.35,0.35,0.37,0.38)	(-0.66,-0.70,-0.74,-0.76)
10	(1,2,3,4)	0.0844	(0.33,0.34,0.38,0.38)	(-0.64,-0.70,-0.77,-0.78)
11	(1,2,3,4)	0.0757	(0.31,0.31,0.36,0.35)	(-0.61,-0.65,-0.75,-0.76)
12	(1,2,3,4)	0.0710	(0.30,0.31,0.34,0.34)	(-0.55,-0.60,-0.77,-0.72)

Chapter 5

Discussion of Bedload Simulations

We divide this chapter into three sections. In the first section, we discuss the results presented in the previous section and their implications on providing a better understanding of bedload transport. While mostly beyond the scope of our dissertation, we start by revisiting the similarities and differences in the transport relationships from our data compared to those found from other experiments and simulations. Then we return to the focus of our dissertation to understand how our results provide insights into the inter-relationship between shear stress, bed height variability, and entrainment/deposition heights are interrelated. Specifically, in this section we provide insight about the statistics of the location of the exchange between particles in the bed and particles in transport. In the last section we consider the origin of the different transport magnitudes among our different models for turbulence. In particular, as we discuss, we hypothesize that our results from the simulations using fluid model four overestimate the transport rate. To help with this, we perform additional simulations in which we vary what we might call the "height" of the average velocity profile.

5.1 Review and discussion of transport results

We open up the discussion by first discussing our results on a narrow size particle distribution with $d_{50} = 7.1$ mm (Section. 4.1). We found, despite its simplicity, our DEM model for bedload transport in section 4.1 reproduces transport behaviors measured in physical systems remarkably well, particularly those which Wong et al. (2007) obtained from laboratory experiments with similar parameters. While, the difference between our reference shear stress and and those reported by Wong et al. (2007) or Brownlie (1983) is small, we think our smaller reference shear stress could be due to the different particle shapes as spherical particles can be dislodged more easily from a bed than aspherical angular particles closer to that used in laboratory experiments, for example, by Wong et al. (2007). We propose that these similarities in the context of the relative simplicity of our simulations give strength to a strategy of using them, not only for the statistical analysis we detail in this study, but also for details of the physics behind a variety of these and other transport behaviors. Using such a simple model as the simulation we describe in section 4.1, we can turn on and off a variety of *phenomenology* ranging from turbulent fluctuations in the fluid to asphericity and irregularity in particles shapes and sizes.

While largely beyond the scope of this dissertation, we briefly consider the similarities and differences between our simulation transport results and those from other researchers, beyond those of Wong et al. (2007). As we discuss herein, we hypothesize the difference between simulation and experimental conditions is responsible for the differences in the results and we discuss a few cases to highlight these specific differences.

We first consider simulation results from Schmeeckle and colleagues (Schmeeckle and Nelson (2003); Schmeeckle (2014)). We focus on these as the 2003 work was among the first to integrate a fluid model with discrete element techniques to represent individual particle movement. Further, the fluid part of our DEM model was in large part inspired by the work described in Schmeeckle and Nelson (2003). Yet the results Schmeeckle

Table 5.1: Comparison of different transport model found by several researchers through their experimental studies or computational simulations: $q^* = a_q \times (\tau^* - \tau_c^*)$.

Experiment/simulation	a_q	τ_c^*
This study	2.59	0.051
Luque and Van Beek (1976)	5.7	0.06
Meyer-Peter and Muller (1948); Wong and Parker (2006)	3.97	0.0495
Wong et al. (2007)	2.66	0.0549

and Nelson (2003) obtained generally indicated a larger transport rate for a particular shear stress (i.e., line 2 in Table 5.1) where they used the relationship found by Luque and Van Beek (1976) for 3.3 mm gravel particles to compare with their data. We note that while our fluid model is analogous to that of Schmeeckle and Nelson (2003), our particle model is not. Our model falls under the category of a "soft sphere" DEM model where the time steps in the simulation are sufficiently short that each particle contact is simulated over many time steps allowing for a representative model deformation of the particles. The model of Schmeeckle and Nelson (2003) falls under the category of a "hard sphere" DEM model where each particle contacts is represented with a single time step during which momentum is conserved, and loss of energy is represented relatively simply. These model frameworks can predict significantly different transport rates. While hard sphere models are less computationally expensive, they are typically no longer used for these dense flows because of the importance of enduring contact dynamics in these high solid fraction particulate systems.

Schmeeckle (2014) developed completely new simulations for the second work which represented interparticle contacts using a soft sphere model. In this work, Schmeeckle (2014) compared his model results to those from the predictions of Meyer-Peter and Muller (Meyer-Peter and Muller (1948)) modified by Wong and Parker (2006), (line 3 in Table 5.1) which seemed to compare well. In this case, we note four significant differences with the framework that beg consideration for their potential independent contributions

to transport rate and transport dynamics. (1) The representation of the fluid dynamics includes consideration of large eddies, i.e., it uses large eddy simulation (LES) techniques to capture more spatially and temporally rich dynamics. This is more complex than we use in even our most complicated representation of velocity fluctuations (model 4). (2) The coupling between particle dynamics and fluid dynamics is two-way. That is, the local fluid velocity influences the particle momenta (via drag and other forces like static pressure), and the local particle velocity influences the local fluid momentum. (3) The simulation conditions were somewhat different in a number of respects. The particles in Schmeeckle (2014) simulations are sand-sized, (0.5 mm), significantly smaller than our particles, also primarily at significantly higher shear stresses, under which bedforms were part of the dynamics, and (4) The particle properties were not represented in a completely straightforward way. As is not uncommon, the hardness was reduced by several orders of magnitude which speeds up the simulation processes as it requires fewer time steps per interaction. We believe that more than one of these differences in model details give rise to the differences in model results and deserve further intensive investigation.

Additionally, we consider questions of measured bedload differences under one more category. Specifically, we consider the two models with which Schmeeckle and colleagues (Schmeeckle and Nelson (2003); Schmeeckle (2014)) compare their results based on experimental data and the results from their data are somewhat different than those from ours. These are from Luque and Van Beek (1976) and Meyer-Peter and Muller (1948) that modified by Wong and Parker (2006). One more thing we note involves the value of the critical shear stress as it depends on particle size in our results. As discussed, the small error in our fitting is promising. However, the differences in τ_c^* between our three size particles is considerable. From the modified Brownlie diagram and by calculating the particle Reynolds number, Re_p, for our simulations, we expected to see a smaller differences in τ_c^* among our three sizes particles. To address these issues, we first refer back to a comment made by Wong et al. (2007) in the paper detailing the

experiments and results they obtained in the flume of 7.1 mm particles. They stated, their equation of transport (Line 4 of Table **??**) "is not proposed as a new universal predictor of the volume bed load transport rate of uniform gravel under lower-regime plane-bed equilibrium conditions. Rather, it serves as a baseline relation to analyze tracer displacement." Similarly, we do not view our results for sediment transport in the form of a proposal for a new relationship.

Rather, we view them in the context of a baseline from which we derive other parameters. We were motivated to use the data from the Wong et al. (2007) paper to make sure our results are physically reasonable by using a closely aligned experiment. We note that the experiments on which Luque and Van Beek (1976) and Meyer-Peter and Muller (1948) are based are significantly more varied than ours. In that context we suggest that if we were able to consider a subset of their data that were taken under similar conditions to those of Wong et al. (2007), they would also align closely with our simulation results. While we find these similarities and differences intriguing they fall beyond the scope of the thesis, we are planning further investigation in the near future.

5.2 Review and discussion of bed height and entrainment height statistics

We now turn to the details of the statistical analysis of our bed surface and entrainment height variability obtained in the previous chapter for different hydraulic conditions and particle sizes. Similar to the results of Wong et al. (2007), we found that the bed surface height variability was well-represented by a Gaussian distribution function, regardless of the particle size, the presence or absence of turbulent fluctuations. The normalized standard deviation of the local bed height about the mean, $\hat{s}_\eta$, increased with bed shear stress for all the simulations performed on different size particles and different fluid models. This dependence took the form of a power law dependence on excess Shields stress $(\tau^* - \tau_c^*)$ as did that of the experiments by Wong et al. (2007). As suggested by

Wong et al. (2007), the maximum probability of entrainment height did not coincide with the average bed surface in our simulations. However, we found a unique relation between $\hat{s}_\eta$ and $\tau^* - \tau_c^*$ for all simulations on different size particles and different fluid models, $\hat{s}_\eta = 0.83(\tau^* - \tau_c^*)^{0.29}$ (Fig. 5.1) that is somewhat a weaker dependence than that of Wong et al. (2007) (whose data suggested that $\hat{s}_\eta = 3.09(\tau^* - \tau_c^*)^{0.56}$). This is true both in terms of the multiplier and the power (Fig. 4.9 and the fitted coefficients to Eq. 4.10). In other words, experimental standard deviation of the local bed height increased at a much higher rate than it did in our simulations.

We propose that the differences in the bed-stress-dependence of the bed surface variations found in this study and that reported by Wong et al. (2007) is two-fold. Firstly, particle shape arguably plays a significant role in many transport issues and we propose it plays a role in bed variability as well. Specifically, bed height variability of a bed of spherical particles is due primarily to relative bed surface particle location alone, while in bed comprised of aspherical particles, bed surface variability may be due to both particle height and particle orientation of the topmost particles. The second effect may be associated with differences in measurement techniques. The bed height measurements by Wong et al. (2007) were obtained using measurements of the topmost particle throughout their experiments, which likely includes at least some of the moving particles. This is different than our bed height simulation, in which our bed height measurements are based only on the top surface of the particles in the bed, with some assumptions of how the bed itself is defined. New simulations with aspherical particles can help us investigate the measurement differences and to test our hypotheses about the underlying source(s).

We were somewhat startled to note that our relationship between $\hat{s}_\eta$ and $\tau^* - \tau_c^*$ was independent of particle size and turbulence fluctuation, that it is essentially the same for all conditions in this report. This suggests that the only controlling parameter in shaping the bed surface variations is the extra stress by the flow after the initiation of the particles motion. The turbulence and particles shape affect the reference shear

stress, yet, at the same excess Shields stress, the bed surface variations is similar for all unimodal mixtures when normalized by particle size.

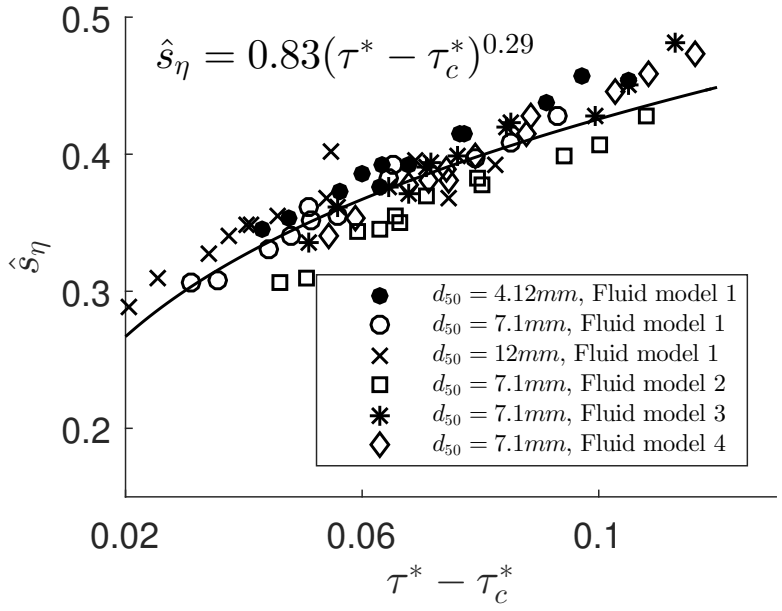

Figure 5.1: The normalized standard deviation of the bed surface variations plotted against the excess Shields stress.

Our entrainment height results provide what we feel is one of the most significant insights from this work regarding the characterization of the bed surface statistics. Before discussing these, we would like to note that these are the first measured results of entrainment height variability, as, because of limited experimental techniques of the period, Wong et al. (2007) could only suggest, not measure, the experimental entrainment height variability. So it is not surprising that some of our results are significantly different from the form expected by Wong et al. (2007).

We highlight four significant results: (i) Our results agreed with those by Wong et al. (2007) in that the maximum probability of entrainment height did not coincide with the average bed surface in our simulations; (ii) In contrast with proposals of Wong et al. (2007), we found that the elevation at which the peak entrainment probability occurs is *above* the average bed height, in contrast of the suggestions by Wong et al.

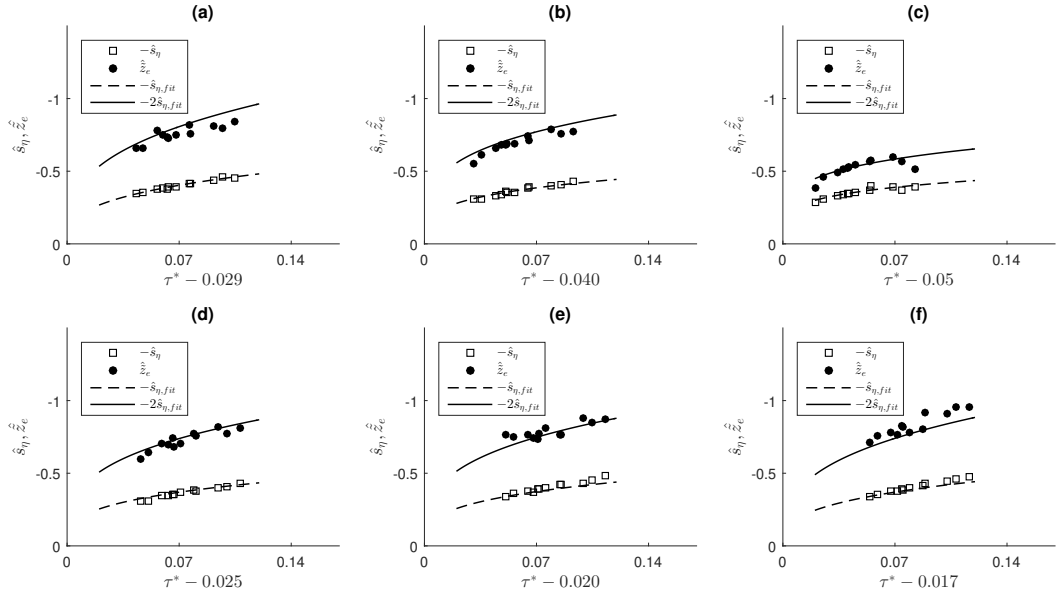

Figure 5.2: The normalized peak entrainment height, $\hat{\tilde{z}}_e$, and normalized bed surface standard deviation, $\hat{s}_\eta$ plotted against the excess Shields stress for a) 4.12 mm particles with fluid model 1, b) 7.1 mm particles with fluid model 1, c) 12 mm particles with fluid model 1, d) 7.1 mm particles with fluid model 2, e) 7.1 mm particles with fluid model 3, f) 7.1 mm particles with fluid model 4.

(2007) that this maximum is likely *below* the average bed surface (in Eq. 2.8b), and (iii) We note that the entrainment height variability was well-represented by a Gaussian distribution function (Fig. 4.7) whose standard deviation ($\hat{s}_e = s_e/d_{50}$) does not vary monotonically with τ_0.

(iv) Perhaps most significantly, the elevation at which the peak entrainment probability occurs ($\tilde{z}_e$) increases with increasing excess Shields stress, similar to the standard deviation of bed variability in Eq. 4.10. In fact, the location of maximum entrainment scales with standard deviation of bed variability $|\tilde{z}_e| \sim \alpha \times s_\eta$ (Fig. 5.2). This result is promising in providing predictions of likely particle entrainment locations by knowing the hydraulic conditions. This makes intuitive sense as, effectively, the location from which particles are being "plucked" increases with the height of maximum protrusion of the bed into the flow. The alternative way to justify this finding is by considering

a bed with a uniform porosity and a flat surface ($s_\eta = 0$). For this bed surface, we expect to have the maximum particle entrainment at the bed surface, or at mean bed height as the most particles are exposed to the highest fluid velocity at that point, We suspect that the details will vary significantly in a bimodal mixture of a different sizes and/or densities in a way that helps explain some of the segregation phenomenology that remains apparently contradictory to established models in mixtures of different density particles (Viparelli et al. (2015)).

For different sized particles where we properly normalized the conditions and the outputs, we note that particle size did not affect the bed surface variations in terms of the standard deviation of bed height Fig. 4.15. On the other hand, we found differences in the normalized s_η values for the different sized particles. This difference is considerable between the $d_{50} = 12.0\ mm$ particles and the other two size distributions. We hypothesize this difference may be associated with the differences in τ_c^* between the different particle sizes. In other words, the standard deviation of the bed surface variations should be a function of the excess Shields stress, $\tau^* - \tau_c^*$, instead of just the Shields stress, τ^*.

Possible reasons for this behavior of the peak entrainment height can be related to the inertia of the large particles, our choice of threshold velocity, or the reference bed shear stress we find from linear least square fitting to our data. This issue is still under investigation. Yet, it is still noteworthy that the peak entrainment height scales with the bed surface roughness and not a constant.

5.3 Distinctions among simulations including velocity fluctuations in bedload transport

5.3.1 Model Validations

As discussed in the previous section, we model the fluid velocities using the "log law of the wall" for the average fluid velocity (Eq. 3.10a), and the proposed expressions for turbulent intensities in the downstream and vertical directions (Eq. 4.13). Since we model the velocity fluctuations as random processes, we found it necessary to check if the fluctuations follow the expressions of interest (Eq. 4.13, 4.20). To do so, we plotted the turbulent intensities from our DEM simulations along with the expression proposed by Nezu and Nakagawa (1993) (Eq. 4.13) in figure 5.3 for a representative ($\tau^* = 0.1044$) of fluid model 2-4.

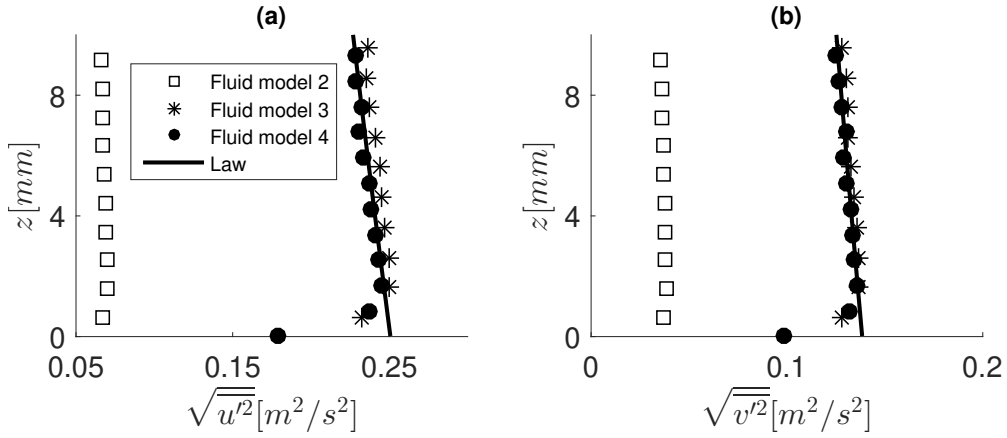

Figure 5.3: Validations of our model turbulent fluctuations against the expressions proposed by Nezu and Nakagawa (1993) for: a) downstream turbulent intensity, (b) vertical turbulent intensity.

Figure 5.3 shows clearly that our fluid models 3 and 4, in which we drew our fluctuations from a normal distribution of numbers, correctly introduced turbulent fluctuations into our simulations in a way that followed the expression proposed by Nezu and Nakagawa (1993) (for the height dependence of average fluctuation magnitudes). However,

our results from fluid model 2, in which we introduced random numbers from a uniform distribution, shows deviation from the expressions of turbulent intensities. We suspect that this might be due to the fact that the turbulent field is a random field characterized by normal distributions based on the Central-Limit-Theorem. In other words, if the flow velocity is measured at a specific time and location in the turbulent flow over many repetitions, then the ensemble average of the measured velocities is a random variable with a normal distributions.

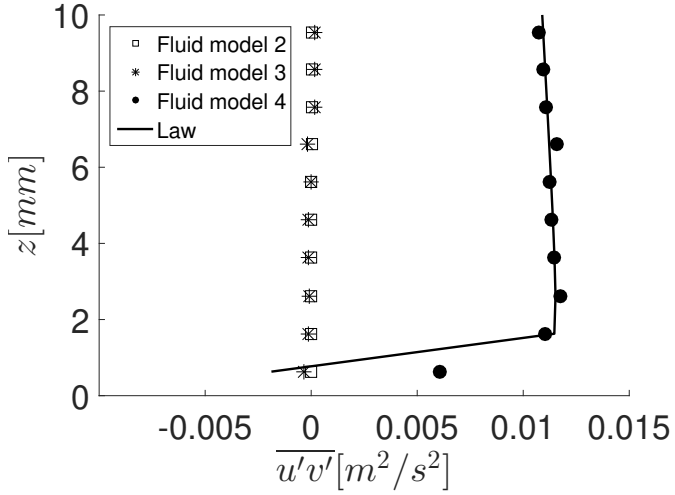

Figure 5.4: Validations of our models capability in introducing the Reynolds stresses similar to what proposed in the literature (Eq. 4.20).

In addition to turbulent intensities, we plot the Reynolds stress for the fluid models 2 to 4 in Fig. 5.4. Figure 5.4 shows that we correctly correlate the fluctuations in downstream and vertical directions for fluid model 4 as the Reynolds stress calculated from the simulations for this fluid model follows the expression of the Reynolds stress (Eq. 4.20). As expected, the turbulent fluctuations in fluid model 2 and 3 are not correlated and therefore the Reynolds stress for these models are approximately zero when averaged over sufficient time.

Figure 5.3 and 5.4 clearly show that our fluid models 3 and 4 satisfy our expectations regarding the turbulent intensities and Reynolds stress. Fluid model 2 shows

deviation from our expectations, however, we included the results from this fluid model for completion.

5.3.2 Importance of baseline depth parameter for velocity fluctuation results

Our simulations using fluid model 3 and 4 provided overestimated transport rate compare to what reported in the literature for 7.1 mm particles and, in particular, to the results of the experimental studies of Wong et al. (2007). Therefore, we perform extra simulations using fluid model 4; however, we shift the zero velocity plane (z_1) upward to reduce the fluid velocity at the bed surface to decrease the particles transport rate which subsequently, results in a decrease in the reference bed shear stress. In particular, we perform three more simulation sets with different z_1 locations (Tab. 5.2).

Table 5.2: Computational flow parameters for investigating the role of zero velocity plane on the transport rate of particles using fluid model 4.

Set Name	Fluid Model	τ^*	k_s	z_1	H (cm)
F4-Z2d	4	0.071 - 0.1330	$3.5d_{50}$	$2.00d_{50}$	10
F4-Z1.9d	4	0.071 - 0.1330	$3.5d_{50}$	$1.90d_{50}$	10
F4-Z1.8d	4	0.071 - 0.1330	$3.5d_{50}$	$1.80d_{50}$	10
F4-Z1.75d	4	0.071 - 0.1330	$3.5d_{50}$	$1.75d_{50}$	10

In a similar procedure we followed to present the results in the previous chapter, we first calculated the normalized transport rate, q^*, of these new simulations. Fig. 5.5 shows the transport rate of two representatives ($\tau^* = 0.0915, 0.125$, similar to the representatives in Fig. 5.5) over time. As clear in Fig. 5.5, shifting the z_1 values upward results in a decrease in the transport rate of particles.

We perform a similar linearized least square fit to these new simulations (F4-1.9d, F4-1.8d, and F4-1.75d) as we did for the other simulations in the previous chapter to find the parameters of the transport rate model (See Fig. 5.6 and Tab. 5.3). Our

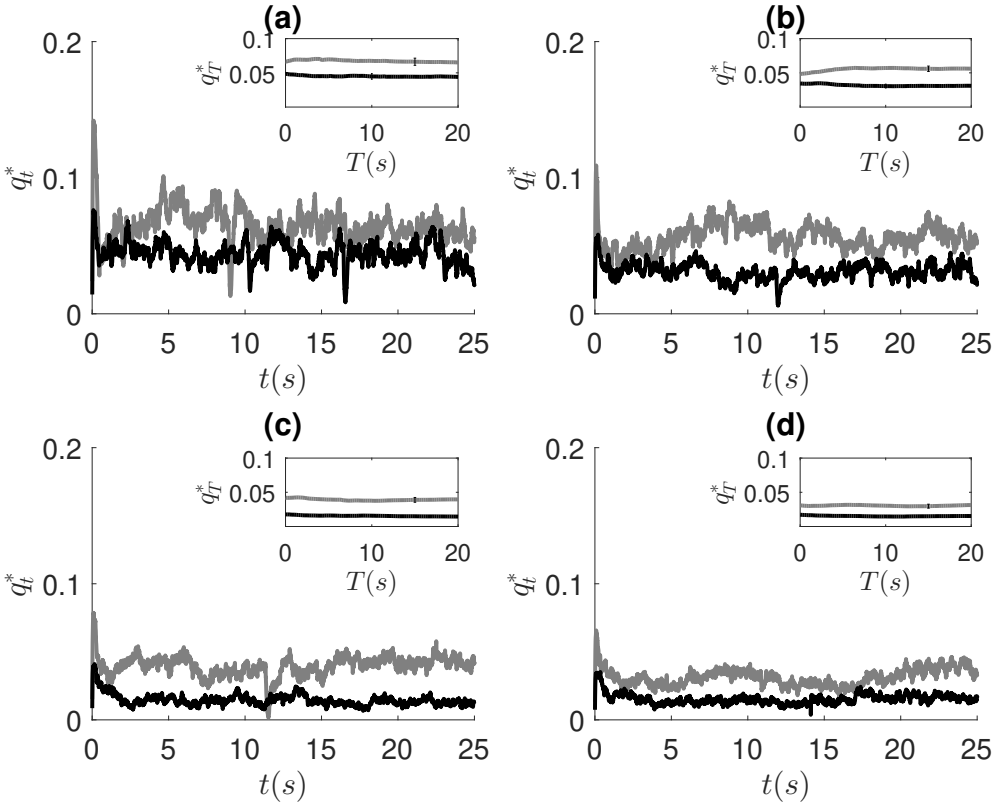

Figure 5.5: Time series of transport rate of two representative simulations for a) F4-Z2d model, b) F4-Z1.9d model, c) F4-Z1.8d model, and d) F4-Z1.75d model. The bed shear stress for black line is $\tau^* = 0.0915$ and for gray line is $\tau^* = 0.125$. The inset in each plot shows the average transport rate starting just after reaching the steady state to time T after reaching steady state. The error-bar in the inset shows the standard deviation of transport variations for 20 seconds after reaching the steady state conditions.

results show a similar transport rate between F1-Z2d and F4-Z1.8d models, where in the first case we have no turbulent fluctuations and in the latter one, we have turbulent fluctuations but the zero velocity plane is closer to the average bed surface.

Table 5.3 shows the reference bed shear stress is the same for F4-Z1.75d and F4-Z1.8d models, however, the coefficient a_q is different. The coefficient a_q shows the sensitivity of transport rate on changing the bed shear stress. In other words, a higher a_q results in a higher rate of increase in transport rate associated with increases in bed shear stress. We note this is apparent in the measurements shown in Fig. 5.6 in which the transport

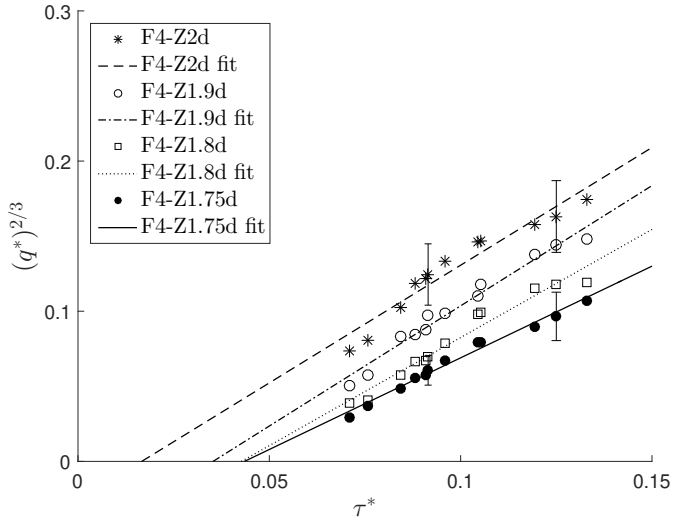

Figure 5.6: Linear least square fitting to transport data against the dimensionless bed shear stress, τ^*, to find the parameters of our transport model, $q^* = a_q \times (\tau^* - \tau_c^*)^{1.5}$, for fluid model 4 but with different z_1 values.

rates of F4-Z1.8d and F4-Z1.75d are close to each other at small bed shear stresses and deviate from each other at higher bed shear stresses.

Table 5.3: Transport parameters for different zero velocity planes of fluid model 4.

Set Name	**Fluid Model**	z_1	a_q	τ_c^*
F4-Z2d	4	$2d_{50}$	1.96	0.017
F4-Z1.9d	4	$1.9d_{50}$	2.03	0.035
F4-Z1.8d	4	$1.8d_{50}$	1.73	0.043
F4-1.75d	4	$1.75d_{50}$	1.35	0.043

To investigate the role of the location of zero velocity plane on the bed surface variations, we calculate the bed surface distribution of these new simulations using the procedure detailed in the previous chapter and plot a representative of each case on Fig. 5.7.

Fig. 5.7 shows the location of the zero velocity plane, z_1, also affects the bed surface variabilities (i.e. compare the distribution of plot (a) which is for F4-Z2d and plot (d)

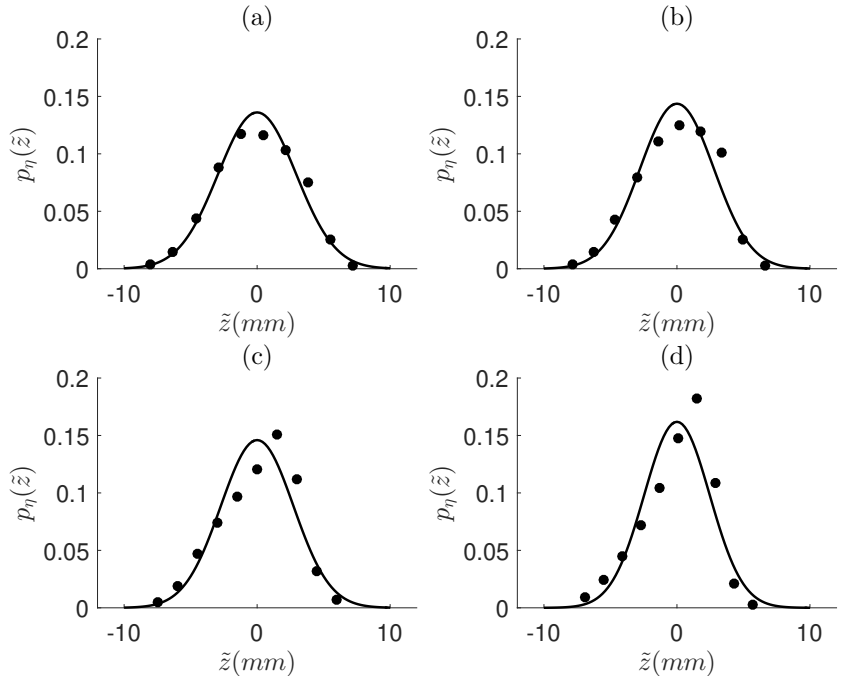

Figure 5.7: A representative ($\tau^* = 0.1044$) of probability density distribution of bed height variations for each fluid model: (a) F4-Z2d, (b) F4-Z1.9d, (c) F4-Z1.8d, and (d) F4-Z1.75d. Filled circles represent the simulation data while the solid line represents the Gaussian fitting curve, $p_\eta(\tilde{z}|0, s_\eta^2)$.

which is for F4-Z1.75d). These results indicate the distribution is wider for a lower zero-velocity depth. To investigate this further, we calculate the normalized standard deviation of the bed surface variations of these simulations and plot on Fig. 5.8 versus both Shields stress and excess Shields stress.

Fig. 5.8a shows a systematic variations in the magnitude of $\hat{s}_\eta$ values with the location of zero velocity plane, when plotted as a function of Shields stress. As clear in this figure, shifting the zero velocity plane upward, which results in a decrease in the average flow velocity at the bed surface, results in a decrease in the bed surface standard deviation.

We plot the $\hat{s}_\eta$ of these simulations against the excess Shields stress on Fig. 5.8b. We found a similar power law relation for these new simulations with the same coefficients

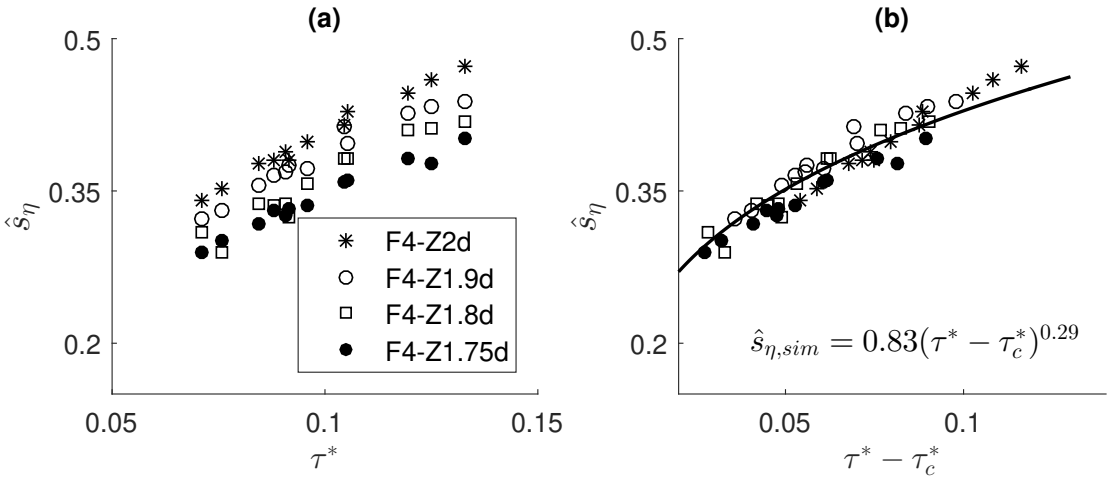

Figure 5.8: Standard deviation of bed surface variations for fluid model 4 , where turbulent fluctuations are introduced from a bi-variate Gaussian distribution, but with different zero-velocity plane locations, a) against the Shields stress, b) against the excess Shields stress.

as to what found before for other simulations.

Next, as we did for our results in the previous chapter, we calculate the entrainment height distribution of these new simulations and plot a representative from each in Fig. 5.9. This figure shows that the location of the zero velocity plane or the average flow velocity also affects the standard deviation of the entrainment height distribution. This is particularly true for the initial shift from 2d to 1.9d (Fig. 5.9(a) to (b)). However, the sensitivity decreases as the zero velocity plane shifts upward (Fig. 5.9(c) to (d)). We note that this accentuates the relationship we mentioned in the previous chapter between the presence of turbulent-like fluctuations and a widening of the $p_e(z)$ distributions.

One of our significant finding in the previous chapter was the relation between the peak entrainment height and the the surface standard deviation ($|\tilde{z}_e| \sim \alpha \times s_\eta$). To understand if this relation applies to these new simulations, we calculate the peak entrainment height of these new simulations and plot them along with the bed surface standard deviation on Fig. 5.10. This figure shows the peak entrainment height, still, scales with the bed surface standard deviation.

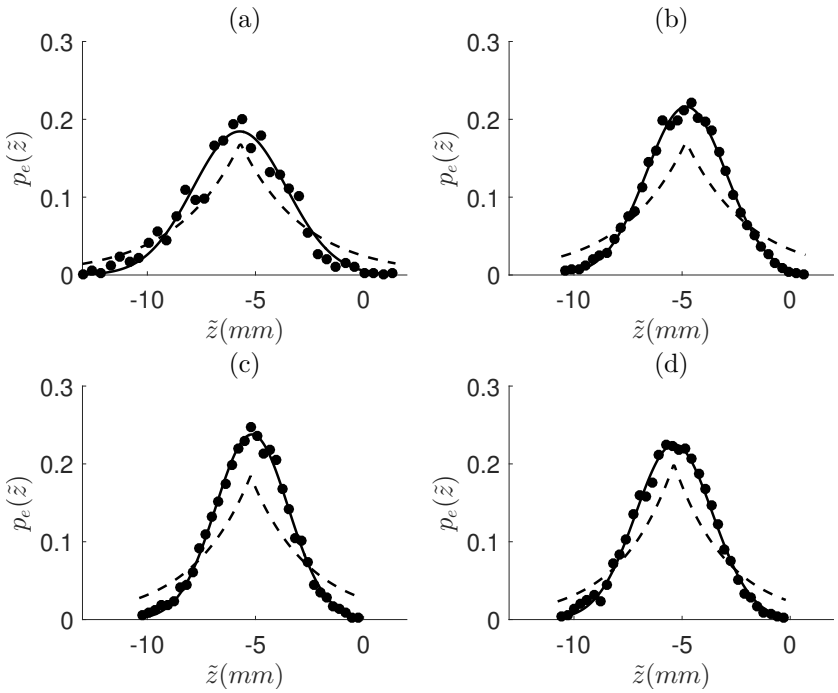

Figure 5.9: A representative ($\tau^* = 0.1044$) of entrainment height distributions for a) F4-Z2d simulations, b) F4-Z1.9d simulations, c) F4-Z1.8d simulations, and d) F4-Z1.75d simulations. Filled circles represent the simulation data; the solid line represents a Gaussian fitting curve, $p_e(\tilde{z}|\tilde{z}_e, s_e^2)$ (Eq. 4.8b), and the dashed line represents an exponential fitting curve, $p_e(\tilde{z}|\tilde{z}_e, s_\eta^2)$, suggested by Wong et al. (2007), (Eq. 4.8a).

The results of this section support the main findings of the previous chapter. However, the significance of these new simulations is to provide results with the same reference shear stress that would help us to better compare the role of turbulent fluctuations with the average flow velocity on the exchange of the bed with the bedload.

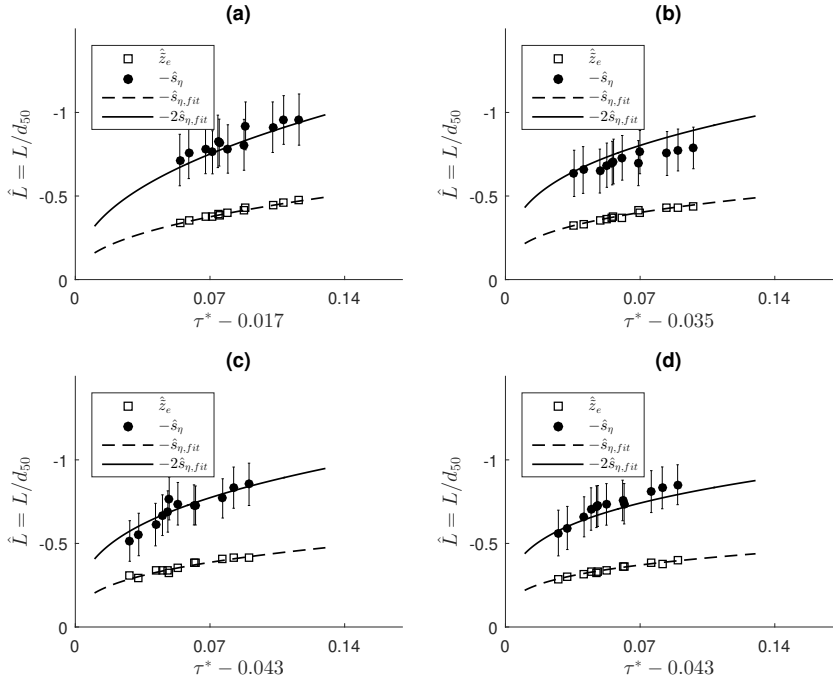

Figure 5.10: Normalized peak entrainment height, $\hat{\tilde{z}}_e$, and normalized bed surface standard deviation, $\hat{s}_\eta$ as a function of excess Shields stress for a) F4-Z2d model, b) F4-Z1.9d model, c) F4-Z1.8d model, and d) F4-Z1.75d model. Error bars show the standard deviation of the entrainment height distribution.

Chapter 6

Background on studies of erosion rates by debris flows

The second class of eroding flows we examine in this thesis involves *debris flows*. Debris flows in the context of geomorphological flows are massive movers of sediment – boulders, gravel, and sand- and clay-sized particles – from mountainous regions and steep hillslopes to foothills, valleys, and river channels below (Jakob et al. (2005)). Along the way, they pose significant hazards to infrastructure and human life, and they determine important details of river channel dynamics to which they supply a substantial amount of sediment. There is significant evidence that changing land use and climate change are increasing debris flow magnitude and frequency which accelerate the need to understand their dynamics (e.g., Stoffel and Beniston (2006); Jakob and Friele (2010); Jomelli et al. (2009)).

Much of our understanding of debris-flow processes is drawn from experimental studies (i.e. Papa et al. (2004); Egashira et al. (2001); Iverson et al. (2011); Farin et al. (2014); Mangeney et al. (2010); Papa et al. (2004)) and limited natural examples (i.e. Berti et al. (2000); Berger et al. (2011); McCoy et al. (2012)). The significant hazard of bouldery debris flows limits the active measurement of erosion rates by natural debris

flows. Additionally, the wide range of grain size along with the limited understanding of the possibly unique contribution of the different sized particles to the dynamics of the debris flows has limited confidence in experimental measurements (Iverson (1997, 2003)). Notably, with recent advancement in computational powers, simulations of debris flows are being considered to provide more information at particle-scale (Zhao (2014)). However, these simulations are still limited due to the difficulties in simulating of a large number of particles with current computational power.

Thus much of our community understanding of erosion by debris flows has been developed in the context of continuum-like sediment transport models, such as ideas of an "excess shear stress" suggested by Takahashi (2009). In turn, predictions from these model frameworks have been fit by the relatively limited available data, such as, in the Takahashi (2009) framework, a minimum angle before sufficient stress forces entrainment. It is already evident that the success of the results are situation-dependent. It is likely that changing environmental conditions, such as rainfall frequency and magnitude, and variable particle properties limit effectiveness of empirical models based primarily on field debris flows.

A solution to this problem may lie in a more physics-based understanding of the manner in which debris flow composition, interstitial fluid composition, and particles which can vary from one debris flow to the next can affect debris flow behaviors. Understanding the mechanisms that control the rate at which a particular debris flow entrains particles and grows in size is important for predicting their hazard (Godt and Coe (2007)).

In this Chapter of this dissertation, we review some of the studies performed to provide an understanding of the parameters that control the entrainment rate of debris flows. Then, we describe new experimental work whose methodology and results provide a foundation to better understand effects of variable particle size distributions in a debris flow on its erosion of loose bed materials.

6.1 Field-scale observations of debris flow entrainment

Much of our intuition of debris flow entrainment has historically been obtained from observations of landscape evolution associated with natural debris flows. After a debris flow is initiated, inspection of the steepest part of the canyons indicates that at the steepest slopes, debris flows entrain most loose sediment in their paths and incise into the bedrock itself (e.g. Wieczorek et al. (2000); Stock and Dietrich (2006);). At intermediate slopes debris flows no longer scour down to bedrock, but they typically continue to entrain debris from the channel bed causing granular flows increase considerably in size (e.g., Revellino et al. (2004); Hungr et al. (2001)).

This study concerns with the dynamics of the entrainment process when the flow is not supply limited. Rather, the rate of entrainment is governed by the flow and/or material in the bed. Many physical factors influence debris flow entrainment rates under these conditions. In most cases, these have been categorized into one of two mechanisms: (1) an applied shear stress by the flow on the bed that has the potential to accelerate the material into motion and (2) internal forces or stresses within the bed that resist the movement of bed materials into the flow (e.g., Takahashi (2009); Hungr et al. (2001)). In other words, the rapid loading associated with debris flows can entrain particles by increasing the shear loading of the material at the same time it can reduce the internal stress or even induce a liquefaction of the bed material, leading to erosion.

Monitoring stations around the world have produced data that have increased our understanding of key factors in debris flow entrainment. Notably, these include stations in active debris flow sites such as Acquabona Creek in the Dolomites in the Italian Eastern Alps (Berti et al. (2000)); Illgraben channel in the Swiss Alps (Berger et al. (2011)); Chalk Cliffs study basin in the Sawatch Range, Colorado, USA (McCoy et al. (2012)). Berti et al. (2000) used flow height sensors, load cells, and fluid pore pressure sensors buried in the channel bed to understand entrainment dynamics in the Italian Eastern

Alps. Their data indicated that the scour rate was proportional to local slope gradient. Berger et al. (2011) used a progressive erodible daisy-chained sensor in conjunction with dynamic load cells measuring downslope and normal stresses, pore pressure sensors video monitors in moderately moist debris flows along the Illgraben channel in a temperate-humid region in the Swiss Alps. They found that entrainment rate increases with both average and fluctuating stresses, and demonstrated that the fluctuations and entrainment rate particularly well-correlated with the highly fluctuating granular front. McCoy et al. (2012) used a comparable situ sensor network to measure related quantities in the Chalk Cliffs study basin of Colorado for dry-to-saturated flows in the typically semi-arid conditions. They found a strong correlation between entrainment and bed-sediment moisture content by comparing time-averaged entrainment rates across all six (dry and saturated) flows. In contrast to the findings of Berger et al. (2011), McCoy et al. (2012) found negligible correlations between stress fluctuations and sediment entrainment, perhaps because of a different in the nature of the debris flows. The Chalk Cliffs measurements indicated shallow stress fluctuation penetration depths into the bed. These field studies have demonstrated the importance of bed inclination, moisture level, and dynamics such as shear stress and bed fluctuations. However, investigating the effects of grain size distribution of the debris flow, or of the erodible material, on erosion dynamics is difficult due to the difficulty of systematically isolating the effect of grain sizes, interstitial fluid properties and other factors from one another.

6.2 Laboratory scale experiments of erosion dynamics

Laboratory investigations can isolate the effects of particle properties, changing interstitial fluid properties, slopes and other parameters from one another. Egashira et al. (2001), Papa et al. (2004), and Haas and Woerkom (2016) reported experiments in a laboratory flume designed to study the effect of changing relative size of the particles in

the flow and the bed. Egashira et al. (2001); Papa et al. (2004) both used millimeter-sized particles (from $\sim$ 2 mm to 10 mm) in an experimental flume with an adjustable angle. The flume was designed with a "weir" at the bottom, allowing these researchers to fill the bottom of the downstream end of the flume with particles and provide an erodible bed at a lower angle of inclination. Papa et al. (2004) showed that, for these systems, if both bed and flow particles are of the same size distribution, erosion rates decrease monotonically with increasing particle size. Egashira et al. (2001) demonstrated that, using smaller or equal-sized particles in the flow, the net erosion rate increases with decreasing bed particle size. Egashira et al. (2001); Papa et al. (2004) predicted theoretically that net erosion rate should scale as d_{flow}/d_{bed}, i.e,. the smaller the bed particles relative to the particles in the flow, the larger the erosion rates.

More recently a significant body of experimental erosion rate research has been performed in the University of Minnesota Complex Particle Flows Laboratory that forms the foundation of the work described in this chapter. Briefly, the work covers four topical areas: (1) laboratory flume design, (2) particle tracking studies of debris flows of narrow grain size distributions, (3) particle scale analysis of bed aging phenomenology for debris flows of narrow grain size distributions, and (4) Effect of viscosity.

Maki (2018) performed several experimental tests to study the dependence of debris flows erosion on the channel slope and particle size distributions. To do so, she performed experiments on dry mixtures, to remove any effects due to interstitial fluid, in a built-in flume designed by Hill et al. (2013). However, the unique features of their flume (same flume is used in this study) allows the investigation of the effect of inclination angle, interstitial fluid, the pore fluid pressure and particle size distributions on the debris flow erosion rate under a controlled procedure. Similar to the bedload transport that researchers developed expressions relating the transport rate to the excess Shields stress, Maki (2018) suggested that the net erosion of materials depends on the difference between the bed inclination angle and the neutral angle, the angle where the net erosion is zero.

The experimental work of Maki (2018) investigated the dependence of net erosion on the particle size distributions with minimum investigation of these dynamics at particle-size scale. To build on this, Moberly (2015) performed experiments on unimodal dry mixtures with a high speed camera to capture flow dynamics at 1000 frames per seconds. To measure the dynamics at particles scale and to relate these with the erosion behavior of the flow, Moberly (2015) developed an algorithm to analyze the images captured by high speed camera through three steps: (1) locating and tracking particles; (2) calculating the solid fraction and velocities profiles; and (3) use the information calculated in step 2 to determine the erosion, erosion rate and the forces that may be driving forces of the entrainment. These three steps are the foundation of image analyses performed in this study. The results of Moberly (2015) showed a positive relation between the erosion rate and granular temperature but no dependence was found between the erosion rate and shear stress.

Longjas et al. (2016) studied the structures within the bed that may resist or help the erosion rate by the debris flows. Their results showed that repeated flows on a bed, weaken the underlying structures within the bed; Therefore results in an increase in the erosion rate of materials by the flow.

Mullenbach (2018) performed experimental studies on the same flume used by Maki (2018); Moberly (2015), to understand the role of the interstitial fluid on erosion rate behavior of debris flows. To systematically investigate the role of the interstitial fluid on erosion rate, he used a viscous Newtonian fluid. He varied the viscosity of the interstitial fluid from one experiment to the next ($\mu = 1$ to 62 centipose). His results showed that the presence of the interstitial fluid, in general, lower the neutral angle; however, he found no changes in the neutral angle by changing the viscosity of the interstitial fluid. His results showed a correlation between the erosion rate with excess pore fluid pressure. Pore fluid pressure is defined as the pressure of fluid that filled the pores and is usually represented by the hydrostatic pressure ($P = \rho_f ghcos(\theta)$). Excess pore fluid pressure refers to times when the pore pressure exceeds that due to the weight of the fluid.

Mullenbach (2018) concluded that the additional erosion he measured under cases of excess pore pressure is dud to a decrease in the normal stresses borne by the particles that reduces the resistance of the bed to erosion Iverson et al. (2010).

While laboratory bench-scale results are compelling, we recognize here that typical laboratory experiments such as these suffer the risk of scale-limiting issues, particularly when it comes to particle-fluid flows [e.g., Iverson (1997)]. The well-known United States Geological Survey (USGS) flume [Iverson et al. (2010)] provides some best elements of both worlds – those of laboratory experiments and field measurements. At 95 m long and 2 m wide, it is sufficiently big to minimize scaling issues of smaller laboratory experiments. Yet because of its relatively simple (rectangular) channel geometry and detailed instrumentation, it provides a setting that allows for systematic studies primarily only possible in relatively small laboratory flumes. Using these facilities, researchers have been able to isolate a number of important dynamics of debris flows [e.g., Iverson et al. (2010)]. Notably, Iverson et al. (2011) and Reid et al. (2011) tested the effect of changing volumetric water content of the bed on relative erosion of that bed by a debris flow. To do so, they varied water content from $\sim 15\%$ to 30% holding all else constant, including the particles in the bed and flow, i.e., mostly gravel and sand with a small percentage of finer particles. They demonstrated that bed moisture plays an indisputable role in entrainment: the more moisture in the bed, the higher the measured entrainments rates. Further, they showed that higher entrainment rates associated with the higher bed moistures were strongly correlated with higher mobility rates of the debris flows.

With this brief review of historical attempts to understand the dynamic of debris flows, and especially the entrainment rate of materials, , we note that the affect of grain size distribution on erosion rate still remains largely unknown. Thus, in this dissertation, we address work to understand the influence of grain size dependence of an initial debris flow on its erosion of materials in the bed over which it flows. To help provide a foundation for these studies, we focus on bimodal mixtures in the initial

debris flow and use dry particles for the results described here. In the next Chapter, we present the methodology we use to investigate the entrainment rate of debris flows as it depends on certain aspects of the grain size distribution in bimodal mixtures.

Chapter 7

Experimental debris flow design and analysis methodology

The experiments described herein were performed in our laboratory flume (Fig. 7.1) designed by Hill et al. (2013); Maki (2018) and fabricated by the University of Minnesota College of Science and Engineering (CSE) machine shop, specifically to study erosion and deposition by an experimental channelized debris flows. Previous students have described the functionality and details of the flume over the last decade (Maki (2018); Moberly (2015); Mullenbach (2018)) to which a number of modifications have been made over the years. For completion and for an up-to-date picture of the experimental conditions under which we performed this work, we also provide a detailed description in this chapter.

7.1 Experimental details

7.1.1 Experimental flume, materials, and equipment

The channel of the flume is approximately 3 m long $\times$ 0.08 m wide. The inclination angle of the flume (ϕ) is adjustable from approximately 0° to 40°. The upslope $\sim$ 1.8

m of the flume channel has a rigid rough bed and is approximately 1.8 m long × 0.15 m deep × 0.08 m wide. Three release gates are installed along this section of the flume at 0.38 m, 1.12 m, and 1.84 m from the upstream end. The bed is roughened from 1.12 mm to the end of this upslope region using sandpaper of ∼ 1mm roughness elements. For the experiments we report here, we used the central release gate at 1.12 m from the upstream end. (Similar results were found using release gates at 0.38 m from the upstream end as detailed in (Moberly (2015)). The downslope ∼ 1.3 m of the flume has a false bottom, without which is ∼ 1.3 m long ∼ 0.70 m tall × 0.15 m high. Both ends of the erodible bed chamber are bounded by a wire mesh of spacing ∼ 0.5 mm up to the height of the bottom of the rigid bed (0.15 m high). A ramp installed between the bottom of the rigid bed and the bottom of the erodible bed chamber (inclined ∼ 30° from the bed) minimizes the scour that, prior to its installation, occurred at the upstream end of the erodible bed. Since installation, the scour is almost non-existent, and did not appear to affect the results we present here.

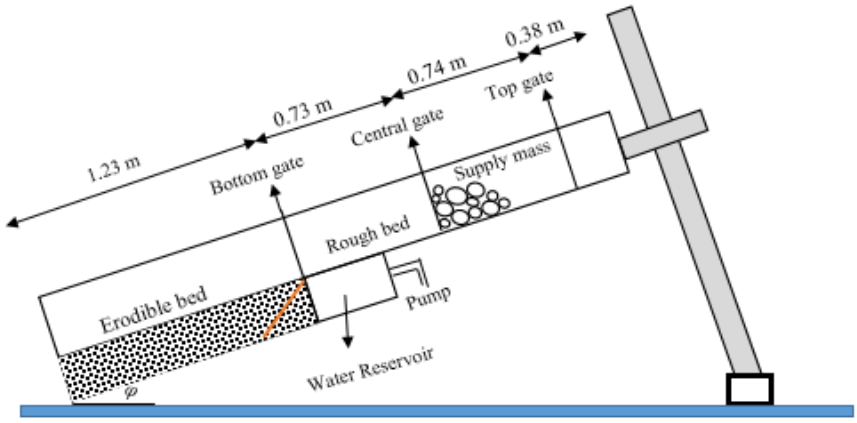

Figure 7.1: Sketch of laboratory flume (not to scale).

For our experimental debris flows and bed material over which they flowed, we used unimodal and bimodal systems of near-spherical zirconium silicate beads (density of 4100 kg/m^3 and diameters of 2.0 mm and 0.8 mm). We dyed the smaller particles blue

using Sharpie ink to enhance differentiation of the two constituents when used together in an experiment. To simplify the experiments for this work, we used only one type of bead in the bed at the beginning of each experiment and used uniform or bimodal systems in the supply, or initial debris flow, of the same material as the particles in the bed.

For each experiment, we used three primary pieces of measurement equipment: a digital level (Husky® accurate to the nearest 0.1°), a digital scale (with a resolution of one gram), and a high speed camera (Photron Fastcam SA3, capable of 1000 x 1000 resolution at 1000 framese per second). Before and after each experiment, we made two relatively simple measurements of relevance here: (1) We determined the inclination angle of the flume, ϕ, using a digital level placed on the base of the flume, as we inclined the flume. (2) We collected mass measurements of the particles using a digital scale. In addition, we captured high speed videos of the experiments using a high speed camera. We present the algorithm used to analyze the images captured by these cameras in the next section.

7.1.2 Experimental procedure

To prepare each experiment, we reset the bed with the flume in a horizontal position, such that $\phi \approx 0°$ and apply anti-static spray to the flume walls. We place a predetermined mass and mixture of particles in a position upslope of the closed gate to act as the initial debris flow for our experiment. The shape of the conglomerate of particles placed here is similar from one experiment to the next, though, using this release gate, we observe little-to-no difference in net erosion when this was changed (Moberly (2015)). Next, we place an amount of particles in the erodible bed chamber predetermined to fill the chamber to the top. We use a flat rectangular plastic piece to *scree* the bed, that is, to gently smooth the top of the erodible bed in a way that flattens the surface while minimizing disturbance to the bed beyond the top layer of beads. After this, we incline the flume to a predetermined angle and then secure the flume in place.

To initiate each experiment, we open the gate to allow the initial debris flow material to flow downstream. As the initial debris flow travels over the roughened rigid section of the flume, the particles accelerate, become agitated and spread out due to the interparticle interactions. Once the energized particles reach the stationary erodible bed, they collide with and mobilize initially stationary particles. These mobilized particles, once energized, become part of the energized shearing collisional flow and subsequently mobilize lower, initially stationary particle in the bed. An apparent non-material boundary between moving and stationary particles descends for some time, depending on the experimental conditions. Then, the process reverses. The bottom-most moving particles slow and stop due to "drag" forces from the particles below them and insufficient mobilizing interactions from the particles above. Next, the particles slightly higher in the bed slow to a stop and so on, until the non-material boundary between moving and stationary particles comes to a rest at the top of the bed. Over the duration of an experiment, the bed may increase in height and mass, decrease in height and mass, or return to its original value, depending on the conditions. That is, at the end of each particular experiment: (1) all or some of the initial debris flow may have deposited on the bed, more so than is eroded, so it finishes with an increased height; (2) some of the bed material may have left the flume, more so than is left behind by the original debris flow, so it finishes with a lower height, or (3) the initial debris flow material that never leaves the flume may be exactly balanced by the bed material that is eroded and leaves the flume, so that the bed finishes with the same height at which it started

During each experiment, we monitor the flow, entrainment, and deposition dynamics primarily using one high speed camera. After flow ceases, we weigh the particle that exited the flume during the experiment to calculate a net mass eroded from the bed, and we analyze the digital images to measure the local quasi-instantaneous entrainment rate.

7.2 Image Processing and Analyses

To monitor the dynamics of debris flows and in particular, the erosion rate and its driving forces, we need to precisely locate and track the movements of particles over the course of the experiments. We found algorithms used previously (Moberly (2015); Mullenbach (2018)) did not provide sufficient particle location for the different sized and shaded particles necessary for the mixtures tracked for this thesis. To improve the tracking, we developed an improved algorithm to detect the particles and track their motion from one image to another.

7.2.1 Particle Locating and Tracking

To locate the particles, we first improve the image quality for the ease of particle locating. To do so, we apply a high-pass and low-pass filtering on each frame captured by the high-speed camera. We perform high-pass filtering with a Gaussian filter to sharpen the image which increase the contrast between the bright and dark pixels. This helps differentiate the particles from each other and also from the image background. We also apply a low-pass filtering with a box blur filter to suppress the noise at small scales.

We perform these filtering steps by performing a convolution of the original image with mathematical representations of these filters. To demonstrate how this type of the convolution works, we consider the 3×3 matrix in Fig. 7.2, an arbitrarily chosen *sharpening* matrix (or *kernel*). We use similar sharpening kernels to emphasize the differences between adjacent pixels. As an example, of how this works, we consider it in the context of a sample (small) 10 by 10 pixel image, where the greyscale is represented by a number proportional to its brightness (see Fig. 7.3). We perform the convolution by operating on each entry of the matrix except the border entries in Fig. 7.3). We do so by first conceptually overlying the convolution kernel on the image matrix with its center on a particular pixel and the rest of the convolution kernel entries on the surrounding image pixels. Then we multiply each entry of the convolution kernel with

the image pixel over which it lies. Finally, we sum these products and replace the central image pixel of this operation with that sum of the products. We perform this operation on each entry of the original matrix and replace it with the modified entries for all but the edge pixels. For a particular example, we consider applying the sharpening kernel on the highlighted pixel in Fig. 7.3:

0	-1	0
-1	5	-1
0	-1	0

Figure 7.2: An example of sharpen kernel with the size of 3×3 to filter the images captured by the camera.

$$\begin{aligned}((0)(34) + (-1)(43) + (0)(49) + (-1)(39) + (5)(46) \\ +(-1)(46) + (0)(39) + (-1)(46) + (0)(46)) = 56\end{aligned} \tag{7.1}$$

Fig. 7.2 shows a convolution kernel with a size of 3. For the purpose of the image processing for this study, we choose the size of our high-pass and low-pass kernels to be the same as the size of the particles in pixels. For the bimodal cases, we use the size of small particles to set the size of the convolution kernels.

After filtering the images, we use the filtered images to locate the particles. Moberly (2015); Mullenbach (2018) used the local brightness maxima algorithm to estimate the center of each particles. In particular, the algorithm they use first identifies the pixels that are brighter than their adjacent neighbors and sets the other pixels to zero. Then, on a domain that correspond to the size a particle, it picks up the brightest pixel among the selected bright pixels and estimates it as the center of the particle. Finally, using the

34	43	49	43	38	33	25	17	12	9
39	46	46	48	48	41	36	30	20	9
39	46	46	50	51	49	45	35	23	11
46	53	57	61	60	56	51	43	33	19
52	51	62	64	64	58	54	47	38	28
50	56	61	67	71	63	55	48	41	32
50	55	62	63	65	61	51	46	41	32
53	57	57	61	61	58	51	44	36	29
48	54	57	60	58	56	49	44	38	26
44	49	55	60	57	55	50	40	41	24

Figure 7.3: An Image with arbitrary pixel points to understand the convolution matrix on an image.

estimated locations, their algorithm calculates a more precise location of the particles' center by calculating the weighted average brightness of the pixels around the estimated location. These calculations are similar to the calculations of mass centroid except that instead of mass, the brightness of the pixels are used.

While the procedure above works well in identifying the particles in a unimodal system, its capabilities is limited in bimodal mixtures. The problem arises from choosing an appropriate size of domain. Setting the size of domain to the size of coarse particles (2 mm particles) leads to neglecting some of the fine particles (0.8 mm particles) in the image. Yet, setting the size of domain to the size of fine particles leads to detecting multiple bright spots on coarse particles. While we could pick these out by eye and distinguish them one at a time, we would not be able to perform much analysis because of the intensive time we would need to do so.

To resolve this problem, we combined the local brightness maxima algorithm with a built-in function in MATLAB called "*imfindcricles*". This function uses the Circular Hough Transform (CHT) algorithm to find circular objects in an image. To do so, this algorithm, first, detects the pixels with highest brightness gradients. The algorithm treats these pixels as representatives of the circular object perimeter. Then, each of

these detected pixels are assumed to be a center of a circle with a known radius of R. The algorithm finds the center of the true circle by finding the point or pixel that is shared with most the of other circles. Figure 7.4 shows schematic representation of this process.

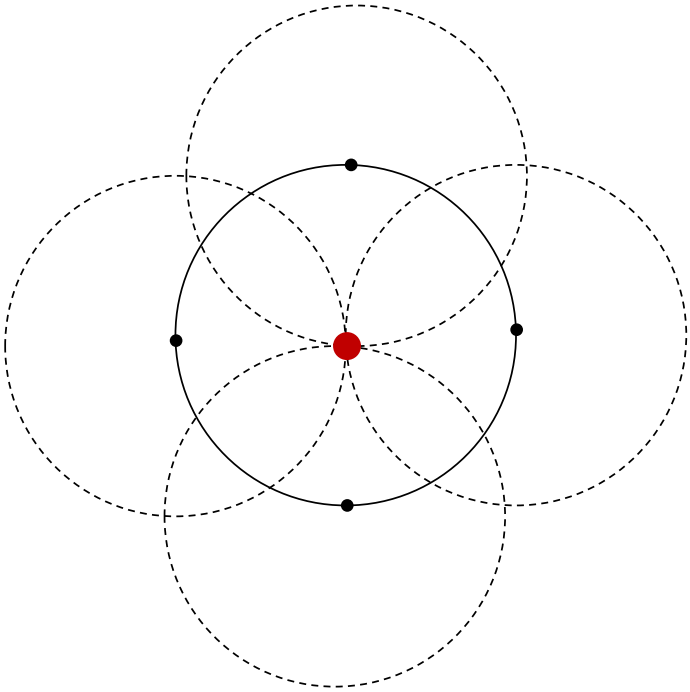

Figure 7.4: Schematic illustration of how circular Hough transform algorithm works. Black dots are the points on the perimeter of the real circular object that are the center of dashed line circles. The center of the real circle (solid line circle) is identified by finding the point that is shared most between the dashed line circles (red point).

The CHT algorithm in the context of our particle location methods is as follows. "*imfindcricles*" function in MATLAB has several options which can be specified by the user. Specifically, we can specify the radius of the circular objects we are looking for in the image. In addition, we can specify the sensitivity of the method in a manner that, by trial and error, leads to detection of more circles in the image.

To detect all the fine and coarse particles of dry experiments, we perform the convolution algorithm described above with the domain size roughly equal to the size of fine

particles. As we mentioned above, this presents us with locations of all the fine particles in the image; at the same time, it presents us with multiple center locations for each coarse particle. To remove these mistakenly assigned spots on the coarse particles, we use the "*imfindcricles*" function. We set the input radius to be the same as the radius of the coarse particles. This way, we detect all the coarse particles in the image. We then computationally compare the two sets of particle locations and use the approximate size of the coarse particles to remove the multiple centers assigned to them in the first step. Finally, we are left with fine particles that are detected using the local brightness maxima and coarse particles that are detected using the "*imfindcricles*" function. Figure 7.5 shows an example from an image we took during a bimodal experiment with located fine and coarse particles with this procedure.

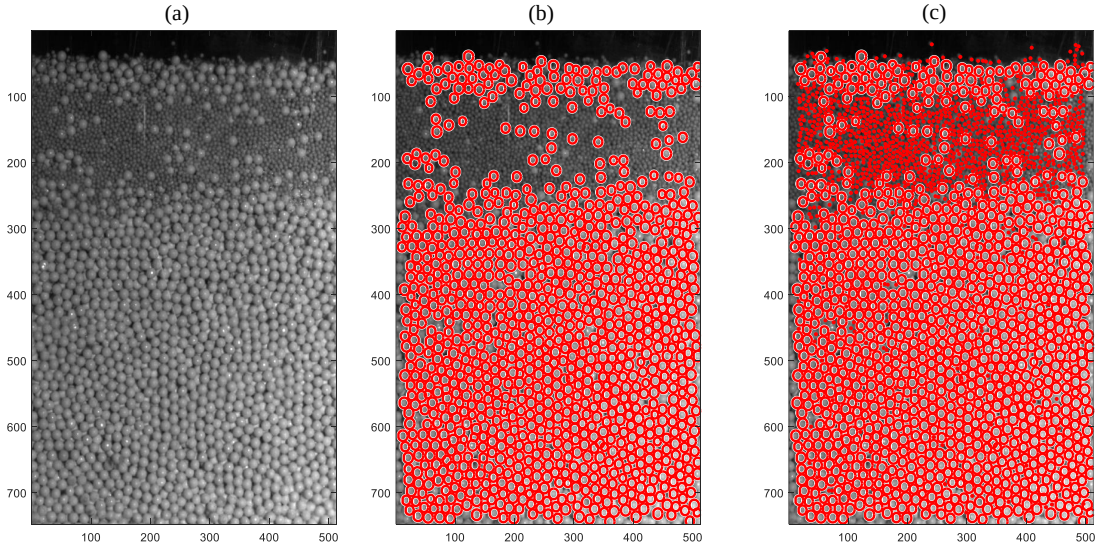

Figure 7.5: An illustration of the steps to find the fine and coarse particles in an image to minimize the noise detection. (a) shows the raw image from the high speed camera; (b) shows the coarse particles detected using the "*imfindcircle*" function in MATLAB, (c) shows all fine and coarse particles that are detected. Coarse particles are detected using "*imfindcircle*" function and fine particles are detected using the local brightness maxima algorrithm.

After locating the particles in all the frames, we calculate their displacement from

one frame to next by minimizing the distance. We use a nearest neighbor algorithm which finds the closest particle in the next frame to a specific particle in the current frame and considers the differences between these two positions as the displacement of that specific particle between two frames. Using the particles displacement information, we can calculate the velocity field of the flow which we explain in the next section.

7.2.2 Fields of Concentration, Velocity, and Velocity Fluctuations

To study the erosion rate and understand its driving forces, we need to have the information regarding the particles' density and the flow velocities. To obtain this information, we first divide each image into several horizontal bins that are parallel to the bottom of the flume. For experiments on unimodal mixtures, we choose the thickness of each bins in a manner to have 21 bins per particles diameter. For bimodal mixtures and to have the uniform thickness of bins, we choose the thickness of each bins in a manner to have 20 bins per coarse particles' diameter and 8 bins per fine particles' diameter.

Using the information obtained from the previous section by locating and tracking the particles, we find the bin that associates with center of each particles. We calculate the volume of the particle and its velocity within that bin. We do the same for the other bins that contain a portion of that particle by calculating the volume of a disk shown schematically in figure 7.6 according to:

$$\forall = \int_{y-dy/2}^{y+dy/2} \pi \left(R^2 - y^2\right) dy \tag{7.2}$$

Equation 7.2 approximates the center of each particle as perfectly aligned on the center of the bin that is associated with the central part of the particle. However, more generally, the center of the particle we calculate from the image processing algorithm does not align perfectly on the center of the bin as shown schematically in figure 7.7. To resolve this issue, we consider the distance between the center of the particle and its

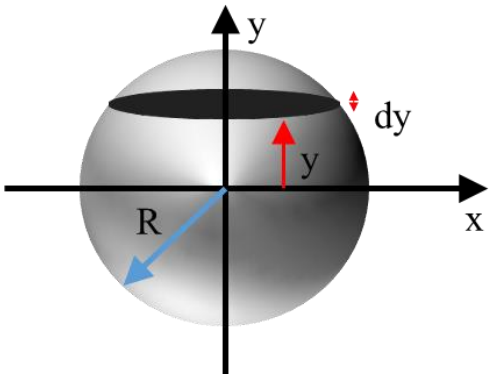

Figure 7.6: Schematic representation of a sphere and a representative disk on it. *dy* is equal to the thickness of the bins.

corresponding bin and calculate volume of each disk by the following equation which is the modified form of Eq. 7.2:

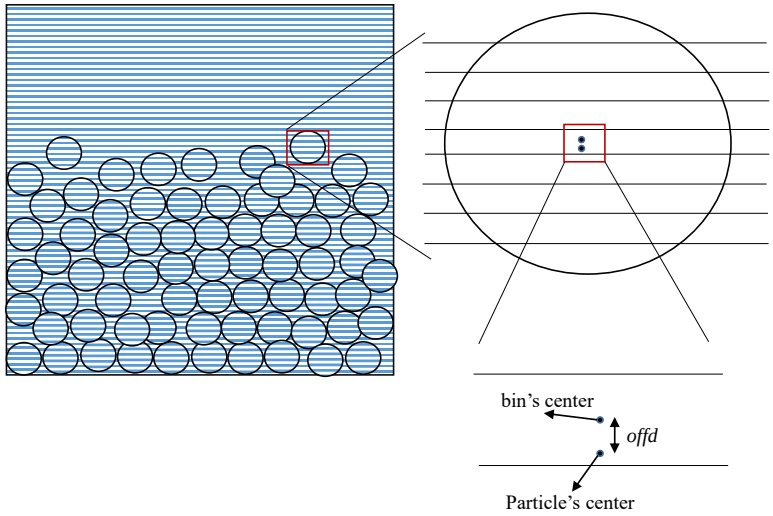

Figure 7.7: Schematic representation of a misalignment between the particle's center and bin's center.

$$\forall = \int_{y-dy/2-offd}^{y+dy/2-offd} \pi \left(R^2 - y^2\right) dy \tag{7.3}$$

where *offd* is the difference between the center of the particle and the bin.

After performing these calculations for all the particles in each frame, we calculate the average solid fraction in each bin as (Hill et al. (2003); Moberly (2015); Mullenbach (2018)):

$$\overline{f}(y) = \overline{f}_{By} = \Sigma_i \Sigma_b \forall_i^b / (N_t \forall_B) \tag{7.4}$$

where $f(y)$ is the solid fraction at the vertical location, y; B_y refers to the bin which centered at y; $\forall_B$ is the volume of the bin; $\forall_i^b$ is the volume of the portion of particle b that falls within bin B_y in image i. To reduce the noise associated with instantaneous calculations, we time-average the calculations over several images and N_t refers to this number of images. The results of Moberly (2015) have shown that averaging over 50 images would be a sufficient number to remove the noise but not the details of the flow dynamics.

After calculating the solid fraction of each bin, we calculate the average streamwise and vertical velocity of each bin, over 50 images, from the information we obtained about their displacement in our tracking algorithm:

$$\overline{u}(y) = \overline{u}_{By} = \frac{\Sigma_i \Sigma_b \forall_i^b \times u_i^b}{\Sigma_i \Sigma_b \forall_i^b} \tag{7.5a}$$

$$\overline{v}(y) = \overline{v}_{By} = \frac{\Sigma_i \Sigma_b \forall_i^b \times v_i^b}{\Sigma_i \Sigma_b \forall_i^b} \tag{7.5b}$$

where $\overline{u}(y)$ and $\overline{v}(y)$ are the average streamwise and vertical velocity of the bin centered at y and averaged over 50 images. u_i^b and v_i^b are the instantaneous streamwise and vertical velocities of particle b in image i, respectively.

For the experiments on the bimodal mixtures, we do the above calculations for each particle size. Then, we add the solid fraction of fine and coarse particles in each bin to calculate the total flow solid fraction. To calculate the total flow velocities, we calculate the weighted average of these velocities from fine and coarse particles:

$$f_{mix}(y) = f_f(y) + f_c(y) \tag{7.6a}$$

$$u_{mix}(y) = \frac{f_f(y) \times u_f(y) + f_c(y) \times u_c(y)}{f_f(y) + f_c(y)} \tag{7.6b}$$

$$v_{mix}(y) = \frac{f_f(y) \times v_f(y) + f_c(y) \times v_c(y)}{f_f(y) + f_c(y)} \tag{7.6c}$$

where f_{mix}, u_{mix}, and v_{mix} are the mixture solid fraction, streamwise and vertical velocity at y, respectively. The subscripts "f'' and "c'' stand for "fine" and "coarse" particles, respectively.

Figure 7.8 shows a snapshot of an experiment the flow at 2.5 seconds after we initiate the experiment with an initial debris flow of 0.8 mm particles of a bed of 2.0 mm particles. Figures 7.8(b) and 7.8(c) provide the corresponding concentration and streamwise velocity profiles at that instance for fine and coarse particles and the mixture throughout the depth of the system. We note that our calculations for streamwise velocity of fine particles include noisiness, specifically for the parts deep in the bed where the concentration of fine particles are negligible. Because the noisiness is greatest in the depth, where the small particle concentration is low, the contribution of these noises on the velocity profile of the mixture is negligible. This allow us to use our image processing algorithms for the experiments we performed in this study. However,

improving our algorithms for particles locating and tracking is a work in progress.

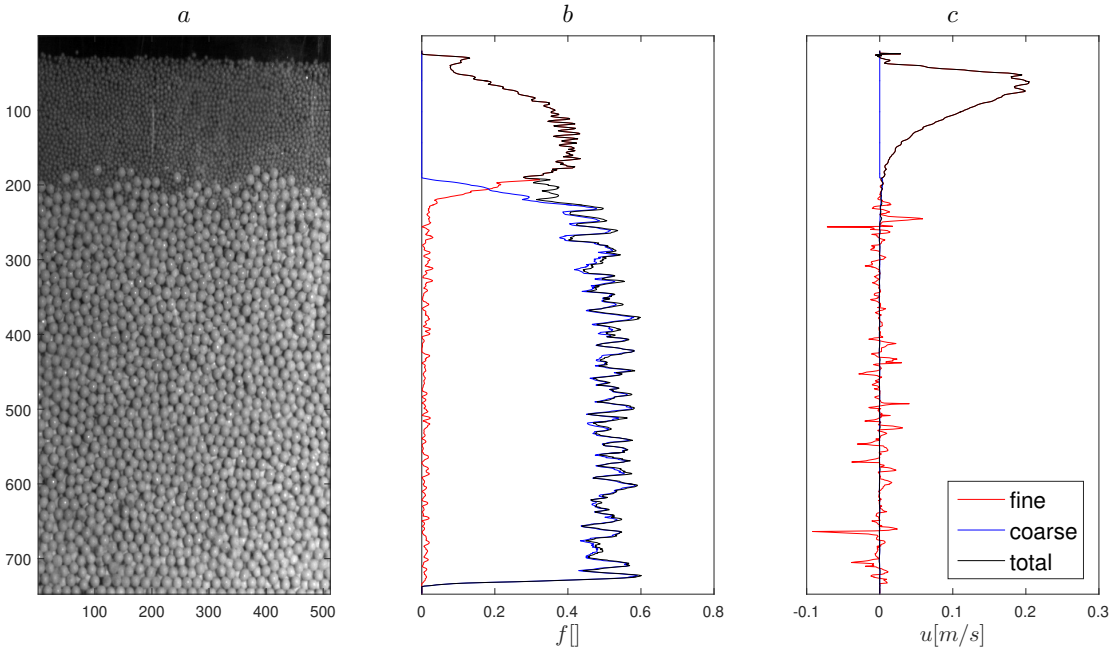

Figure 7.8: Illustration of profiles calculation for bimodal mixtures. (a) shows a snapshot of the flow at 2.5 seconds after initiation of the flow for the experiment with 100 % fine particles in the supply. (b) shows the concentration profile of fine, coarse and mixture. (c) shows the streamwise velocity profile of fine, coarse and mixture.

7.2.3 Flow Dynamics Calculations

For a qualitative measurement of the entrainment rate of bed materials by debris flows, we need to define an interface that distinguishes flowing layer from the erodible bed. The changes in the location of this interface indicates the growth rate of debris flows by entraining materials. To determine this interface which from now we call it *entrainment height*, we compare the downstream velocity of each bin, calculated in the previous section, with a critical velocity, u_{crit}. We define a bin is part of the flow if its downstream velocity is greater than the critical velocity.

Other researchers (i.e. Hill et al. (2003); Gioia et al. (2006); Frey and Church (2011);

Forterre and Pouliquen (2008); Mangeney et al. (2007, 2010)) have shown that the velocity of particles in deep layers of flow decays exponentially with depth. Therefore, setting the critical velocity to zero is not a reasonable choice. In addition, the particles deep in the bed may assigned a very small velocity due to either shakes of the fume or our particles' locating procedure. Therefore, for this study, we choose $u_{crit} = 0.01$ m/s. To determine the entrainment height, we fit a linearized least squared to the logarithmic values of the downstream velocity (See Fig. 7.9):

$$y_{bot,fit,j}(u_j) = m_j \ln(u_j(y)) + b_j \tag{7.7}$$

where m_j and b_j are the fitting coefficients determined from the least square method for each average set, j. After finding these coefficients, we can determine the entrainment height:

$$H_{ent} = m_j \ln(0.01) + b_j \tag{7.8}$$

Using this way of determining the entrainment height, we can track the changes in this height during the course of our experimental tests. In addition, we can determine the changes in this height with time, which we refer to as *entrainment rate* ($\dot{e}$) here and henceforth. We calculate this rate by calculating the changes in the entrainment height over a specified time interval:

$$\dot{e} = -\frac{\Delta H}{\Delta t} \tag{7.9}$$

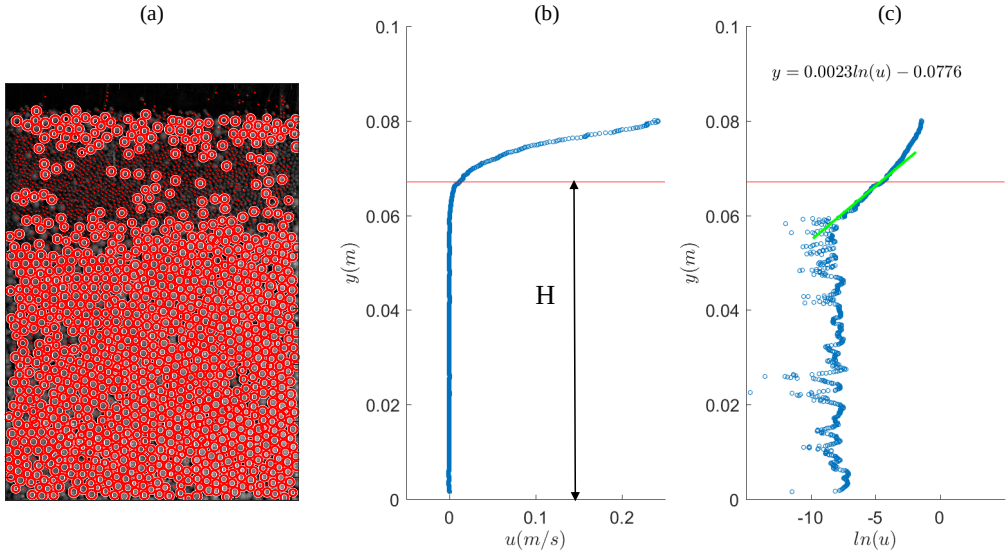

Figure 7.9: Illustration of our methodology in determining the entrainment height. (a) shows the detected fine and coarse particles, b) shows the mixture velocity profile of the flow at an instantaneous time, and the entrainment height (H) which is measured from the bottom of the channel to the interface between the flowing layer and the erodible bed. c) shows the linearized least square fitting between the natural log of the velocity data for mixtures and the height.

Here, ΔH is the change in entrainment height over time interval Δt. The negative sign came from the fact that we define the entrainment rate as positive when the entrainment height decreases. To calculate the entrainment rate in this study at each time step, we choose the entrainment height values for four time steps before and after the current time step. Fig. 7.10 illustrates our methodology in determining the entrainment rate.

In addition to using the tracking data to calculate an entrainment height and its changes over time, we use the data to calculate potential driving forces for these changes. Previous studies (Berger et al. (2011); Berti et al. (2000); Moberly (2015); Mullenbach (2018)) have suggested different factors such as *shear stress* and *granular temperature* of the flowing layer control the changes in entrainment height. We note that in other

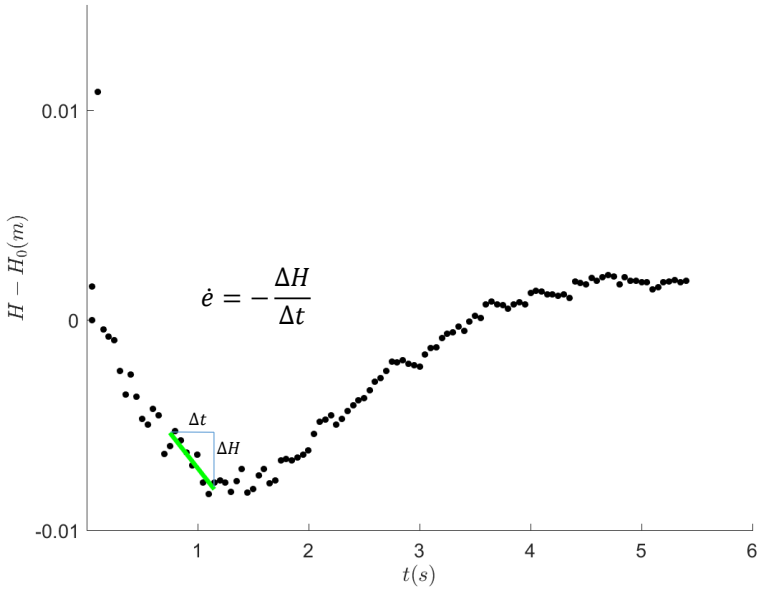

Figure 7.10: The changes in entrainment height over time. The slope of these changes indicates the entrainment rate.

contexts, issues of segregation and infiltration related to mixed grain sizes play a role in sediment entrainment and transport (Dudill et al. (2017)). We investigate some of these effects in the context of changing grain size distribution as we describe in more detail in the next chapter.

Chapter 8

Experimental findings of the dependence of debris flow erosion rates on particle size

We divide this chapter into four parts. In the first part, we present our results regarding the *net eroded mass* measured from our experiments on unimodal and bimodal mixtures. Specifically, this includes the experiments and results obtained concerning the dependence of total net erosion on (1) the grain size in the bed and flow in single-sized particle systems and (2) the grain size distribution of the initial debris flow, our "supply composition" in bimodal mixtures at the flume and bed angle of inclination equal to the neutral angle of the bed material.

In the second part, we present the results of how the time-dependent near-instantaneous erosion rate depends on the initial debris flow or "supply composition," when the original bed material is kept the same from one experiment to the next.

In the third part we discuss the results of the time-dependent erosion rate in the context of hypothesized controls over the erosion rate. We do this in the context of our grain-sized dependent particle tracking and image analyses procedure.

We conclude the chapter with a brief discussion of the results and the strengths and weaknesses of this framework.

8.1 Macroscopic analyses of net eroded mass by debris flows

8.1.1 Combined roles of bed angle of inclination and material

To understand the roles of combined bed-supply materials and the angle of bed inclination for our set of particles on the erosion of bed materials by debris flows, we performed what we call "uniform particle experiments." For these experiments, all particles (in the initial debris flow and in the bed) were the same and we varied the inclination angle from one experiment to the next.

For the first set of experiments, we performed several experiments, as detailed in Table. 8.1, on different inclination angles for each particle size. For each experiments, we calculate the normalized net mass eroded:

$$\hat{m}_e = \frac{m_{out} - m_{initial}}{m_{initial}} \tag{8.1}$$

Here, $\hat{m}_e$ is the normalized net eroded mass, m_{out} is the mass exited the flume, and $m_{initial}$ is the initial debris flow mass. A positive value of $\hat{m}_e$ indicates that the flow is net erosional which means the total mass of particles that leaves the flume by the end of the experiment is more than what supplied by the initial debris flow. In a similar way, a negative value of $\hat{m}_e$ indicates that the flow is net depositional, that is, once all flow has stopped, less mass leaves the bed than was supplied by the initial debris flow.

We use a linearized least squares fit to determine a straight line that represents the relationship between the $\hat{m}_{e,fit}$ and ϕ data.

Table 8.1: Particle properties and input parameters for uniform particle experiments.

Experiment	$\rho(kg/m^3)$	d (mm)	$m_{initial}(kg)$	$m_{bed}(kg)$	$\phi(deg)$
1	4100	0.8	6.6	17.1	22.5
2	4100	0.8	6.6	17.1	23.5
3	4100	0.8	6.6	17.1	24.5
4	4100	0.8	6.6	17.1	25.0
5	4100	0.8	6.6	17.1	25.5
6	4100	2.0	6.6	17.1	24.0
7	4100	2.0	6.6	17.1	25.0
8	4100	2.0	6.6	17.1	25.5
9	4100	2.0	6.6	17.1	26.0
10	4100	2.0	6.6	17.1	27.0

$$\hat{m}_{e,fit} = \frac{\Delta\hat{m}_{e,fit}}{\Delta\phi} \times (\phi_{fit} - \phi_n) \tag{8.2}$$

where $\frac{\Delta\hat{m}_{e,fit}}{\Delta\phi}$ and ϕ_n are fitting parameters. We provide values for these parameters in table 8.3 and discuss the significance of those parameters in Section 8.4.

8.1.2 Effects of initial debris flow concentration

We performed a second set of experiments where we maintained a constant bed composition and bed inclination and varied the composition of the initial debris flow (or "supply") from one experiment to the next. We performed five sets of experiments using an initial bed comprised only of 2.0 mm particles and another five sets of experiments using an initial bed comprised only of 0.8 mm particles. where the bed was uniformly composed of one size particles but the percentage of finer and coarser particles in supply

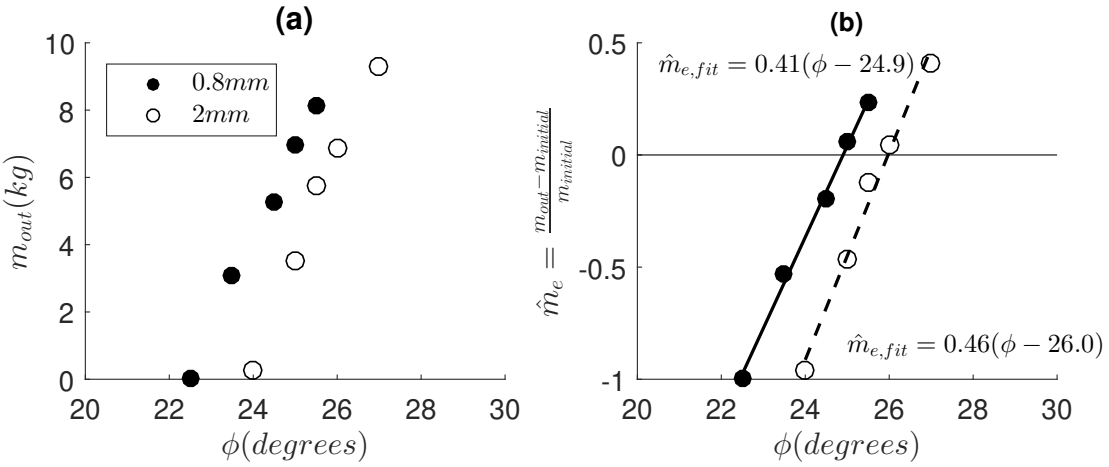

Figure 8.1: Net eroded mass as a function of bed inclination, ϕ. (a) total mass discharged from the system, m_{out}, (b) normalized net mass out, $\hat{m}_e = \frac{m_{out}-m_{initial}}{m_{initial}}$. The lines represent linearized least square fit lines, Eq. 8.2.

was varied. We performed both sets of experiments with the bed inclined at the angle at which, in Section 8.4.1 we demonstrated that there was no net erosion. We used an inclination angle of approximately 26° for the experiments with a bed composed of coarse particles, and approximately 23.5° for the experiments on a bed composed of finer particles.

We performed several "mixture erosion experiments" for each of the two types of particles, for which we varied the percentage of fine and coarse particles in the initial flow as detailed in table 8.2. The fine bed particles ($d_b = 0.8\ mm$) was not stable under the same conditions, thus for these we performed the experiment using a somewhat lower angle than that at which we achieved stability ($\phi = 23.5° < 24.9° = \phi_n$). Fig. 8.2 shows the normalized net eroded mass as a function of % fine particles in the initial flow.

The results from the "mixture erosion experiments" presented in Fig. 8.2 shows that, when the bed was comprised only of 2.0 mm particles, we found the total net eroded mass decreases with increasing fraction of fine particles in the initial debris flow, or supply.

Table 8.2: Input parameters for mixture erosion experiments.

Experiment	$d_b(mm)$	$d_{s,c}(mm)$	$d_{s,f}(mm)$	$\phi(deg)$	% fines in initial flow
1	0.8	2	0.8	23.5	0
2	0.8	2	0.8	23.5	25
3	0.8	2	0.8	23.5	50
4	0.8	2	0.8	23.5	75
5	0.8	2	0.8	23.5	100
6	2	2	0.8	26.0	0
7	2	2	0.8	26.0	25
8	2	2	0.8	26.0	50
9	2	2	0.8	26.0	75
10	2	2	0.8	26.0	100

In contrast, when the bed composed only of fine particles, we found no systematic changes in the total net eroded mass as we change the percentage of coarse particles in the supply. We note that the results for the 2.0 mm and 0.8 mm particle evaluated individually varies a bit more. One might expect that the normalized net erosion of one component should be proportional to its representation in the initial flow. However, for the bed composed of coarse particles, the normalized net eroded mass of fine particles decreases with increase of fine particles, while the normalized net eroded mass of the coarse particles is relatively flat. In the case of bed composed of fine particles, the normalized net eroded mass of the fine particles increases slightly overall, while the normalized net eroded mass of coarse particles increases with decreasing representation of coarse particles in the initial debris flow.

In the next section, we analyzed some of the experiments presented in this section through our image analyses algorithm to provide a better understanding of underlying mechanisms at particle-scale that leads to the results presented in this section.

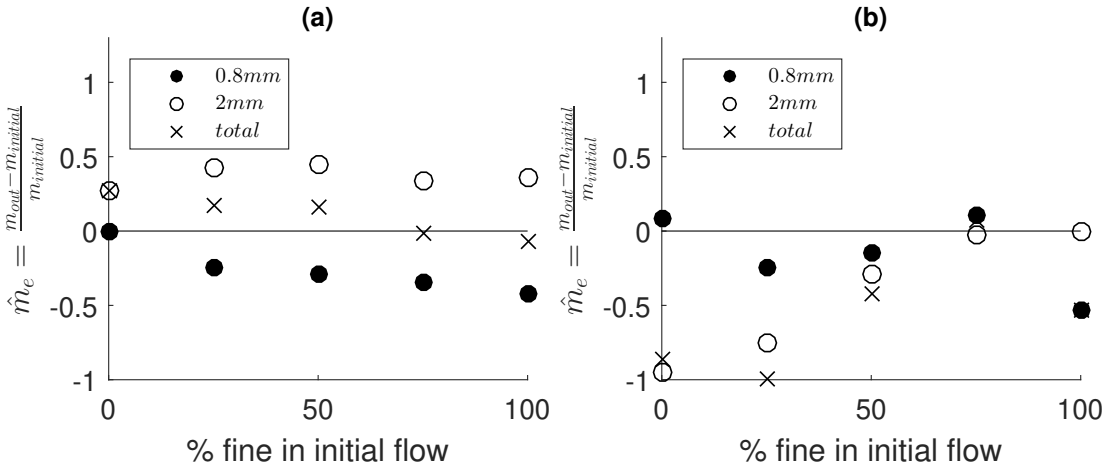

Figure 8.2: Normalized net eroded mass for each component and total as a function of concentration of the fine particles in the supply. (a) shows the normalized net eroded mass for bed composed of coarse particles, (b) shows the normalized net eroded mass for bed composed of fine particles.

8.2 Instantaneous particle-scale measurements of dynamics associated with debris flow erosion

Towards understanding the driving forces of erosion rate at particle-scale, we choose a subset of the experiments we described in the previous section to analyze in more detail. In particular, we choose the experiments we performed on a bed composed of coarse particles only (experiments 6 through 10 in Table 8.2) . In this section we consider the dynamics of the erosion rates and potential drivers as they vary with concentration of fine particles in the initial debris flow.

We start by considering the entrainment height (the interface between the stationary bed and flowing layer) and entrainment rate as they vary with time for these five experiments. These two parameters are introduced before in section 7.2.3. Figure 8.3a shows the entrainment height ($H - H_0$ where H_0 is the initial bed height) as it varies in time for five different concentrations of fine particles in the initial debris flows.

All of the experiments exhibit decreasing bed height as a function of time for the

dense flow first impinges on the bed ($\approx$ 1 s to 1.5 s following the time at which the dense flow impinges on the bed). As seen in this figure, the entrainment height drops sharply in the beginning of the experiments when we have 50 to 75 percent by mass fine particles in the supply. Figure 8.3b shows the entrainment rates of these experiments over the course of each test in which we can associate the initial drop in the entrainment height with an initial positive entrainment rate.

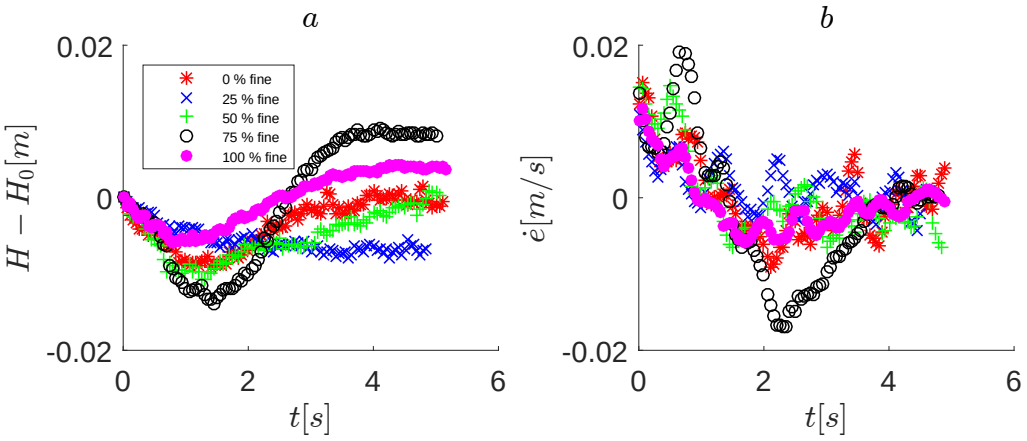

Figure 8.3: Time series of (a) entrainment height, (b) entrainment rate. H_0 is the entrainment height at the initial time.

For additional information on these results, we consider the velocities and concentrations. For a few examples, we provide these results, along with a snapshot, for three experiments: that with 25% fine particles in the initial debris flow (Fig.8.4); that with 75% fine particles in the initial debris flow (Fig.8.5), and that with 100% fine particles in the initial debris flow (Fig.8.6).

When we compare these three sets of ***snapshots*** with one another, we notice a few obvious similarities and differences among these three experiments.

- For all cases the state of the particles in the snapshots indicate a more energetic flow at 1 seconds after the impinging of the dense flow on the bed than at 2 seconds

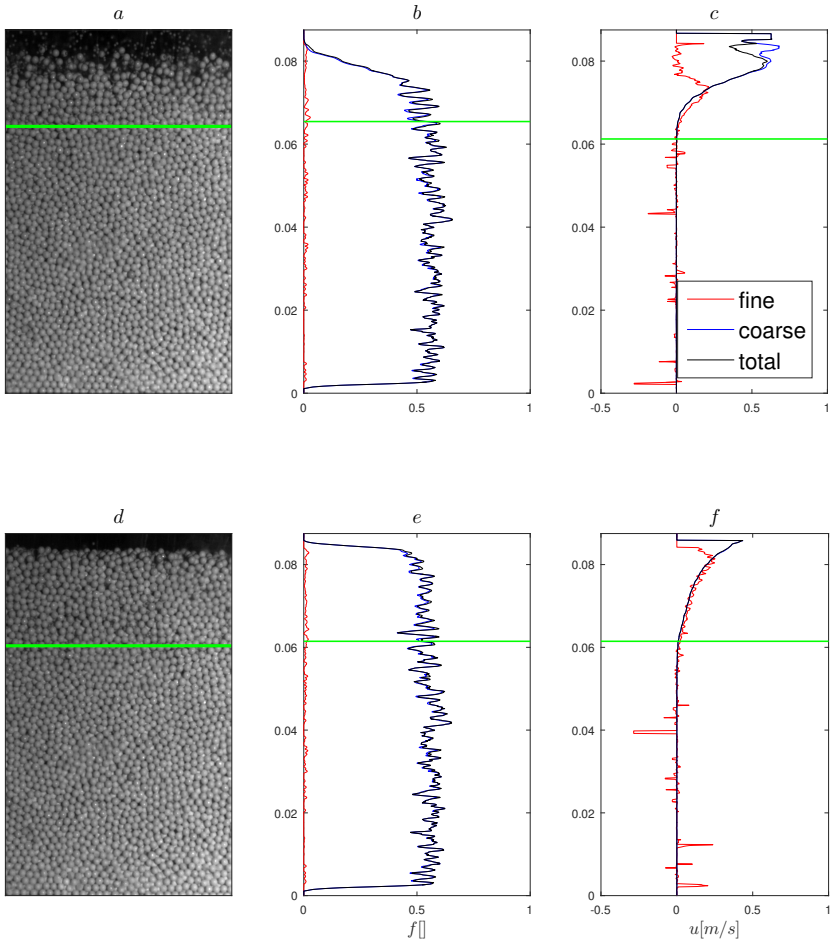

Figure 8.4: (a) A snapshot of flow at 1 seconds after the start of flow for experiment with 25 % fine particles in the supply. Green line shows the entrainment height (the interface between the flowing layer and stationary bed). (b) shows the concentration profile for fine, coarse, and their combination. (c) shows the downstream velocity profiles of fine, coarse and their combination. (d-f) shows the snapshot, concentration profiles, and downstream velocity profiles, respectively, for 2 seconds after the start of the flow.

after initiation.

- The relative locations of the fine particles and coarse particles indicate that the fine particles infiltrate more into the bed for the experiment with 75% fines in the supply compared to the other two experiments. We note the 75% case is the case with an intermediate percentage of fines in the initial debris flow compared with

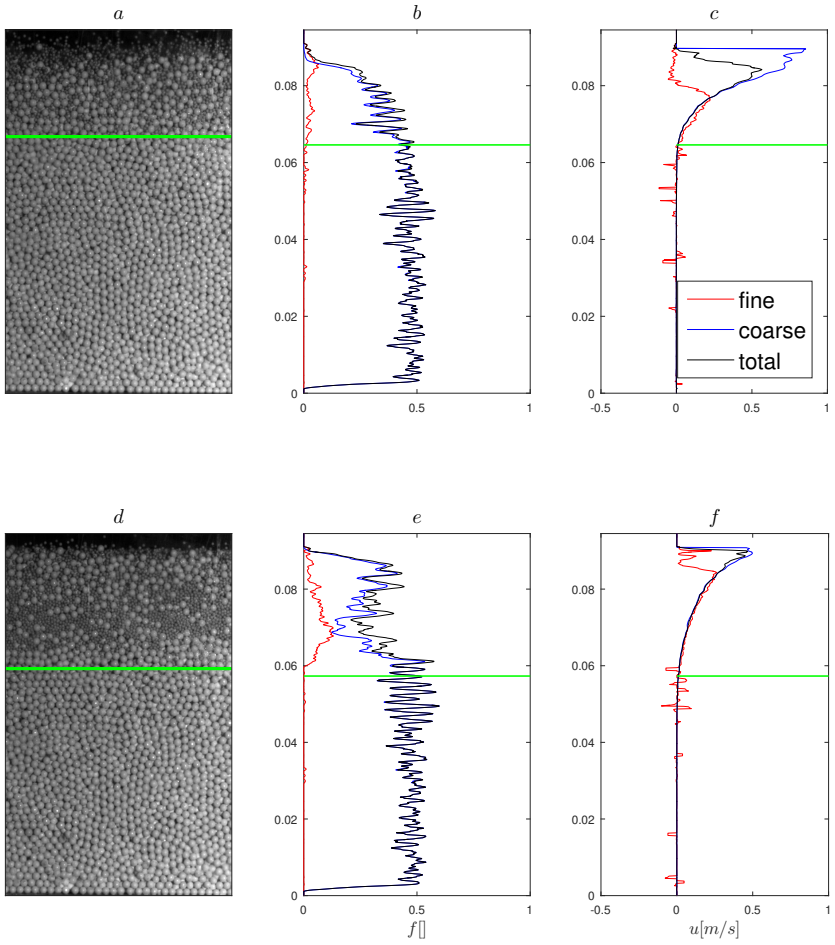

Figure 8.5: (a) A snapshot of flow at 1 seconds after the start of flow for experiment with 75 % fine particles in the supply. Green line shows the entrainment height (the interface between the flowing layer and stationary bed). (b) shows the concentration profile for fine, coarse, and their combination. (c) shows the downstream velocity profiles of fine, coarse and their combination. (d-f) shows the snapshot, concentration profiles, and downstream velocity profiles, respectively, for 2 seconds after the start of the flow.

the other two we compare here.

When we compare these three sets of ***concentration profiles*** and ***velocity profiles*** with one another other, a few more details emerge.

- The flow velocity for all three experiments is higher at 1 seconds after the initiation of the experiment compare to the velocity at 2 seconds after the initiation. This

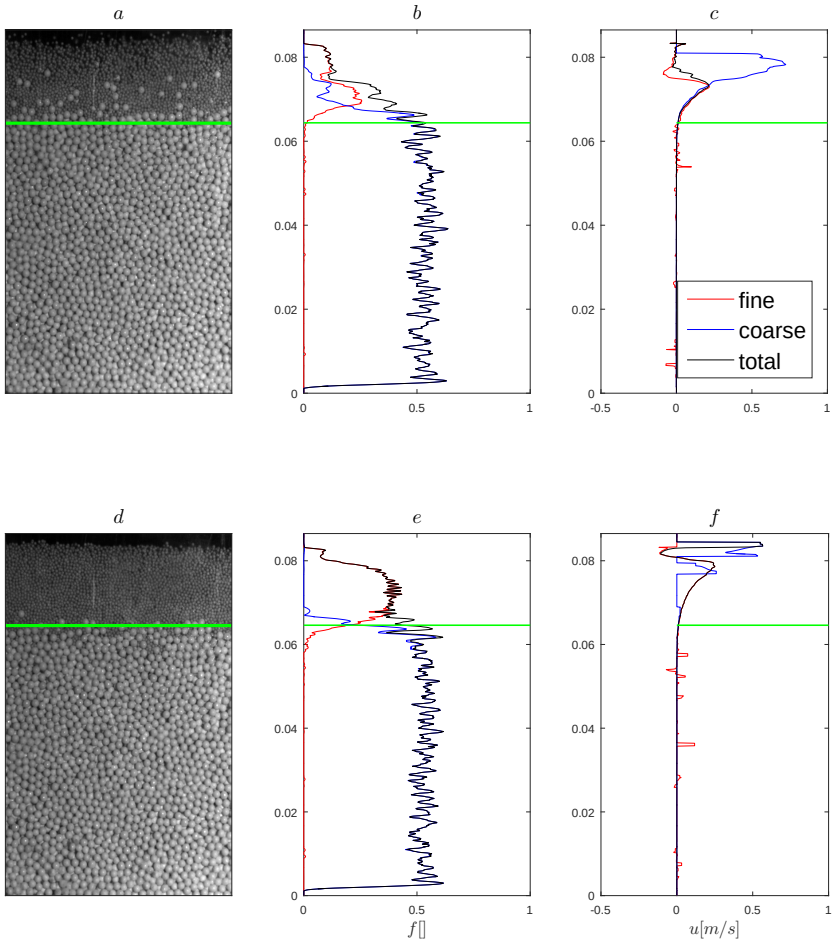

Figure 8.6: (a) A snapshot of flow at 1 seconds after the start of flow for experiment with 100 % fine particles in the supply. Green line shows the entrainment height (the interface between the flowing layer and stationary bed). (b) shows the concentration profile for fine, coarse, and their combination. (c) shows the downstream velocity profiles of fine, coarse and their combination. (d-f) shows the snapshot, concentration profiles, and downstream velocity profiles, respectively, for 2 seconds after the start of the flow.

is in agreement with the snapshots that show a more energetic flow at 1 seconds after the initiation of the flow.

- The concentration profiles support the general picture provided by the snapshots, that fine particles infiltrates more into the bed for the experiment with 75% fines in the supply compare to the other two experiment where we have more or less

fine particles in the supply.

- Only for the experiment with 75% fines in the initial debris flow, the bottom of the fine particles appears to reach the location of the entrainment height. In other words, the fine particles are able to reach the point at which the flowing particles interact with relatively stationary particles.
- Only for the experiment with 100% fine particles in the initial debris flow, the interface between moving particles and the bed never penetrates into a region of high concentration of large particles. That is, during these relatively early times in the experiment, the entrainment height remains near the interface between the fine and coarse particles.

8.3 Other macroscopic fields and their influence on erosion rates

In this section, we explore the dependence of erosion rate on two factors proposed by other researchers. In particular (since the effect of interstitial fluid is negligible in our experiments), we consider the average shear stresses and granular temperature as described in the following sections to consider whether these parameters influence the erosion rate in our experiments.

8.3.1 Shear stress

We calculate the average shear stress due to the weight of particles in the flowing layer on the interface between the flowing layer and stationary bed:

$$\tau = \rho_s \overline{f} g h sin(\theta) \tag{8.3}$$

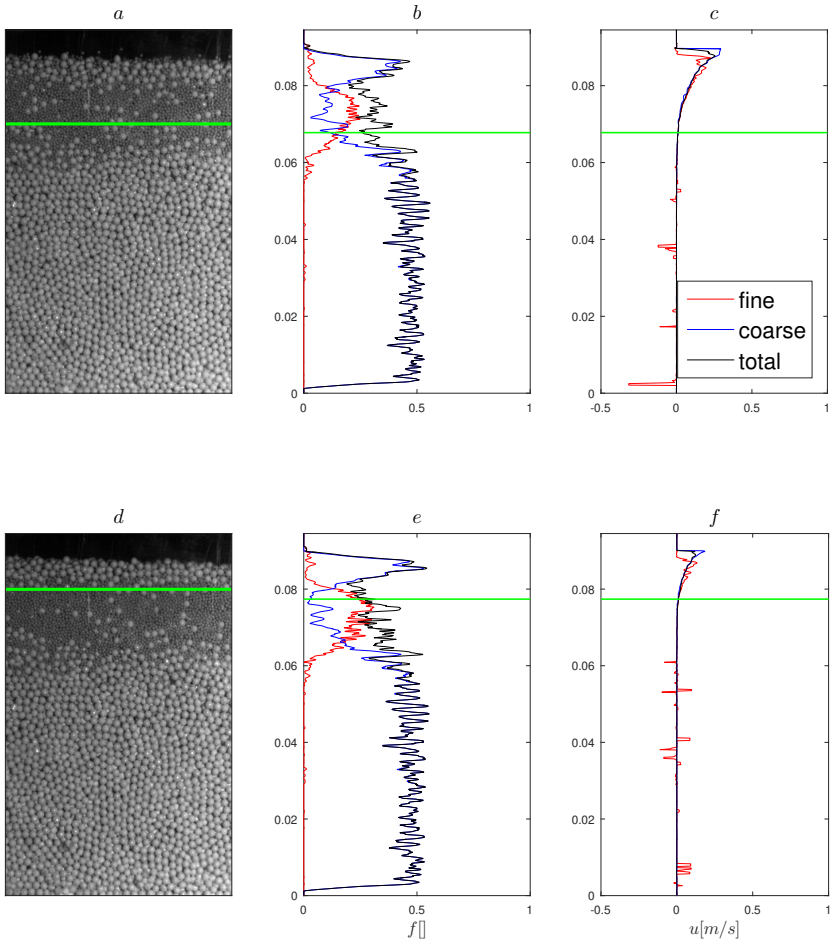

Figure 8.7: (a) A snapshot of flow at 3 seconds after the start of flow for experiment with 75 % fine particles in the supply. Green line shows the entrainment height (the interface between the flowing layer and stationary bed). (b) shows the concentration profile for fine, coarse, and their combination. (c) shows the downstream velocity profiles of fine, coarse and their combination. (d-f) shows the snapshot, concentration profiles, and downstream velocity profiles, respectively, for 4 seconds after the start of the flow.

Figure 8.10 shows the average shear stress over the course of experiments for each tests. This figure shows the average shear stress, in general, increases as the amount of fine particles in the supply decreases. We know from Eq. 8.3 that the magnitude of the shear stress depends on the thickness of the flowing layer. Therefore, we conclude that the flow thickness increases as the percentage of fine particles in the supply decreases. To understand if the shear stress (or similarly the flow thickness) controls the erosion

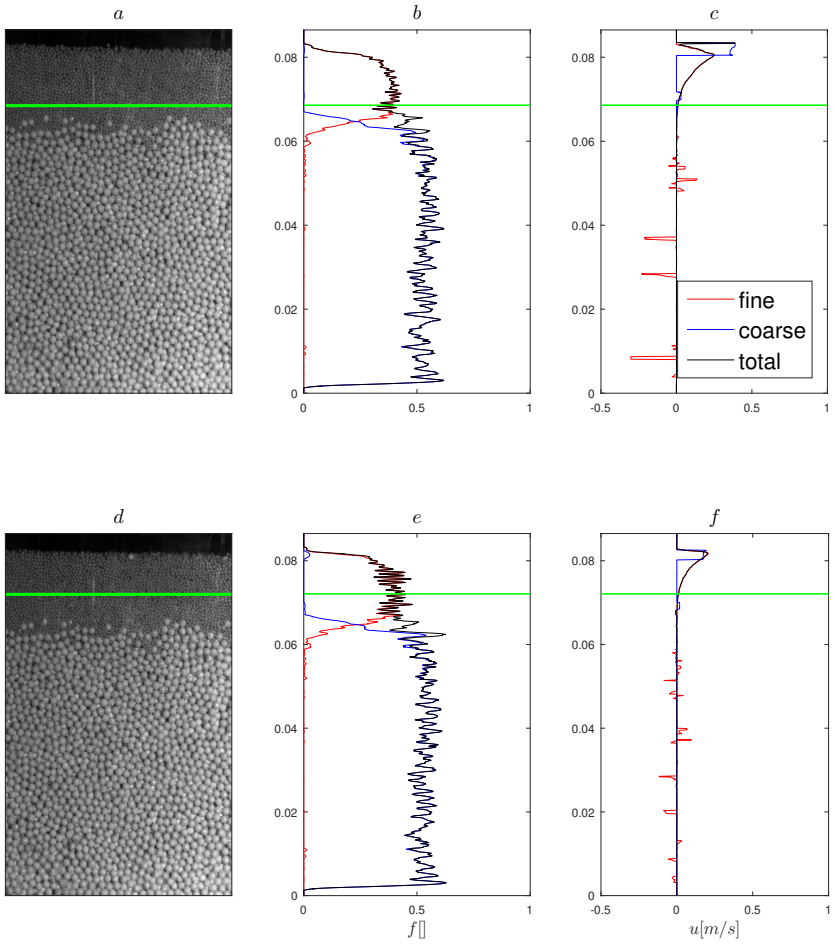

Figure 8.8: (a) A snapshot of flow at 3 seconds after the start of flow for experiment with 100 % fine particles in the supply. Green line shows the entrainment height (the interface between the flowing layer and stationary bed). (b) shows the concentration profile for fine, coarse, and their combination. (c) shows the downstream velocity profiles of fine, coarse and their combination. (d-f) shows the snapshot, concentration profiles, and downstream velocity profiles, respectively, for 4 seconds after the start of the flow.

rate, we plot the erosion rate versus shear stress on the inset of Fig. 8.10. As clear in this figure, there is not a significant correlations between the shear stress and the erosion rate. Specifically, we notice that the range of changes in erosion rate is similar for two cases: 100 % fines in the supply and 0 % fines in the supply. However, in the latter cases the range of changes in shear stress is about 3 times larger than the other case. Therefore, we think that other factors rather than the shear stress should control

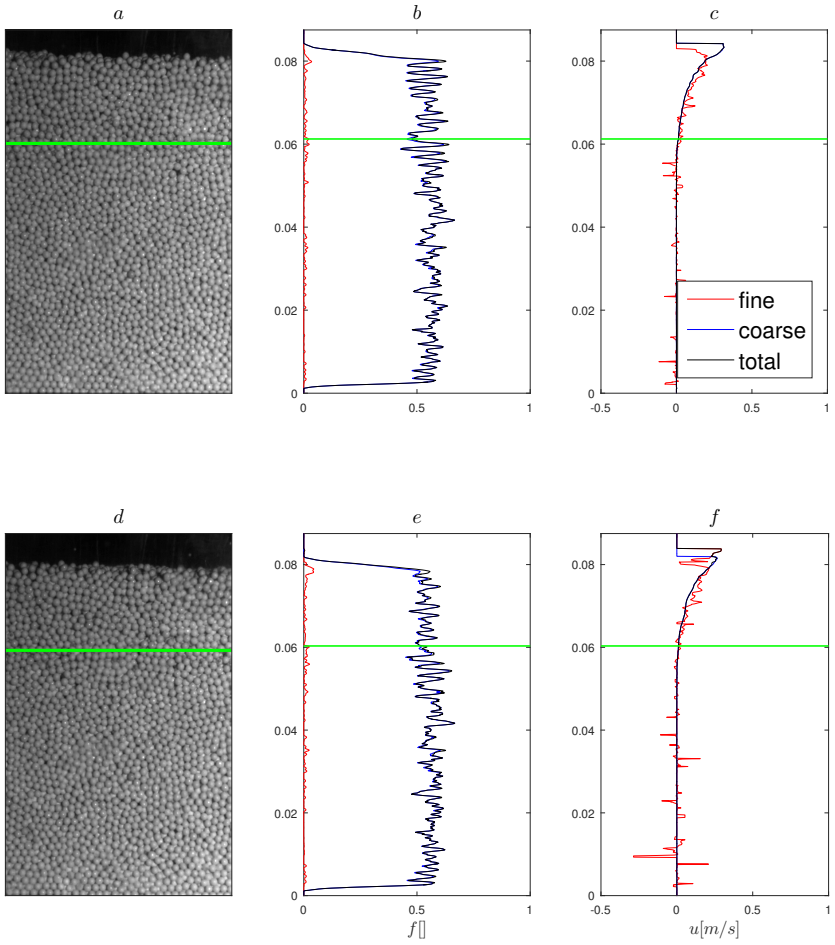

Figure 8.9: (a) A snapshot of flow at 3 seconds after the start of flow for experiment with 25 % fine particles in the supply. Green line shows the entrainment height (the interface between the flowing layer and stationary bed). (b) shows the concentration profile for fine, coarse, and their combination. (c) shows the downstream velocity profiles of fine, coarse and their combination. (d-f) shows the snapshot, concentration profiles, and downstream velocity profiles, respectively, for 4 seconds after the start of the flow.

the erosion rate. In the next section, we investigate the dependence of the erosion rate on granular temperature.

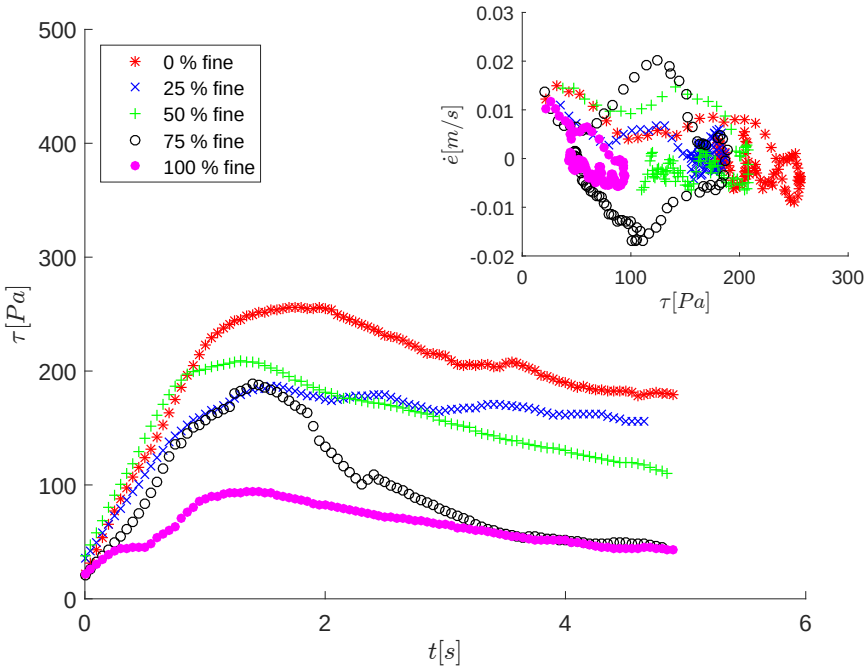

Figure 8.10: Plot of average shear stress (τ) through time on the interface between the flowing layer and stationary bed. The inset shows the plot of erosion rate vs average shear stress for the course of the experiment.

8.3.2 Granular temperature

We calculate the average granular temperature for the dense flowing layer based on velocity variations near the interface between the bed and the dense flowing layer.

We start with the instantaneous and local velocity vectors calculated throughout the experiment and also the near-instantaneous velocity fields calculated according to Equation 7.5. We then calculate profiles of the correlations of the velocity fluctuations according to the following equations:

$$\overline{\sigma}_u(y) = \overline{\sigma}_{u_{By}} = \frac{\Sigma_i \Sigma_b \forall_i^b \times (u_i^b - \overline{u}_{By}) \times (u_i^b - \overline{u}_{By})}{(N_t \forall_B)} \tag{8.4a}$$

$$\overline{\sigma}_v(y) = \overline{\sigma}_{v_{By}} = \frac{\Sigma_i \Sigma_b \forall_i^b \times (v_i^b - \overline{v}_{By}) \times (v_i^b - \overline{v}_{By})}{(N_t \forall_B)} \tag{8.4b}$$

We calculate a "granular temperature" according to the sum of these velocity variations for the dense flowing layer:

$$T = \frac{\sum_{y=H}^{y=h_{top}} \rho_s f(y) \left(\overline{\sigma}_u(y) + \overline{\sigma}_v(y)\right)}{h_{top} - H} \tag{8.5}$$

In this equation, H is the entrainment height, and h_{top} is the top of the flowing layer.

Figure 8.11 shows the plot of average granular temperature over time for each of the experiments. In contrast to the plot of average shear stress, there is no systematic variations between the average granular temperature with the percentages of fine particles in the supply. Instead, the granular temperature is highest, at early stages of the flow, for experiments that have 25 and 50 percent of fine particles in the supply. To understand if the granular temperature determines the erosion behavior of the flow observed before in Fig. 8.3b, we plot these two parameters against each other on the inset of Fig. 8.11. The inset shows no clear dependence between the erosion rate and granular temperature except, perhaps, at very early times.

Previous studies by Longjas and Hill (2020); Moberly (2015) shows a correlation between the granular temperature and erosion rate at early stages of the flow. To investigate if the same positive correlation exist for the experiments of this study, we plot the erosion rate versus granular temperature for the early stages of the flow (from 0.5 seconds to 1.5 seconds). As we can see from Fig. 8.12, there is a slightly positive correlation between the granular temperature and shear rate at early stages of the flow, except the experiment with 100% fines in the supply that shows a negative correlation between these two at early stages of the flow.

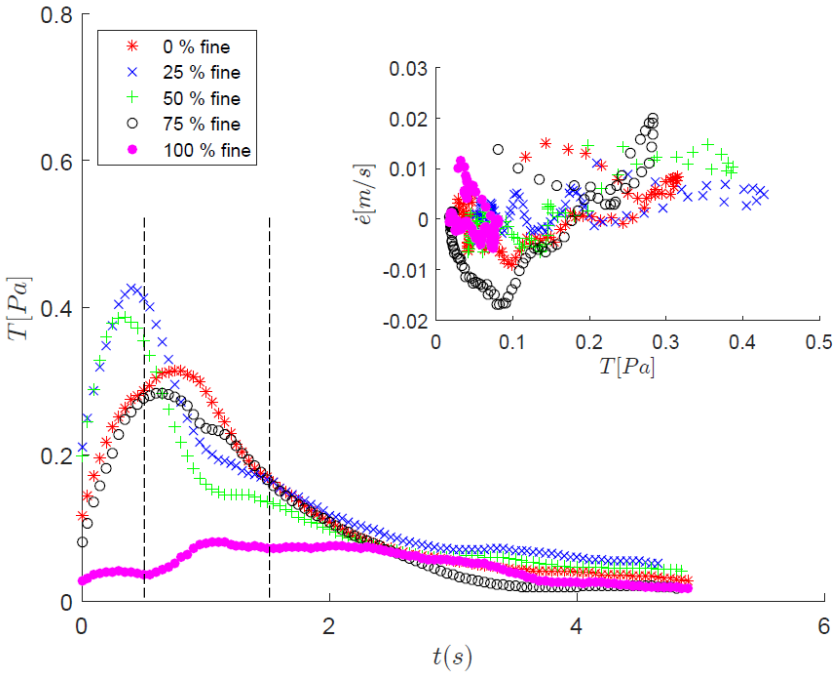

Figure 8.11: Plot of average granular temperature (T) through time for the dense flowing layer. The inset shows the plot of erosion rate vs average granular temperature for the course of the experiment.

8.4 Discussion of Debris Flow Results

We note that there are a number of similarities in the results we present here and previous results obtained in this flume (e.g., by Maki (2018) and Moberly (2015)). The ways in which our results differ provide important insights to experimental debris flow as we discuss here.

8.4.1 Dependence of erosion on bed angle

Similar to the results of Hill et al. (2013); Maki (2018), Fig. 8.1 demonstrates that the total net erosion in our experiments increases linearly with the inclination angle, ϕ. The linearity of these results is independent of bed material (compared with the Maki (2018) that used glass particles for her experiments, while we used denser zirconium silicate

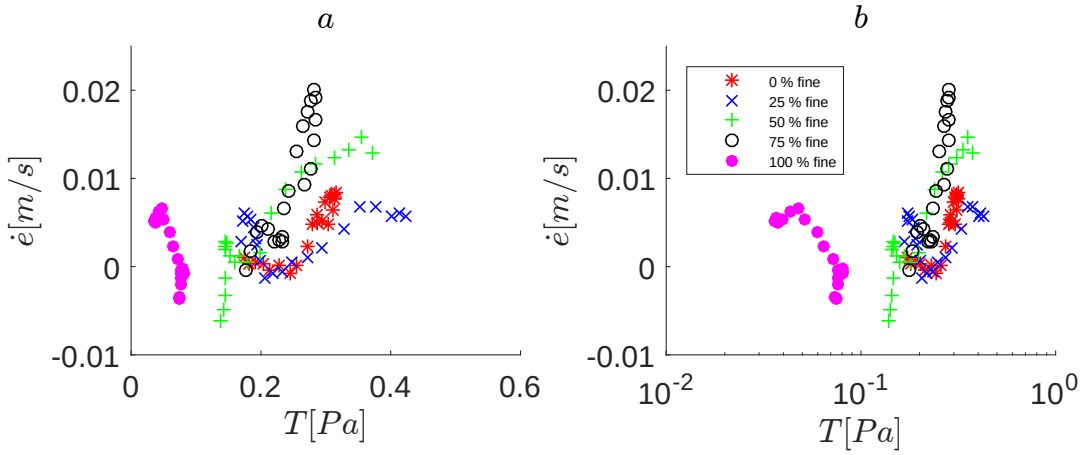

Figure 8.12: Plot of erosion rate ($\dot{e}$) for early stages of the flow (0.5 - 1.5 seconds) against the average granular temperature.

particles). On the other hand, we recall (from Chapter 6) that Maki (2018) recorded an erosion dependence that increased with large particles in the initial debris flow, or supply, regardless of whether there were large or small particles in the bed. This is in contrast with our results for the small-particle bed, where the dependence of net total erosion on concentration of large particles was ambiguous.

We hypothesize that the difference lies in certain particle properties as they manifest in natural angles of the two types of particles in the two different mixtures. We follow the example of Hill et al. (2013); Maki (2018) and assign the fit parameter ϕ_n to the neutral angle for a particular system of particles. It is essentially the flume inclination angle at which the net erosion for a particular system of particles is equal to zero (i.e., $m_{out} - m_s = 0$). The neutral angle is analogous to what Egashira et al. (2001) and Papa et al. (2004) call "the equilibrium angle". Similar to our use of this term, these groups defined this equilibrium, or neutral, angle as the angle at which an erodible bed slope will adjust to when debris flows pass over the erodible bed. The fitted slopes of our linear least squares fits $\frac{\Delta \hat{m}_{e,fit}}{\Delta \phi}$ represents a measure of the sensitivity of the erosion

to the deviation of the angle of inclination from the neutral angle ($\phi - \phi_n$). Since this value is larger for the coarser particles, we suspect the variability of this slope from one system to the next is due to a variability of relative roughness of the particles, another surface property, or a relative asphericity of the particles. Although investigating of this, is beyond the scope of this paper, it is likely important in the context of natural particles that differ more significantly in shape and surface properties and is the topic of future work.

Table 8.3: Fit parameters for uniform particle experiments.

d (mm)	$\phi_n(deg)$	$\Delta\tilde{z}_{e,fit}/\Delta\phi$	R^2
0.8	24.9	0.41	0.996
2.0	26.0	0.46	0.985

We note that for the glass spheres used by Hill et al. (2013); Maki (2018) in their experiments, they found that the neutral angle for the two types of particles and also their 50'/50 mixture was strikingly similar. In contrast, we found that the neutral angles of our zirconium silicate particles differed from one another with statistical significance. Specifically, the neutral angle of the fine particles is smaller (by just over 1^o as shown in Table 8.3) than the coarse particle neutral angle that emphasizes on the role of the bed slope in determining the erosion or deposition patterns of debris flows (Conway et al. (2010)). We hypothesize that this affects the erosion rates of different beds as we discuss in the next section.

8.4.2 Dependence of erosion on composition of initial debris flow

The previous section presented arguments for the differences in total net erosion on coarse particle content in the debris flow from one bed material to the next. Two things are left in question. First: In three out of the four cases discussed here the net total erosion increases with higher concentrations of large particles in the flow (specifically, two from Hill et al. (2013); Maki (2018) and the one over the coarse bed discussed

herein). Second, the instantaneous erosion rates appear to be somewhat less systematically dependent on the large particle fraction in the initial debris flow. Perhaps even more surprisingly, the highest and lowest erosion rates (and deposition rates) do not scale monotonically with concentration of the large particles in the initial debris flow. In this section we consider the first issue. For insight into why the net total erosion increases systematically with increasing large particles in most cases, we consider the potential of collisional energy transfer between chains of large particles compared with small and large particle mixtures. Similar to the concept of "jamming", we hypothesize that increasingly long chains of large particles in contact increases the efficiency of their effect on particles in lower layers. We follow this hypothesis with another in which we hypothesize that increasing fractions of large particles increase the effective impact of the coarse particles with their size, increasing increasing their capability to dislodge other particles.

On the other hand, we did not find a systematic relation between the amount of coarse particles in the supply with net eroded mass when we used a bed composed with fine particles. We hypothesize that a bulk effect drives this, related to the deposition of the coarse particles on the bed inclined lower than its own ϕ_n, as discussed in details in subsection 8.4.1.

For the second question, that of the variation of instantaneous erosion rates with coarse particles in the supply, we turn back to the instantaneous data and images in Section 8.3 to understand.

8.4.3 Effects of instantaneous measures of flow on bed erosion rates

Perhaps the most striking detail of these results is the apparent non-monotonic behavior with changing fine particle concentration in the supply. Despite the results of net eroded mass shown in Fig. 8.2 that shows a decrease in net eroded mass with decreasing amount of coarse particles in the supply when the bed composed of coarse particles, we found different behaviors in a smaller time intervals. Specifically, the net eroded mass is higher

for 75 % fine particle in the supply at early stages of the flow (Fig. 8.13).

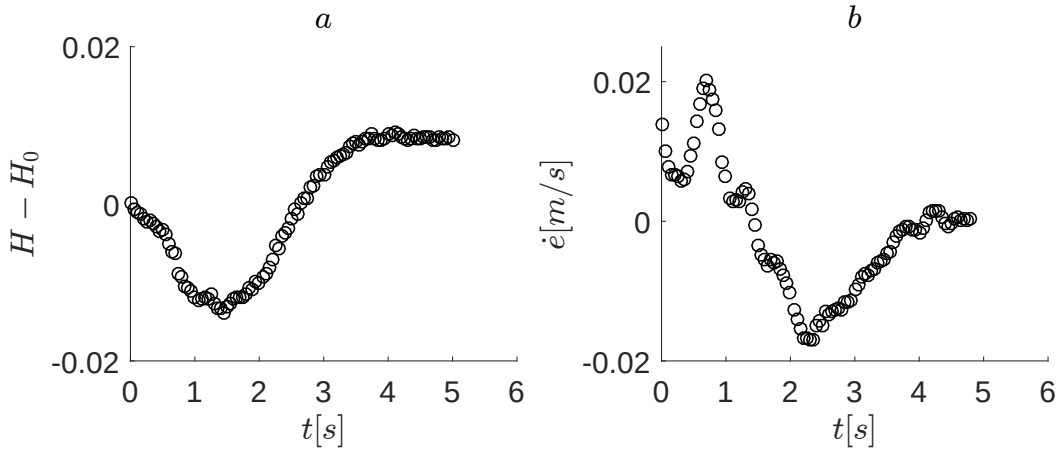

Figure 8.13: Time series of (a) entrainment height, (b) entrainment rate for the experiment with 75 % fine particles in the supply.

The observation of the instantaneous flow conditions at early stages of the flow with 75 % fine particles in the supply (Fig. 8.5) shows the infiltration of these fine particles into the coarse bed once the flow actively shearing the erodible bed. However, our observations did not show the same magnitude of the fine particles infiltration into the bed when we have more (Fig. 8.6) or less (Fig. 8.4) fine particles in the supply. We hypothesize the balance of two parameters control the infiltration of fine into the coarse particles bed: (1) enough fine particles in the supply to infiltrate into the bed before carrying out by the flow (2) coarse particles in the supply to provide enough shear rate at the bed surface to open up spaces to let the fine particles to infiltrate, a process which is known as *kinetic sieving*. The experiment with 75 % fine particles in the supply meets both of these two criteria as it has enough coarse particles in the flow to provide a sufficient shear rate as well as enough fine particles to infiltrate once the shear rate is provided at the bed surface. However, these two criteria are not met at the same time for the other two experiments that we showed in Figs. 8.4 and 8.6 (25 and 100 percent

fine particles in the supply). In particular, for the experiment with 25 % fine particles in the supply, there are enough coarse particles to provide a sufficient shear rate at the bed surface but there are not enough fine particles that can infiltrate into the bed. For the experiment with 100 % fine particles in the supply, there are enough fine particles in the supply; but there are not enough coarse particles to provide a sufficient shear rate at the bed surface.

To explain in more detail the high erosion rate at the beginning of the flow for 75 % fine particles in the supply (Fig. 8.13) is related to the infiltration of fine particles in the coarse bed. Studies of bedlaod transport have shown an increase in transport rate by addition of fine particles in the flow (Hill et al. (2017); Venditti et al. (2010); Yohannes and Hill (2010)). In the context of granular system, this increase in transport can be explained differently. Specifically, for the experiments of this study where the effects of interstitial fluid (air) is negligible, the flow dynamics and entrainment are solely depends on particles interaction. Previous studies along with our observations of recorded videos of the experiments show that a coarse particle on a coarse erodible bed dislodges easier if the flow contain particles of similar size or larger. Once a coarse particle at the bed surface entrains, an open space is created for fine particles to infiltrate. Based on our observations, two reasons can lead to an increase in erosion of particles by the infiltration of fine particles into the bed: (1) segregation in which the coarse particles are tend to move towards the bed surface; (2) filling up the spaces that results in deposition of a coarse particles at a higher elevation. These infiltration may change the bed structure, in particular the force chain between the bed particles. Additionally, complex inter-particle interactions including segregation, and disparate momentum and energy exchange may play a role.

Finally we also note here that not only the 75% mixture has the highest entrainment rate at the beginning but slightly later, the same mixture has the highest deposition rate. We noticed that fine particles keeps infiltrating into the bed as long as the previous two criteria meets: (1) sufficient amount of fine particles to infiltrate; (2) sufficient

magnitude of shear rate at the interface between the flowing layer and erodible bed. When any of these two criteria disappeared, fine particles stop infiltrating. If the amount of fine particles exceeds the capacity of available voids in the bed, fine particles start to make a layer between the top of the flow layer and coarse particles (Fig. 8.7). We noticed once this layer starts to develop, the flow starts to decelerate. We believe the explanation for this flow behavior is due to two factors. First, the layers made of fine particles tends to reach an equilibrium condition that is the their neutral angle. This results in slowing down the coarse particles on top of the flow layer as they now moves on a slope that is smaller than their neutral angle. Once the coarse particles are slowed down, they start to slow down the layers below them. As the contact interface between a coarse particle flowing on top of fine particles is high, the friction forces slow down the motion of fine particle furthermore. Ultimately, this results in a sharp increase in entrainemnt height (Fig. 8.3).

Chapter 9

Summary and Future Work

To summarize: in this dissertation we investigated the characteristics of particles entrainment in two important environmental particle-fluid flows; 1) Bedload transport in rivers, 2) Debris flows in steep upland regions. In a number of ways, the dynamics have similarities in their natural settings. However, the methodology and focus of each in this dissertation are distinct. In this final chapter, we first review the major activities and conclusions. Then we conclude this work by presenting what we see as the next major potential for advancements in these areas.

9.1 Summary of bedload erosion activities and results

Towards studying the bedload transport in rivers, we used Distinct Element Method (DEM) simulations to investigate the behavior of height-dependent entrainment statistics under steady state conditions. We used physics-based interparticle force laws and established drag relationships to represent fluid forces on the particles. Moreover, our particle size distributions followed published experimental work, specifically, the log-normal gravel particle size distribution of experiments performed by Wong et al. (2007); Hill et al. (2017). For a subset of the simulations, we included model turbulent-like velocity fluctuations using a random processes where the turbulent intensities and Reynolds

stress followed physical measurements summarized by Nezu and Nakagawa (1993).

We represented turbulence in a few different ways to study the effects of turbulence fluctuations compared to average turbulence stresses:

1. In two sets of simulations we represented turbulence only through its affect on the form of the average velocity profile and associated average local drag forces on particles. We consider the design of these computational experiments in three contexts:

    - The first set of computational experiments was modeled with a grain size distribution associated with well-established and detailed laboratory flume experiments (Wong et al. (2007))
    - The second set of experiments were designed to investigate the effect of grain size on the statistics of bed height variations in entrainment statistics of bedload transport. The parameters were chosen in based on the results from a single size and scaling considerations.

2. For the rest of the simulations we used the same size distribution as from the Wong et al. (2007) experiments and varied the representation of turbulence. Specifically, we included the magnitude of the stress through the shape of an averaged velocity profile *in addition to* fluctuations in velocities normal to the bed and downstream. We investigated three variation of the form of these fluctuations:

    - Turbulence with uncorrelated normal and downstream fluctuations of evenly distributed magnitudes about their local mean (uniform distribution)
    - Turbulence with uncorrelated normal and downstream fluctuations of normally distributed magnitudes about their local mean (Gaussian distribution)
    - Turbulence with correlated normal and downstream fluctuations of normally distributed magnitudes about their local mean (bi-variate Gaussian distribution)

3. Turbulence with correlated normal and downstream fluctuations where similar to the last case mentioned above, but with the additional consideration of the location of the "zero velocity plane" where the model fluid velocity and velocity fluctuations vanish

In the experiments designed with a grain size distribution and range of bed stresses similar to previously published experiments (Wong et al. (2007)) we found a number of encouraging results that suggested the simulations reasonably represent physical transport processes:

1. The fitted bed "reference" or "excess" shear stress scales with the median grain size as suggested by existing experimental results reported by others (i.e.Meyer-Peter and Muller (1948); Ashida and Michiue (1972); Wong et al. (2007)

2. All the simulations, with or without turbulence fluctuations, reproduced the same power law relations between the bed transport rate and the fitted bed "reference" or "excess" shear stress reported by others (i.e.Meyer-Peter and Muller (1948); Ashida and Michiue (1972); Wong et al. (2007)): $q^* \sim (\tau^* - \tau_c^*)^{3/2}$

3. All the simulations, with or without turbulence fluctuations, reproduced bed height statistics, that is, that are well-represented by a Gaussian distribution.

4. The width of that distribution, represented by the standard deviation about the mean bed height, increases with excess bed shear stress. That is, it increases with bed shear stress with or without the presence of model turbulence fluctuations and scales with both.

Additionally, we presented some unique observations, presently only attainable through simulations such as these, that could give insight to larger scale river reach models. If incorporated, they could be tested by comparing predictions from these models with larger-scale measurements of transport and stratigraphy. Regardless, these provide

physical insight for our understanding of these phenomena and guidance for instrumentalists and modelers alike:

1. All of the simulations exhibited a strong relationship between local bed height and entrainment height statistics. While specific relationships were hypothesized by Wong et al. (2007), as we discuss, they are not capable of producing the details possible in our simulations that are required for closing the probablistic model. Speifically:

    - The entrainment height distribution, similar to the local bed height distribution, follows a normal distribution about the peak entrainment height.
    - The peak entrainment height increases with the standard deviation of the bed height about its average: $\tilde{z}_e \approx 2 \times s_\eta$ above the average bed height for all runs.
    - Unlike the standard deviation of the bed height, s_η, the standard deviation of the entrainment height s_e about its mean height $\tilde{z}_e$ shows no correlation with the Shields stress or turbulence fluctuations.

2. Our (fitted) reference shear stress we found depended on a number of specific model variables:

    - The presence of the turbulent fluctuations. Specifically, the presence of turbulent fluctuations increases the transport rate and results in a drop in the reference shear stress needed to initiate the transport, analogous to that experimentally shown by Lajeunesses and colleagues (Malverti et al. (2008); Lajeunesse et al. (2010)).
    - The location of zero velocity plane where the fluid velocity goes to zero. We note this is well-defined for the case of a log-law near an impermeable bed, various forms have been proposed for a sediment bed. In physical cases, it is

likely dependent on some measure of pore size via the grain size distribution, but we had little physical investigation to support specific relationships.

Finally, the results of these simulations allowed us to provide a link between the longitudinal transport rate and vertical bed surface statistics discussed in the phenomenological model development in Chapter 5.

9.2 Summary of debris erosion activities and results

Towards studying the particle entrainment mechanism in debris flows, we conducted experimental studies to investigate the effect of changing the fraction of large particles in a bimodal grain size distribution in an initial debris flow on the net erosion of the bed over which it flows. To isolate the effects of interstitial fluid, we performed the "dry experiments" or air as an interstitial fluid. In particular, we performed two sets of distinct experiments:

1. A set of *unimodal* experiments on an erodible bed that is composed of either coarse particles (2 mm particles) or fine particles (0.8 mm particles).

2. A set of experiments that we called the *bimodal* experiments in this study that we used bimodal mixtures of particles in the supply but unimodal mixture of particles in the erodible bed.

The set of unimodal experiments were used to determine the neutral angle of the two size particles used in this study. The neutral angle found in these experiments are then used to conduct the experiments at that angle but with a bimodal mixture of particles in the supply. By conducting these experiments and through our observations and analyses, we found:

- The neutral angle for coarse particles are higher than fine particles. This indicates, at the same inclination angle, coarse particles behaves more stable and less erosional compare to the fine particles.

- The flow composition plays an important role in determining the erosion rate behaviors. We found the infiltration of fine particles into the course bed increases the erosion rates. Our observations suggested two conditions that are required for this infiltration to happen: (1) sufficient amount of fine particles in the flow; (2) sufficient amount of shear rate at the bed surface to provide a space for fine particles to infiltrate.

- While the infiltration of fine particles into the course bed can increase the erosion rate in a short run; it can have opposite effects on the long run when the amount of fine particles suppress the available voids in the bed. Once this happens, the additional fine particles make a layer within the flowing layer, above the coarse bed surface and below the coarse particles in the flow that are pushed to the top of the flow due to segregation. Once this layer of fine particles is made between the two layers of coarse particles; it decelerates the flow.

- Despite the role of the bed composition on erosion rates, we found no correlations between the erosion rate with the average shear stress or granular temperature, except at early stages where the granular temperature and erosion rates are slightly correlated.

9.3 Future research directions

These two sets of fundamental research set the foundation for further such investigations into relationships that better predict entrainment in bedload and debris flow systems.

There are a few details that first would be satisfying to settle in these relatively basic frameworks. For the bedload transport systems here are a few details we would suggest future researchers address:

- Our DEM model uses one-way coupling only between the fluid and particles and neglects the influences of particles on fluid velocity. It would be informative to

determine whether this is a reasonable first order approximation or a lowered local or global velocity would be better in modeling real physical systems.

- Our DEM model neglects details of non-sphericity and larger scale roughness in the particles. These may prove to be first order effects that faster computational speed would provide relatively simple means for investigation

- Our DEM model neglects effects of fine clay and silt particles and biofilms that are likely present in real systems and may play a first order role in transport of these systems.

Additionally, we consider how this probablistic entrainment model can inform a physics-based model for bedload transport as discussed in Chapter 5. However, further studies are needed to validate and extend this link into a broader range that could include: 1) a more accurate representation of the flow field in computational experiments, 2) a mixture of particles with different size distribution. The latter case may reveal new insights that can be used to provide a more physics-based formulations of mixture transport rate instead of the hiding factor considerations as are common currently in predicting the mixture transport rate.

In regards to debris flow studies, we suggest the following directions for future studies:

- Prior to conducting any new experiments to capture different aspects of flow dynamics and to provide a better understanding of the erosion rate by debris flows, there is a need to revise the algorithms used in this study for particle locating and tracking. Although our particle locating and tracking algorithm serves well for the purpose of this study, yet there are a few areas that this algorithm needs to be improved:

    1. Our algorithm works well in detecting fine and coarse particles; yet there is some level of noise involved in this particle locating where it erroneously

"detects" fine particles in the areas where there are no fine particles (Fig. 7.8). Possible solutions to this issue may be found by (1) a set up of the experiment where the lightening spread uniformly over area that high speed camera captures, (2) a better image filtering to remove the noise (e.g, due to a few small imperfections on the flume walls) and to better differentiate the fine and coarse particles from one another other, (3) train the machine to detect the particles instead of using the local brightness maxima and the built-in function *imfindcircle*.

2. We suspect that the reason why we found no significant correlations between the granular temperature and erosion rate may be related to our particle tracking algorithm. We used the nearest neighbor algorithm to track the particles. Despite the simplicity of this algorithm, it serves well for our purpose in many cases. However, we found that this algorithm fails to track the particles accurately in some cases. To resolve this issue, we examined a more sophisticated algorithms for particle tracking (such as 3 frames (3MA) and 4 frames (4MA) algorithms Ouellette et al. (2006)). These algorithms assumes the constant velocity or acceleration between the two consecutive frames. For example, 3 frames algorithm uses 3 frames at each time to track the particles; the first two frames are used to estimate the particles velocity and using the estimated velocity, they estimate the particles location in the third frame and finds the closest particle to that estimated location. Our investigations show that these algorithms are not yet capable the of solving the issues with our particle tracking. Therefore, a new and improved algorithm is needed and is currently under investigation.

- New experiments on dry mixtures can be performed to not only have mixtures in the supply but also in the erodible bed.

- New experiments with non-Newtonian interstitial fluid can be performed to provide insights on how more complex rheology of interstitial fluid affects the particles entrainment under the naturally varied loading conditions.

Although this study investigated the particles erosion under controlled and specific conditions (i.e. steady state lower region plane bed for bedload transport and bimodal mixtures with minimum effects of interstitial fluid for debris flows), the findings of this can provide a basic physical understanding of these two particle-fluid systems and extended to the more complex situations. For example, the results of this study for bedload transport can be used to provide a better understanding and prediction of pollutant transport and diffusion in rivers, a better design of hydraulic structures by considering the local scour and ultimately a better understanding of various geomorphological phenomena observed in nature such as vertical and downstream segregation.

References

J. Abbott and J. R. D. Francis. Saltation and suspension trajectories of solid grains in a water stream. *Philosophical Transactions of the Royal Society of London. Series A, Mathematical and Physical Sciences*, 284(1321):225–254, 1977.

C. Ancey. Stochastic modeling in sediment dynamics: Exner equation for planar bed incipient bed load transport conditions. *Journal of Geophysical Research: Earth Surface*, 115(F2), 2010.

A. Armanini. Non-uniform sediment transport: dynamics of the active layer. *Journal of Hydraulic Research*, 33(5):611–622, 1995.

K. Ashida and M. Michiue. Study on hydraulic resistance and bed-load transport rate in alluvial streams [in japanese]. In *Proceedings of the Japan Society of Civil Engineers*, number 206, pages 59–69. Japan Society of Civil Engineers, 1972.

R. A. Bagnold. The flow of cohesionless grains in fluids. *Philosophical Transactions of the Royal Society of London. Series A, Mathematical and Physical Sciences*, 249 (964):235–297, 1956.

G. K. Batchelor. *An introduction to fluid dynamics*. Cambridge, UK: Cambridge university press, 1976.

C. Berger, B. McArdell, and F. Schlunegger. Direct measurement of channel erosion by debris flows, illgraben, switzerland. *Journal of Geophysical Research: Earth Surface*, 116(F1), 2011.

M. Berti, R. Genevois, R. LaHusen, A. Simoni, and P. Tecca. Debris flow monitoring in the acquabona watershed on the dolomites (italian alps). *Physics and Chemistry of the Earth, Part B: Hydrology, Oceans and Atmosphere*, 25(9):707–715, 2000.

A. Blom, J. S. Ribberink, and G. Parker. Vertical sorting and the morphodynamics of bed form-dominated rivers: A sorting evolution model. *Journal of Geophysical Research: Earth Surface*, 113(F1), 2008. doi: 10.1029/2003JF000069.

J. Bridge and D. Dominic. Bed load grain velocities and sediment transport rates. *Water Resources Research*, 20(4):476–490, 1984. doi: 10.1029/WR020i004p00476.

W. R. Brownlie. Flow depth in sand-bed channels. *Journal of Hydraulic Engineering*, 109(7):959–990, 1983.

S. C. Chapra, R. P. Canale, et al. *Numerical methods for engineers*. Boston: McGraw-Hill Higher Education,, 2010.

S. Conway, A. Decaulne, M. Balme, J. Murray, and M. Towner. A new approach to estimating hazard posed by debris flows in the westfjords of iceland. *Geomorphology*, 114(4):556–572, 2010.

Y. Cui, C. Braudrick, W. E. Dietrich, B. Cluer, and G. Parker. Dam removal express assessment models (dream) part 2: Sample runs/sensitivity tests. *Journal of Hydraulic Research*, 44(3):308–323, 2006a. doi: 10.1080/00221686.2006.9521684.

Y. Cui, G. Parker, C. Braudrick, W. E. Dietrich, and B. Cluer. Dam removal express assessment models (dream). part 1: model development and validation. *Journal of Hydraulic Research*, 44(3):291–307, 2006b. doi: 10.1080/00221686.2006.9521683.

P. A. Cundall and O. D. Strack. A discrete numerical model for granular assemblies. *geotechnique*, 29(1):47–65, 1979.

T. G. Drake and J. Calantoni. Discrete particle model for sheet flow sediment transport in the nearshore. *Journal of Geophysical Research: Oceans*, 106(C9):19859–19868, 2001. doi: 10.1029/2000JC000611.

A. Dudill, P. Frey, and M. Church. Infiltration of fine sediment into a coarse mobile bed: a phenomenological study. *Earth Surface Processes and Landforms*, 42(8):1171–1185, 2017.

S. Egashira, N. Honda, and T. Itoh. Experimental study on the entrainment of bed material into debris flow. *Physics and Chemistry of the Earth, Part C: Solar, Terrestrial & Planetary Science*, 26(9):645–650, 2001.

H. A. Einstein et al. *The bed-load function for sediment transportation in open channel flows*, volume 1026. Citeseer, 1950.

M. Farin, A. Mangeney, and O. Roche. Fundamental changes of granular flow dynamics, deposition, and erosion processes at high slope angles: insights from laboratory experiments. *Journal of Geophysical Research: Earth Surface*, 119(3):504–532, 2014.

R. I. Ferguson. Emergence of abrupt gravel to sand transitions along rivers through sorting processes. *Geology*, 31(2):159–162, 2003. doi: 10.1130/0091-7613(2003)031⟨0159:EOAGTS⟩2.0.CO;2.

Y. Forterre and O. Pouliquen. Flows of dense granular media. *Annu. Rev. Fluid Mech.*, 40:1–24, 2008.

P. Frey and M. Church. Bedload: a granular phenomenon. *Earth Surface Processes and Landforms*, 36(1):58–69, 2011.

A. Ghasemi. Study of macroturbulence and bursting via the-1 spectral power law region of turbulent open channel flows over gravel beds. 2016.

A. Ghesemi, J. Fox, and A. Husic. Predicting macroturbulence energy and timescales for flow over a gravel bed: Experimental results and scaling laws. *Geomorphology*, 332:122–137, 2019.

G. Gioia, S. Ott-Monsivais, and K. M. Hill. Fluctuating velocity and momentum transfer in dense granular flows. *Physical review letters*, 96(13):138001, 2006.

J. W. Godt and J. A. Coe. Alpine debris flows triggered by a 28 july 1999 thunderstorm in the central front range, colorado. *Geomorphology*, 84(1-2):80–97, 2007.

A. J. Grass. The influence of boundary layer turbulence on the mechanics of sediment transport. *Proc of Euromech 156, Mechanics of Sediment Transport*, pages 3–17, 1983.

T. d. Haas and T. v. Woerkom. Bed scour by debris flows: experimental investigation of effects of debris-flow composition. *Earth Surface Processes and Landforms*, 41(13): 1951–1966, 2016.

K. Hill, L. Maki, and R. Kaitna. Particle-scale controls on entrainment and deposition due to debris flows. In *AGU Fall Meeting Abstracts*, 2013.

K. M. Hill and D. Tan. Granular flows applied to gravel-bed rivers: particle-scale studies of the mobilization of a gravel bed by the addition of fines. In D. Tsutsumi and J. B. Laronne, editors, *Gravel-Bed Rivers: Processes and Disasters*, chapter 3, pages 73–95. Wiley Online Library, 2017. doi: 10.1002/9781118971437.ch3.

K. M. Hill, G. Gioia, and V. V. Tota. Structure and kinematics in dense free-surface granular flow. *Physical Review Letters*, 91(6):064302, 2003.

K. M. Hill, J. Gaffney, S. Baumgardner, P. Wilcock, and C. Paola. Experimental study of the effect of grain sizes in a bimodal mixture on bed slope, bed texture, and the transition to washload. *Water Resources Research*, 53(1):923–941, 2017.

M. Hirano. River-bed degradation with armoring. In *Proceedings of the Japan Society of Civil Engineers*, volume 1971, pages 55–65. Japan Society of Civil Engineers, 1971.

O. Hungr, S. Evans, and I. Hutchinson. A review of the classification of landslides of the flow type. *Environmental & Engineering Geoscience*, 7(3):221–238, 2001.

R. M. Iverson. The physics of debris flows. *Reviews of geophysics*, 35(3):245–296, 1997.

R. M. Iverson. The debris-flow rheology myth. *Debris-flow hazards mitigation: mechanics, prediction, and assessment*, 1:303–314, 2003.

R. M. Iverson. Elementary theory of bed-sediment entrainment by debris flows and avalanches. *Journal of Geophysical Research: Earth Surface*, 117(F3), 2012.

R. M. Iverson, M. Logan, R. G. LaHusen, and M. Berti. The perfect debris flow? aggregated results from 28 large-scale experiments. *Journal of Geophysical Research: Earth Surface*, 115(F3), 2010.

R. M. Iverson, M. E. Reid, M. Logan, R. G. LaHusen, J. W. Godt, and J. P. Griswold. Positive feedback and momentum growth during debris-flow entrainment of wet bed sediment. *Nature Geoscience*, 4(2):116, 2011.

M. Jakob and P. Friele. Frequency and magnitude of debris flows on cheekye river, british columbia. *Geomorphology*, 114(3):382–395, 2010.

M. Jakob, O. Hungr, and D. M. Jakob. *Debris-flow hazards and related phenomena*, volume 739. Springer, 2005.

C. Ji, A. Munjiza, E. Avital, J. Ma, and J. Williams. Direct numerical simulation of sediment entrainment in turbulent channel flow. *Physics of Fluids*, 25(5):056601, 2013.

Z. Jiang. The motion of sediment-water mixtures during intense bedload transport: computer simulations. *Sedimentology*, 42(6):935–945, 1995.

Z. Jiang and P. Haff. Multiparticle simulation methods applied to the micromechanics of bed load transport. *Water resources research*, 29(2):399–412, 1993. doi: 10.1029/92WR02063.

V. Jomelli, D. Brunstein, M. Déqué, M. Vrac, and D. Grancher. Impacts of future climatic change (2070–2099) on the potential occurrence of debris flows: a case study in the massif des ecrins (french alps). *Climatic Change*, 97(1-2):171–191, 2009.

E. Lajeunesse, L. Malverti, and F. Charru. Bed load transport in turbulent flow at the grain scale: Experiments and modeling. *Journal of Geophysical Research: Earth Surface*, 115(F4), 2010.

L. Landau and E. Lifshitz. Fluid mechanics. 1987. *Course of Theoretical Physics*, 1987.

A. Longjas and K. M. Hill. Evolution of bed fabric from repeated experimental debris flows. 2020.

A. Longjas, J. Mullenbach, and K. M. Hill. Experimental studies of increased bed fragility induced by evolving bed fabric associated with repeated debris flows. In *AGU Fall Meeting Abstracts*, 2016.

R. F. Luque and R. Van Beek. Erosion and transport of bed-load sediment. *Journal of hydraulic research*, 14(2):127–144, 1976.

L. Maki. Laboratory debris flow experiments: A study of erosion. 2018.

L. Malverti, E. Lajeunesse, and F. Métivier. Small is beautiful: Upscaling from microscale laminar to natural turbulent rivers. *Journal of Geophysical Research: Earth Surface*, 113(F4), 2008.

A. Mangeney, L. Tsimring, D. Volfson, I. S. Aranson, and F. Bouchut. Avalanche mobility induced by the presence of an erodible bed and associated entrainment. *Geophysical Research Letters*, 34(22), 2007.

A. Mangeney, O. Roche, O. Hungr, N. Mangold, G. Faccanoni, and A. Lucas. Erosion and mobility in granular collapse over sloping beds. *Journal of Geophysical Research: Earth Surface*, 115(F3), 2010.

R. Maurin, J. Chauchat, B. Chareyre, and P. Frey. A minimal coupled fluid-discrete element model for bedload transport. *Physics of Fluids*, 27(11):113302, 2015.

S. McCoy, J. W. Kean, J. A. Coe, G. Tucker, D. M. Staley, and T. Wasklewicz. Sediment entrainment by debris flows: In situ measurements from the headwaters of a steep catchment. *Journal of Geophysical Research: Earth Surface*, 117(F3), 2012.

I. McEwan, B. Jefcoate, and B. Willetts. The grain-fluid interaction as a self-stabilizing mechanism in fluvial bed load transport. *Sedimentology*, 46(3):407–416, 1999.

S. McLean, J. Nelson, and S. Wolfe. Turbulence structure over two-dimensional bed forms: Implications for sediment transport. *Journal of Geophysical Research: Oceans*, 99(C6):12729–12747, 1994.

E. Meyer-Peter and R. Muller. Formulas for bed-load transport. In *Proceedings of the 2nd meeting of the International Association for Hydraulic Structures Research*, pages 39–64. Stockholm, Sweden: International Association for Hydraulic Structures Research., 1948.

D. Moberly. Laboratory experiments investigating entrainment by debris flows. 2015.

J. Mullenbach. Experimental studies of the influence of the properties of the matrix of a debris flow on its erosional behavior. 2018.

H. Nakagawa, I. Nezu, and H. Ueda. Turbulence of open channel flow over smooth and rough beds. In *Proceedings of the Japan Society of Civil Engineers*, volume 1975, pages 155–168. Japan Society of Civil Engineers, 1975.

J. M. Nelson, R. L. Shreve, S. R. McLean, and T. G. Drake. Role of near-bed turbulence structure in bed load transport and bed form mechanics. *Water resources research*, 31(8):2071–2086, 1995.

I. Nezu and H. Nakagawa. Turbulence in open channels. *IAHR/AIRH Monograph. Balkema, Rotterdam, The Netherlands*, 1993.

V. Nikora. Flow turbulence over mobile gravel-bed: spectral scaling and coherent structures. *Acta Geophysica Polonica*, 53(4):539, 2005.

N. T. Ouellette, H. Xu, and E. Bodenschatz. A quantitative study of three-dimensional lagrangian particle tracking algorithms. *Experiments in Fluids*, 40(2):301–313, 2006.

M. Papa, S. Egashira, and T. Itoh. Critical conditions of bed sediment entrainment due to debris flow. *Natural Hazards and Earth System Sciences*, 4(3):469–474, 2004.

G. Parker. Selective sorting and abrasion of river gravel. i: Theory. *Journal of Hydraulic Engineering*, 117(2):131–147, 1991a. doi: 10.1061/(ASCE)0733-9429(1991)117:2(131).

G. Parker. Selective sorting and abrasion of river gravel. ii: Applications. *Journal of Hydraulic Engineering*, 117(2):150–171, 1991b. doi: 10.1061/(ASCE)0733-9429(1991)117:2(150).

G. Parker. 1d sediment transport morphodynamics with applications to rivers and turbidity currents. *E-book available from http://vtchl. uiuc. edu/people/parkerg/morphodynamics_e-book. htm (last accessed 23 February 2010)*, 2004.

G. Parker, C. Paola, and S. Leclair. Probabilistic exner sediment continuity equation for mixtures with no active layer. *Journal of Hydraulic Engineering*, 126(11):818–826, 2000. doi: 10.1061/(ASCE)0733-9429(2000)126:11(818).

A. Pelosi, G. Parker, R. Schumer, and H.-B. Ma. Exner-based master equation for transport and dispersion of river pebble tracers: Derivation, asymptotic forms, and quantification of nonlocal vertical dispersion. *Journal of Geophysical Research: Earth Surface*, 119(9):1818–1832, 2014. doi: 10.1002/2014JF003130.

A. Perry, S. Henbest, and M. Chong. A theoretical and experimental study of wall turbulence. *Journal of Fluid Mechanics*, 165:163–199, 1986.

A. Perry, K. Lim, and S. Henbest. An experimental study of the turbulence structure in smooth-and rough-wall boundary layers. *Journal of Fluid Mechanics*, 177:437–466, 1987.

S. B. Pope. Turbulent flows, 2001.

M. E. Reid, R. M. Iverson, M. Logan, R. G. LaHusen, J. W. Godt, and J. P. Griswold. Entrainment of bed sediment by debris flows: results from large-scale experiments. In *Fifth International Conference on Debris-flow Hazards Mitigation, Mechanics, Prediction and Assessment, edited by: R. Genevois, Hamilton, DL, and Prestinizi, A., Casa Editrice Universita La Sapienza, Rome*, pages 367–374. Citeseer, 2011.

P. Revellino, O. Hungr, F. M. Guadagno, and S. G. Evans. Velocity and runout simulation of destructive debris flows and debris avalanches in pyroclastic deposits, campania region, italy. *Environmental Geology*, 45(3):295–311, 2004.

J. S. Ribberink. Mathematical modelling of one-dimensional morphological changes in rivers with non-uniform sediment. 1987.

J. C. Roseberry, M. W. Schmeeckle, and D. J. Furbish. A probabilistic description of the bed load sediment flux: 2. particle activity and motions. *Journal of Geophysical Research: Earth Surface*, 117(F3), 2012.

S. Savage and C. Lun. Particle size segregation in inclined chute flow of dry cohesionless granular solids. *Journal of Fluid Mechanics*, 189:311–335, 1988.

H. Schlichting and K. Gersten. *Boundary-layer theory*. Springer, 2016.

M. W. Schmeeckle. Numerical simulation of turbulence and sediment transport of medium sand. *Journal of Geophysical Research: Earth Surface*, 119(6):1240–1262, 2014.

M. W. Schmeeckle and J. M. Nelson. Direct numerical simulation of bedload transport using a local, dynamic boundary condition. *Sedimentology*, 50(2):279–301, 2003. doi: 10.1046/j.1365-3091.2003.00555.x.

J. D. Stock and W. E. Dietrich. Erosion of steepland valleys by debris flows. *Geological Society of America Bulletin*, 118(9-10):1125–1148, 2006.

M. Stoffel and M. Beniston. On the incidence of debris flows from the early little ice age to a future greenhouse climate: a case study from the swiss alps. *Geophysical Research Letters*, 33(16), 2006.

B. M. Sumer, L. H. Chua, N.-S. Cheng, and J. Fredsøe. Influence of turbulence on bed load sediment transport. *Journal of Hydraulic Engineering*, 129(8):585–596, 2003.

T. Takahashi. A review of japanese debris flow research. *International Journal of Erosion Control Engineering*, 2(1):1–14, 2009.

Y. Tsuji, T. Tanaka, and T. Ishida. Lagrangian numerical simulation of plug flow of cohesionless particles in a horizontal pipe. *Powder technology*, 71(3):239–250, 1992. doi: 10.1016/0032-5910(92)88030-L.

L. C. Van Rijn. Equivalent roughness of alluvial bed. *Journal of the Hydraulics Division*, 108(10):1215–1218, 1982.

J. Venditti, W. Dietrich, P. Nelson, M. Wydzga, J. Fadde, and L. Sklar. Mobilization of coarse surface layers in gravel-bedded rivers by finer gravel bed load. *Water Resources Research*, 46(7), 2010.

E. Viparelli, R. Haydel, M. Salvaro, P. R. Wilcock, and G. Parker. River morphodynamics with creation/consumption of grain size stratigraphy 1: laboratory experiments. *Journal of Hydraulic Research*, 48(6):715–726, 2010a. doi: 10.1080/00221686.2010.515383.

E. Viparelli, O. E. Sequeiros, A. Cantelli, P. R. Wilcock, and G. Parker. River morphodynamics with creation/consumption of grain size stratigraphy 2: numerical model. *Journal of Hydraulic Research*, 48(6):727–741, 2010b. doi: 10.1080/00221686.2010.526759.

E. Viparelli, L. Solari, and K. Hill. Downstream lightening and upward heavying: Experiments with sediments differing in density. *Sedimentology*, 62(5):1384–1407, 2015.

G. Wieczorek, B. Morgan, and R. Campbell. Debris-flow hazards in the blue ridge of central virginia. *Environmental & Engineering Geoscience*, 6(1):3–23, 2000.

P. R. Wilcock and J. C. Crowe. Surface-based transport model for mixed-size sediment. *Journal of Hydraulic Engineering*, 129(2):120–128, 2003.

M. Wong and G. Parker. Reanalysis and correction of bed-load relation of meyer-peter and müller using their own database. *Journal of Hydraulic Engineering*, 132(11):1159–1168, 2006.

M. Wong, G. Parker, P. DeVries, T. M. Brown, and S. J. Burges. Experiments on dispersion of tracer stones under lower-regime plane-bed equilibrium bed load transport. *Water Resources Research*, 43, 2007. doi: 10.1029/2006WR005172.

A. Yeganeh, H. Gotoh, and T. Sakai. Applicability of euler-lagrange coupling multiphase-flow model to bed-load transport under high bottom shear. *Journal of Hydraulic Research*, 38(5):389–398, 2000.

A. Yeganeh-Bakhtiary, B. Shabani, H. Gotoh, and S. S. Wang. A three-dimensional distinct element model for bed-load transport. *Journal of Hydraulic Research*, 47(2): 203–212, 2009.

B. Yohannes and K. M. Hill. Rheology of dense granular mixtures: Particle-size distributions, boundary conditions, and collisional time scales. *Physical Review E*, 82(6): 061301, 2010.

T. Zhao. *Investigation of Landslide-induced Debris Flows by the DEM and CFD.* PhD thesis, University of Oxford, 2014.

H. Zhu, Z. Zhou, R. Yang, and A. Yu. Discrete particle simulation of particulate systems: a review of major applications and findings. *Chemical Engineering Science*, 63(23): 5728–5770, 2008.